NONLINEAR DISTORTION MITIGATION IN DYNAMIC-RANGE-LIMITED OPTICAL WIRELESS COMMUNICATION SYSTEMS

A Dissertation
Presented to
The Academic Faculty

by

Kai Ying

In Partial Fulfillment
of the Requirements for the Degree
Doctor of Philosophy in the
School of Electrical and Computer Engineering

Georgia Institute of Technology
December 2016

Copyright © 2016 by Kai Ying

NONLINEAR DISTORTION MITIGATION IN DYNAMIC-RANGE-LIMITED OPTICAL WIRELESS COMMUNICATION SYSTEMS

Approved by:

Dr. G. Tong Zhou, Advisor
School of Electrical and Computer Engineering
Georgia Institute of Technology

Dr. Robert J. Baxley, Co-advisor
School of Electrical and Computer Engineering
Georgia Institute of Technology

Dr. Gee-Kung Chang
School of Electrical and Computer Engineering
Georgia Institute of Technology

Dr. Xiaoli Ma
School of Electrical and Computer Engineering
Georgia Institute of Technology

Dr. John R. Barry
School of Electrical and Computer Engineering
Georgia Institute of Technology

Dr. Yao Xie
School of Industrial and Systems Engineering
Georgia Institute of Technology

Date Approved: October 4, 2016

To my family

ACKNOWLEDGEMENTS

First, I would like to express my sincere gratitude to my Ph.D. advisors Dr. G. Tong Zhou and Dr. Robert J. Baxley for providing me an opportunity to work in their labs and continuously supporting my study and related research.

I would also like to thank the other members of my Ph.D. dissertation committee: Dr. Gee-Kung Chang, Dr. Xiaoli Ma, Dr. John R. Barry and Dr. Yao Xie, for their time to attend my thesis defense and their insightful suggestions on my dissertation, which are of great help.

Besides, I would like to give my special thanks to Wallace H. Coulter Foundation and the CEO Ms. Sue Van that have sponsored my study in both Ph.D. program and Georgia Tech Shanghai Master program.

My sincere thank also goes to the members in the research group: Dr. Zhenhua Yu, Dr. Qi Zhou, Dr. Marie Shinotsuka, Dr. Andrew Harper, Dr. Malik Muhammad Usman Gul, Brian Beck, Yiming Kong, Qingsong Wen, Hyunwoo Cho, Dr. Junwen Zhang, Dr. Ming Zhu, Jing Wang, Mu Xu, Lin Cheng, Feng Lu and other colleagues, for the support and help during these years.

Additionally, I would like to thank all my friends from Georgia Tech Shanghai program for encouraging and accompanying me.

Last but not the least, I would like to thank my parents and my wife. Without their support, care and love, I could not have had such a happy and fruitful life in general.

TABLE OF CONTENTS

LIST OF TABLES

LIST OF FIGURES

SUMMARY

The objective of this dissertation is to mitigate the nonlinear distortion in dynamic-range-limited optical wireless communication (OWC) systems. Similar to radio frequency (RF) systems, nonlinear components in OWC systems distort the signal and degrade system performance. The light emitting diode (LED) is the major source of nonlinearities since the electrical-to-optical conversion in the LED is nonlinear. Moreover, to drive the LED, the input electric signal must be positive and exceed the turn-on voltage of the device. On the other hand, the signal is also limited by the saturation point or maximum permissible value of the LED. As a result, the nonlinearity in an OWC system belongs to a family of dynamic-range-limited nonlinearities.

To overcome nonlinearities, we can deal with either the signal or the system. One straightforward approach is to choose or modify input signals such that they are insensitive to the nonlinear distortions, which is named as waveform-specific mitigation. For example, we can use on-off keying (OOK) or pulse position modulation (PPM), which produces two-level signals and is immune to system nonlinearities. For orthogonal frequency division multiplexing (OFDM) signals, peak-to-average power ratio (PAPR) reduction techniques can be utilized. With smaller dynamic-range, the signal after PAPR reduction is less vulnerable to nonlinearities than the original input signal. Another approach is to compensate for the nonlinearities by predistortion or postdistortion, which is named as waveform-agnostic mitigation. After compensation, the overall system response is approximately linear.

In the preliminary research, we will analyze how to maximize the signal-to-noise-plus-distortion ratio (SNDR) of the nonlinearities in OWC systems. Specifically,

we answer the question of how to optimally predistort a double-sided memory-less nonlinearity that has both a "turn-on" value and a maximum "saturation" value. The result herein can serve as a guideline to design predistortion linearization of nonlinear devices like LEDs. Additionally, we will study the constrained clipping method which can mitigate the distortions so that the clipping levels can be more aggressive than the simple clipping to further reduce the PAPRs. Unlike RF signaling, both the maximum and minimum of OWC signals must be considered since OWC systems are dynamic-range-limited. In this case, we care about PAPRs on both the upper side and the lower side, which are named as upper PAPR (UPAPR) and lower PAPR (LPAPR).

In the follow-up research, we will extend our work to multiple-input multiple-output (MIMO) OWC systems and bit-loaded OFDM systems respectively. In the MIMO OWC system, we will study the design of MIMO transceiver under the OWC-specific constraints such as the dynamic-range constraint. The design goal is to avoid double-sided clipping distortions and to fully utilize the spatial multiplexing. In the bit-loaded OFDM system, we will consider constellation-wise distortion constraints into the design of PAPR reduction techniques. We would like to enhance the PAPR performances on both sides and guarantee that the distortion requirements of all the in-band subcarriers can be satisfied.

CHAPTER I

INTRODUCTION

1.1 Motivation of optical wireless communications

In recently years, optical wireless communications (OWC) have attracted many attentions in both academia and industry. The reasons are summarized as following [1–4]:

- Light emitting diodes (LEDs) dominate the world of illumination.

  Recently, many traditional companies have killed incandescent bulb production and focused on creating LED lights. The benefits of the LED are attractive. First of all, it has a very high energy efficiency, which is at least ten times greater than incandescent bulbs. Additionally, the lifetime of the LED is also much longer. There is no doubt that LEDs will be widely deployed in the near future.

- OWC can be a complementary solution to meet the ever growing demand in wireless data.

  With a growing number of communication devices, we have more and more data traffics. Since LEDs will be applied almost everywhere, the human beings can "borrow" their lights for communications. The light spectrum is license-free worldwide, so that OWC can help solve the spectrum scarcity problem at radio frequency (RF) systems. Moreover, we can reuse the modulation bandwidth spatially in adjacent communication cells (rooms).

- Recent advancements in LED technology enable fast switching time.

  The remaining issue is the feasibility of data transmissions by LED lighting. Actually, LEDs can switch very fast so that human eyes cannot recognize the

fast-changing of the light. Thus, it is possible for LEDs to support illumination and communication simultaneously.

- The light transmission is immune to radio frequency interference.

  In this case, OWC can coexist with cellular networks and WiFi hot spots.

- OWC employs relatively low-cost front ends.

  Comparing to complex RF antenna systems, the commercial LEDs are much cheaper.

- The light is safe to human bodies and electro-sensitive devices.

  OWC can be applied in some sensitive scenarios such as hospitals and airplanes.

- OWC has a high level of security.

  The data can only be received within the illumination areas. The information leakage is not a big issue in OWC.

1.2 OWC system model

The basic model of OWC is shown in Fig. 1. OWC employs intensity modulation and direct detection (IM/DD) [1, 3, 5]. At the transmitter side, LED converts the amplitude of the electric signal into the intensity of the optical signal. At the receiver side, the photo detector (PD) generates the electric signal proportional to the intensity of the received optical signal. The light can be visible light or infrared light [5]. If we use visible light, it is called visible light communications (VLC). This dissertation concentrates on VLC, but the fundamental results can be applied to other optical wireless applications and even intensity-modulated laser transmissions.

Comparing to amplitude-limited systems like RF systems, there are three major differences in OWC [1–5].

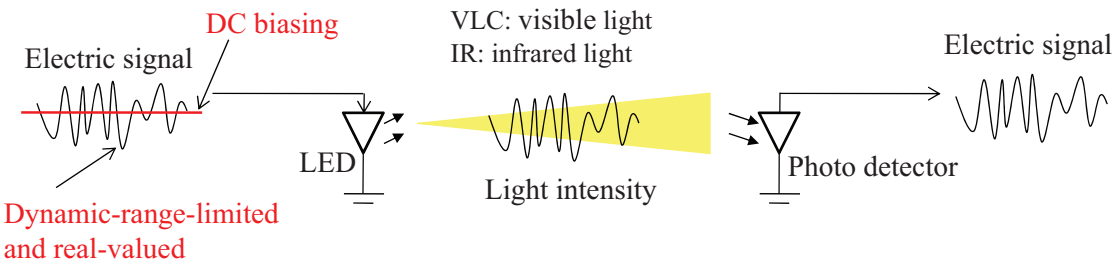

Figure 1: System model for OWC.

- Real-valued: Since OWC uses intensity modulation, the electric signals should be real-valued.

- Dynamic-range-limited: To drive the LED, there is a turn-on voltage. In addition, LED has a saturation point or a maximum permissible value.

- Direct current (DC) biasing required: In most cases, the electric signal is bipolar. It can be positive or negative. A DC biasing is always required to move the signal to the working range of LED.

1.3 Nonlinear distortions in OWC

OWC systems may contain many nonlinear components including driving circuits, digital-to-analog converters (DACs), analog-to-digital converters (ADCs), LEDs and PDs. Among all these nonlinear components, the LED is the major source of nonlinearities [4, 6–9]. According to the OWC-specific characteristics mentioned in the last section, we care about two kinds of nonlinear distortions.

- Signal beyond dynamic-range: double-sided clipping.

  To drive the LED, the input electric signal must be greater than the turn-on value and less than the maximum permissible value or the saturation point of the LED. When the signal is beyond the required dynamic-range, clipping on both sides is applied. Clipping results in distortions and degrades the system

performance. Thus, one of the major objective in this dissertation is to avoid or reduce the double-sided clipping distortions.

- Signal within dynamic-range: nonlinear transfer function.

  For the signal within the dynamic-range, the input-output relationship may not be linear. Hence, other objectives of this dissertation include how to model such nonlinearities and how to construct an optimal input-output transfer function.

1.4 OWC waveforms

1.4.1 Single carrier waveform

Using single carrier is a direct and simple way modulate the OWC signals. There are two major modulation schemes [2]:

- Pulse amplitude modulation (PAM).

  M-ary pulse amplitude modulation (M-PAM) converts the information bits into M different amplitude levels of the signal. The number of bits per symbol duration is $\log_2 M$. 2-PAM is equivalent to on-off keying (OOK).

- Pulse position modulation (PPM).

  Each symbol duration is divided into multiple time slots, then the information is presented by the pulse position. Considering 2-PPM as an example, 0 is represented by a positive pulse at the beginning of the period followed by a lower level pulse, and 1 is represented by a lower level pulse at the beginning of the period followed by a positive pulse.

Fig. 2 shows examples of OOK and 2-PPM. Single carrier waveforms above are real-valued and relatively insensitive to nonlinearities. They can be easily implemented, but the spectrum utilization efficiency is limited.

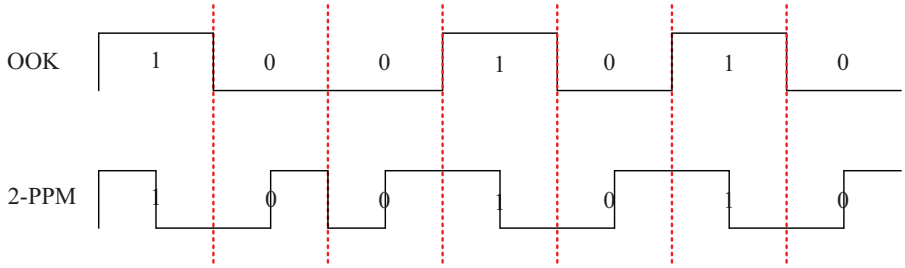

Figure 2: Examples for single carrier waveforms.

1.4.2 Multi-carrier waveform

Recently, orthogonal frequency division multiplexing (OFDM) has been proposed in OWC systems to boost the date rate [19–23]. In addition, bit-loading further enables OFDM to make full use of the LED modulation bandwidth [56]. To satisfy real-value requirement, Hermitian symmetry is applied to the subcarriers [19–23, 56]. The disadvantage of OFDM is the high peak-to-average power ratio (PAPR) [19–23, 56], which makes the signal sensitive to the dynamic-range-limited nonlinearities. Moreover, in dynamic-range-limited OWC systems, PAPRs on both upper side and lower side should be taken into account [22, 23]. Thus, double-sided PAPR reduction is one of the major topics in this dissertation.

1.5 OWC channels

1.5.1 Single-input single-output (SISO)

In the indoor OWC system, there are two types of links, which is shown in Fig. 3. One is the direct point-to-point line-of-sight (LOS) link and the other is the diffuse link caused by reflections. In most cases, only the LOS link is considered since it is usually much stronger than the diffuse link [44–51, 59]. Authors in [49] showed that even the strongest multipath component was at least 7 dB lower than the weakest LOS component. In [51], it was pointed out that no multipath interference would occur at data rates below several hundreds Mb/s according to a root mean square delay spread investigation. Practically, the emission from an LED can be modeled by

a generalized Lambertian radiant intensity [60]:

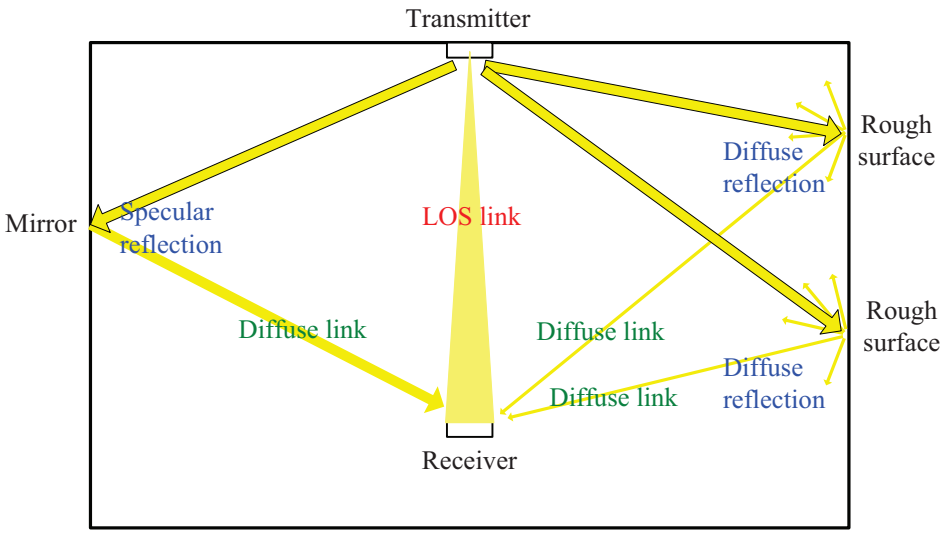

Figure 3: Illustration of LOS links and diffuse links in OWC systems.

$$R_o(\phi) = \frac{m+1}{2\pi} \cos^m \phi \tag{1}$$

where ϕ is the angle of emission relative to the optical axis of the emitter; m is the order of Lambertian emission given by $m = -\ln 2 / \ln(\cos \Phi_{\frac{1}{2}})$ and $\Phi_{\frac{1}{2}}$ is the transmitter semiangle (at half power).

At the receiver, the photo detector (PD), the frequency response of LOS channel is relatively flat near DC, which can be modeled as

$$h = \begin{cases} \frac{A}{d^2} R_o(\phi) \cos\theta, & \text{for } \theta \leq \Theta_{\frac{1}{2}}, \\ 0, & \text{for } \theta > \Theta_{\frac{1}{2}} \end{cases} \tag{2}$$

where θ is the angle of incidence with respect to the receiver axis; $\Theta_{\frac{1}{2}}$ is the field-of-view (FOV) semiangle of receiver; A is the detector area of receiver; and d is the distance between the transmitter and the receiver [5].

1.5.2 Multiple-input multiple-output (MIMO)

Current low-cost commercial LED has narrow modulation bandwidth, which limits the throughput of OWC. Optical MIMO has been proposed in OWC systems to boost the data rate by utilizing spatial multiplexing to obtain parallel data streams [44–53].

Considering the channel for a MIMO OWC system, where signals are transmitted by multiple LEDs and received by multiple PDs, the MIMO channel matrix H can be determined by the direct current (DC) gains among each LED and PD pair [49]:

$$\mathbf{H} = \begin{bmatrix} h_{11} & h_{12} & \cdots & h_{1N_t} \\ h_{21} & h_{22} & \cdots & h_{2N_t} \\ \vdots & \vdots & \ddots & \vdots \\ h_{N_r1} & h_{N_r2} & \cdots & h_{N_rN_t} \end{bmatrix}, \tag{3}$$

where N_t is the number of LEDs and N_r is the number of PDs; and element h_{mn} can be derived from (2) corresponding to the nth LED and the mth PD.

1.6 Organization of this dissertation

The rest of the dissertation is organized as following:

Chapter 2 shows the modeling and analysis of nonlinearities in OWC systems. Additionally, we summarize distortion mitigation techniques, which can help address nonlinear issues in OWC systems.

In Chapter 3, we theoretically prove how to construct an optimal input-output transfer function to minimize the nonlinear effects in dynamic-range-limited systems like OWC systems. The fundamental result can be a guideline for predistortion along with system design in OWC or other dynamic-range-limited applications.

Chapter 4 studies the topic of double-sided PAPR reduction. Some VLC-specific requirements, such as dimming control, are taken into account. A distortion-based method evolving from simple clipping, which is named constrained clipping, is adopted

to mitigate the clipping distortions. Thus, lower clipping levels can be applied to further reduce the PAPRs on both upper side and lower side.

In Chapter 5, we extend our work to optical MIMO. Different from SISO scenarios, we aim to design MIMO precoders and detection techniques to avoid double-sided clipping distortions and to fully utilize the spatial multiplexing. Several optical MIMO transceiver schemes are analyzed and compared. The proposed minimum mean-square error (MMSE) precoder and equalizer can be a practical and efficient solution for indoor VLC-MIMO systems.

In Chapter 6, we enhance the constrained clipping so that it can be applied to bit-loaded VLC-OFDM systems more efficiently. The proposed constellation-wise mitigation helps revise and "relocate" the clipping distortions among all the in-band subcarriers reasonably according to their different selections of modulation schemes. Hence, all the subcarriers can satisfy the error vector magnitude (EVM) requirements and the clipping levels are no longer restricted by the subcarriers with the highest modulation order, so that double-sided PAPR performance can be improved.

In the final analysis, Chapter 7 summarizes the contributions of the dissertation and then suggests topics for future study.

CHAPTER II

NONLINEARITIES AND DISTORTION MITIGATION TECHNIQUES IN OWC

Many physical devices used in optical wireless communication (OWC) or visible light communication (VLC) systems exhibit nonlinear effects, which can significantly degrade the overall system performance. For example, the light emitting diode (LED) is the major source of the nonlinearity. The forward current is zero unless the forward voltage exceeds a "turn-on" value. The forward current is also limited with a maximum permissible value. In addition, the electrical-to-optical conversion is also nonlinear. In this chapter, we provide an overview of techniques related to modeling and distortion mitigation techniques of the nonlinearity in OWC/VLC systems. Appropriate models and robust nonlinearity mitigation techniques are crucial to support high-speed transmissions in practical OWC/VLC systems. Although this dissertation mainly studies on VLC systems, the distortion analysis and mitigation techniques can also be applied to other optical wireless applications and even intensity-modulated laser transmissions.

2.1 Introduction

In recent years, with the improvement of the light emitting diode (LED) chip design and massive deployment of the LED devices, visible light communication (VLC) systems have become an attractive method. VLC can help address the current challenges in wireless communications such as the bandwidth limitation, energy efficiency, electromagnetic radiation and safety [1]. VLC is on the road to standardization and commercialization [2, 3].

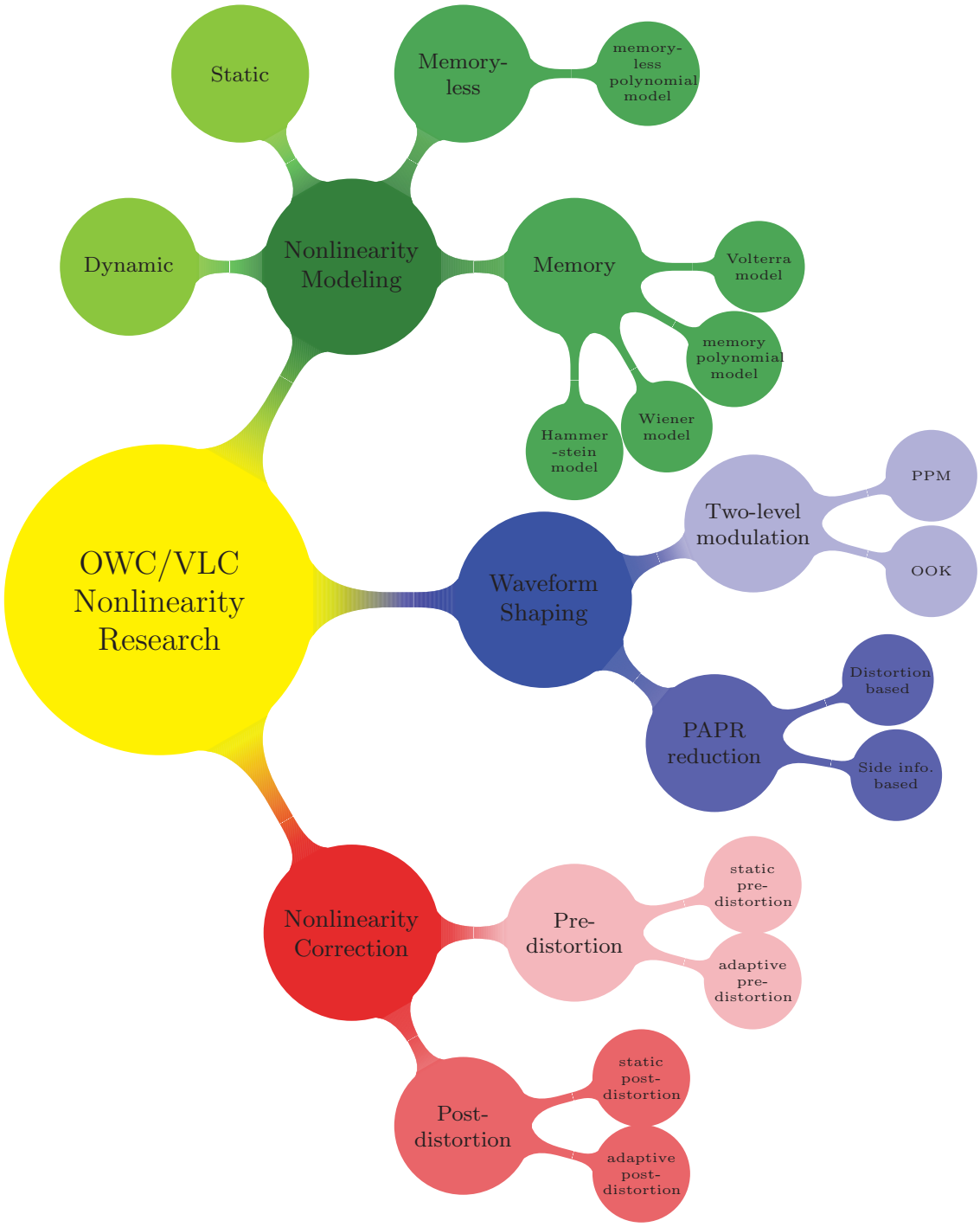

Figure 4: Study topics of nonlinear distortion mitigation in OWC/VLC.

Similar to radio frequency (RF) systems, nonlinear components in VLC systems distort the signal and degrade system performance. Nonlinear distortions in VLC systems may come from driving circuits of the LEDs, digital-to-analog converters (DACs), analog-to-digital converters (ADCs), LEDs and PDs. Since the optical front-end tends to employ simple intensity modulation and direct detection (IM/DD) techniques, the system performance is also sensitive to nonlinearities in the electrical-to-optical conversion and optical-to-electrical conversion. Among all nonlinear sources, the LED is the major source of nonlinearities. Both the voltage-current relationship and the current-light intensity relationship in the LED are nonlinear [4, 6–9]. At the receiver, the PD operates in a narrow range so that the distortion is not as significant as that in the LED [9]. Moreover, to drive the LED, the input electric signal must be positive and exceed the turn-on voltage of the device. On the other hand, the signal is also limited by the saturation point or maximum permissible value of the LED. As a result, the nonlinearity in a VLC system belongs to a family of dynamic-range-limited nonlinearities.

The overall VLC system can be modeled as follows. Denoted by $x(n)$ a real-valued input signal, the received signal $y(n)$ is modeled by

$$y(n) = h(x(n)) + v(n), \tag{4}$$

where $v(n)$ is additive noise; $h(\cdot)$ is a nonlinear mapping or transfer function with dynamic-range constraint $A_{min} \leq h(x(n)) \leq A_{max}$. The dynamic-range is determined by the characteristics of the LED.

For the signal beyond the dynamic-range of the device, double-sided clipping can be used to model such nonlinear effects. For the signal within the dynamic-range, a nonlinear transfer function may be applied to model the nonlinear effects. Both distortions impact the overall system performance.

Nonlinearity modeling is essential for the discussion of the impact of nonlinearities and mitigation methods. The nonlinear models can be divided into memory models

and memory-less models, based on whether we take into account the memory effects of nonlinearities. On the other hand, according to whether the dynamic characteristics of LEDs are considered or not, we can also categorize the nonlinear models into dynamic models and static models. Current researches mainly concentrate on static, memory-less LED nonlinearity modeling [4, 6–9, 14]. In these cases, present output only depends on present input. The nonlinearity does not change over time, either. To model such nonlinearities, one approach is to fit the nonlinear transfer function using measurement data with power series (e.g. Taylor expansion). However, the memory-less polynomial model is inadequate to describe the LED nonlinearity, especially for high speed transmission. Actually, the current-voltage response of the LED is frequency-dependent, thus introduces nonlinearities with memory effects [4, 15]. In these cases, the output of the LED depends not only on the present input, but also on past input values. In addition, the LED characteristics may change over time due to the component aging and temperature changes [4]. The dynamic nonlinearities can degrade the accuracy of the nonlinearity mitigation techniques. Careful and adequate modeling of nonlinearities in VLC is required to design the mitigation methods.

With appropriate models, we can work on mitigating the impact of nonlinear distortions. One straightforward approach is to choose or modify input signals such that they are insensitive to the nonlinear distortions. For example, we can use on-off keying (OOK) or pulse position modulation (PPM), which produces two-level signals and is immune to system nonlinearities. For orthogonal frequency division multiplexing (OFDM) signals, peak-to-average power ratio (PAPR) reduction techniques can be utilized. With smaller dynamic-range, the signal after PAPR reduction is less vulnerable to nonlinearities than the original input signal. Another approach is to compensate for the nonlinearities by predistortion or postdistortion. After compensation, the overall system response is approximately linear. Predistortion or postdistortion has been widely used in different areas [61, 62]. In this chapter, we will

show the particular characteristics in VLC. To take into account memory effects and time-varying characteristics, robust mitigation techniques are necessary to adapt to the system dynamics.

We summarize current and potential topics related to LED nonlinearities for VLC in Fig. 4. The remainder of this chapter is organized as follows. We first present the modeling of LED nonlinearities and discuss the impact of nonlinear distortions. We also point out that the LED exhibits time-varying characteristics, which should be taken into account for robust nonlinear distortion mitigation design. Afterwards, both waveform-specific mitigation techniques and waveform-agnostic mitigation techniques are discussed. For the former, some specific modulation schemes are studied and PA-PR reduction techniques for OFDM signal are presented. For the latter, we show the optimal nonlinear mapping for dynamic-range-limited nonlinearities and then show the linearization approaches such as the predistortion and postdistortion. Finally, we point out challenges of nonlinear distortion mitigation in VLC and conclude the chapter.

2.1.1 Nonlinearities in LED

LED is the major source of nonlinearities in VLC. Fig. 5 shows the nonlinear characteristics of the LED's voltage-current (V-I) conversion and current-optical power (I-O) conversion. In [8, 16], details on nonlinearities of V-I relationship were presented. The authors in [6, 7, 15] concentrated on I-O nonlinear curve. In this chapter, we consider modeling both of them with one nonlinear transfer function. Since VLC employs light intensity modulation and the voltage of electric signal always serves as the control variable, the overall system function can be described by the V-O curve.

2.1.2 Memory-less vs. memory

Models for LED nonlinearities can be divided into two categories: memory-less models and memory models.

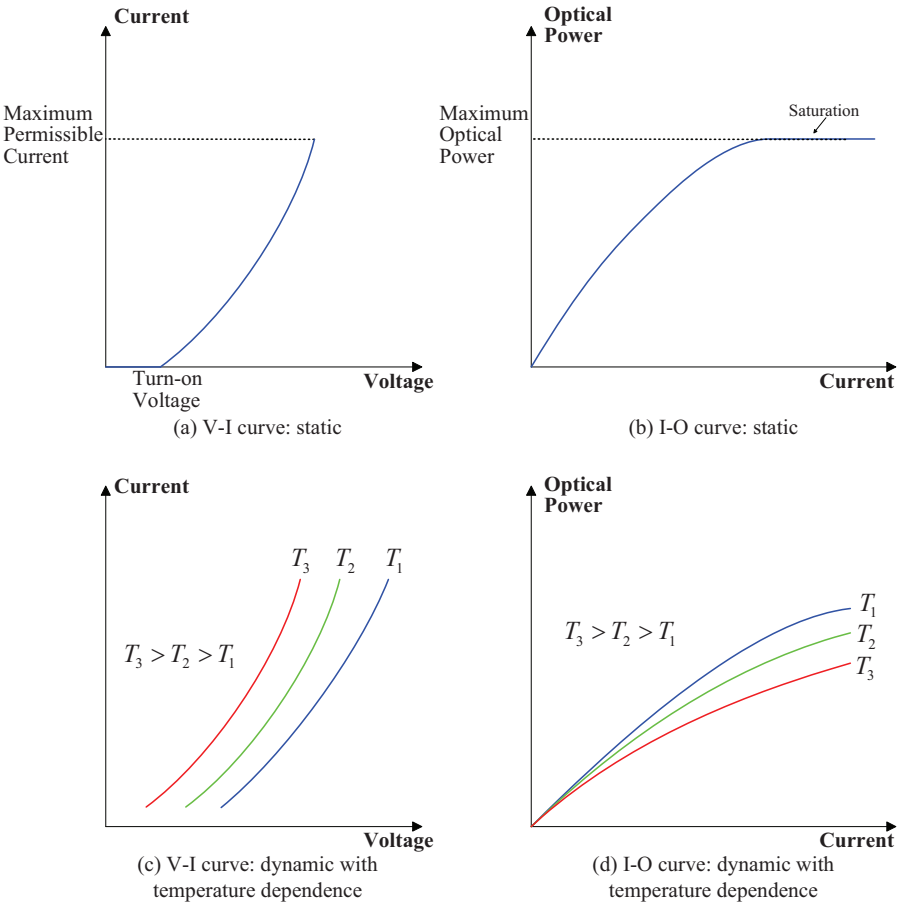

(a) V-I curve: static

(b) I-O curve: static

(c) V-I curve: dynamic with temperature dependence

(d) I-O curve: dynamic with temperature dependence

Figure 5: Nonlinearities of LED.

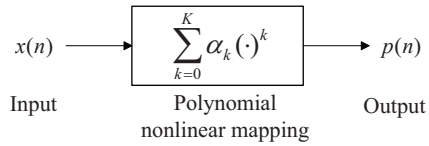

(a) Memory-less polynomial model

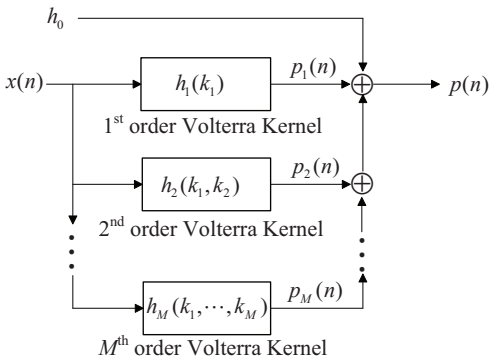

(b) Volterra model

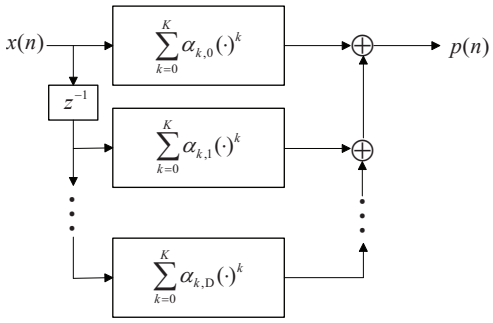

(c) Memory polynomial model

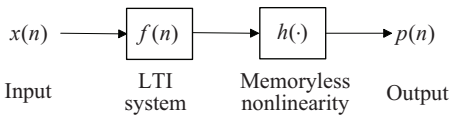

(d) Wiener model

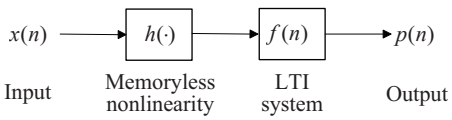

(e) Hammerstein model

Figure 6: Nonlinear models for LED.

A power series or a polynomial model is popular to describe a memory-less LED because a smooth instantaneous nonlinear transfer function can be expanded by Taylor series. Fig. 6(a) shows the input-output relationship of the memory-less polynomial model. After obtaining the measurement data of an LED, we need to figure out two sets of parameters of the polynomial model. The first one is the best polynomial order K since we truncate the Taylor series for complexity reasons. In [6, 7], authors showed that a fifth-order polynomial is adequate to model measured transfer functions and a second-order polynomial already provides a satisfying description for the devices that they tested. Second, we can use least square fitting to calculate the coefficients α_k of the polynomial. The memory-less polynomial is adequate to model the LED nonlinearities when the input signal is a narrowband signal.

Similar to the Taylor series for the memory-less nonlinear model, the Volterra series is a general approach to model a nonlinear system with memory. Since the LED has a frequency-dependent nature, memory effects cannot be ignored, especially when signal bandwidth is large. Fig. 6(b) shows the general structure of the Volterra model, where $h_m(\cdot)$ is the mth-order Volterra kernel and h_0 is a constant. The contribution of the mth order nonlinearity to the output signal can be expressed as

$$p_m(n) = \sum_{k_1=0}^{D_m} \cdots \sum_{k_m=0}^{D_m} h_m(k_1, \cdots, k_m) \times x(n-k_1) \cdots x(n-k_m), \tag{5}$$

where D_m is the memory length for the mth order nonlinear kernel and M is the nonlinear order. The authors in [15] showed that a second-order Volterra expansion can provide a fair approximation for the power spectrum up to 14 MHz. The LED nonlinearity with memory can be properly represented by the Volterra series. However, the main limitation of the Volterra model is its complexity. The number of coefficients increases exponentially as the nonlinear order and the memory length increase. Thus, the full Volterra series is not practical for real-time applications. To

avoid the complexity issue, simplifications on the Volterra series are studied.

Memory polynomial model is a special case of the Volterra model with only diagonal kernels. The general structure of the memory polynomial model is shown in Fig. 6(c). Comparing to the memory-less polynomial model, the output of the memory model depends not only on the present input, but also on past input values.

The Wiener model is another subset of the Volterra model. The Wiener model, as shown in Fig. 6(d), is constructed by a linear time-invariant (LTI) system followed by a memory-less nonlinearity. In [16], authors modeled the LED nonlinearities with a Wiener model.

Similarly, the Hammerstein model is a memory-less nonlinearity followed by an LTI system, which is opposite to the Wiener model. Fig. 6(e) shows the structure of Hammerstein model. It offers similar complexity to that of the Wiener model. Depending on the nature of the nonlinearity, the Hammerstein model can also be an appropriate model with reduced complexity.

2.1.3 Static vs. dynamic

Nonlinear models can also be classified into the static model and the dynamic model. "Static" indicates that the LED nonlinearity does not change over time. This kind of nonlinearities is relatively easy to deal with. The accuracy of the model can be improved with sufficient data collected over time. Most researches in existing literatures concentrate on the static model. However, the LED nonlinearity may change over time due to the component aging and temperature drift [4]. Hence, the dynamic model is required to capture these changes. In addition, dimming control should be supported in VLC implementation since the principal functionality of the LED is for lighting [2]. Different illumination levels result in changes in temperature, which in turn affect the system nonlinearity. Fig. 2(c) and 2(d) illustrate typical changes of both LED V-I conversion and I-O conversion under different temperature ($T_1 < T_2 < T_3$). More

specific measurements can be found in [17, 18]. Typically, at constant forward current, the driving voltage decreases at increasing LED temperature [17]. On the other hand, optical power decreases with an increase in LED temperature for the same driving current [18]. In these cases, LEDs work with time-varying nonlinearities. The mitigation techniques for LED nonlinearities will be influenced by the dynamic characteristics. Thus, careful modeling and robust mitigation methods should adapt to these dynamics. Finding robust mechanisms to model and estimate these dynamics is an open research problem.

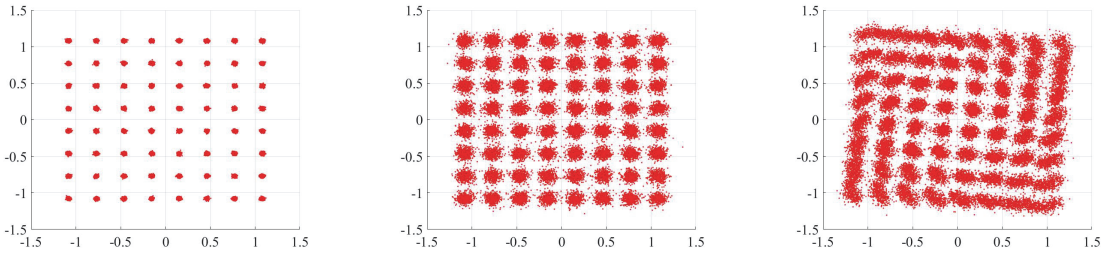

(a) Linear LED model

(b) Memory-less nonlinear LED model

(c) Memory nonlinear LED model

Figure 7: Impacts of nonlinear distortions.

2.1.4 Impact of nonlinear distortions

There are two kinds of nonlinear distortions. One is caused by the nonlinear mapping of LED electrical-to-optical conversion within the dynamic-range. The other results from the hard clipping of signals below the turn-on voltage or exceeding the maximum permissible value of the LED. The impact of the soft nonlinear mapping has been extensively discussed in [6–8]. Authors in [14] studied the clipping noise. To illustrate the impact of the nonlinear distortion as well as the memory effects, we compare constellation diagrams among three cases: (i) linear LED model; (ii) memory-less nonlinear LED model (polynomial model); (iii) nonlinear LED model with memory (Wiener model). In the simulation, a DC-biased optical OFDM (DCO-OFDM) VLC system with uncoded 64-quadrature amplitude modulation (QAM) is

tested. The memory-less nonlinearity is modeled by a polynomial model ($K = 5$, $\alpha_1 = 1.3985$, $\alpha_2 = 0.0269$, $\alpha_3 = -1.8732$, $\alpha_4 = -0.0387$ and $\alpha_5 = 1.0001$). For the case with memory effects, an LTI block ($F(z) = 1 + 0.15z^{-1} + 0.1z^{-2}$) is added before the memory-less nonlinearity. A line-of-sight (LOS) channel with an additive white Gaussian noise (AWGN) is applied. The simulation results are shown in Fig. 7(a), (b), and (c), respectively. Compare Fig. 7(a) and Fig. 7(b), we observe that the nonlinear distortion created by the memory-less nonlinearity is obvious. The distortion is larger than the mismatch created by the noise from the channel. While from Fig. 7(c), we observe that the distortion created by the nonlinearity with memory effects is severer than that with memory-less nonlinearity. The output signal is blurred and cannot be easily distinguished as data symbols.

2.2 Waveform shaping

Since nonlinear distortions degrade the system performance, the distortion mitigation is an important issue in VLC system design. The most straightforward approach is to design the signal waveform such that the signal is not sensitive to the nonlinear distortion. Another approach is to linearize the nonlinearity.

In waveform-specific mitigation techniques, the overall system nonlinear mapping is not modified. Instead, the signaling waveform is changed such that it is less sensitive to the nonlinear effect.

2.2.1 Two-level modulation

Two types of single carrier modulation methods are predominantly used in VLC: 1) amplitude modulation such as on-off keying (OOK) and M-ary pulse amplitude modulation (M-PAM); 2) pulse-position modulation (PPM) [2]. To avoid or mitigate the impact of the nonlinear distortion, OOK and PPM can be utilized since they only produce two-level signals, which are not sensitive to the nonlinearity. OOK transmits the bit 1 by "turning on" the light and transmits the bit 0 by "turning off" the light.

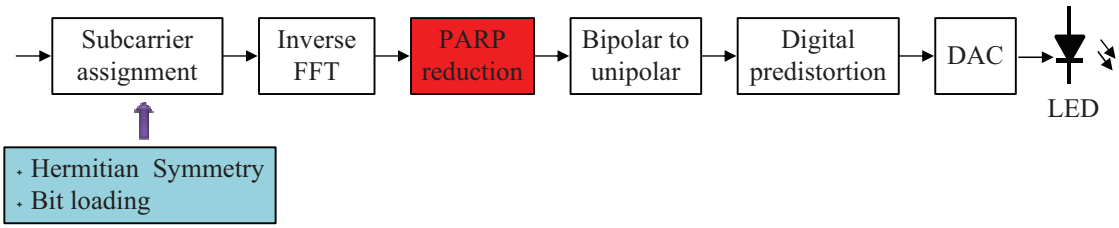

(a) VLC-OFDM transmitter front-end

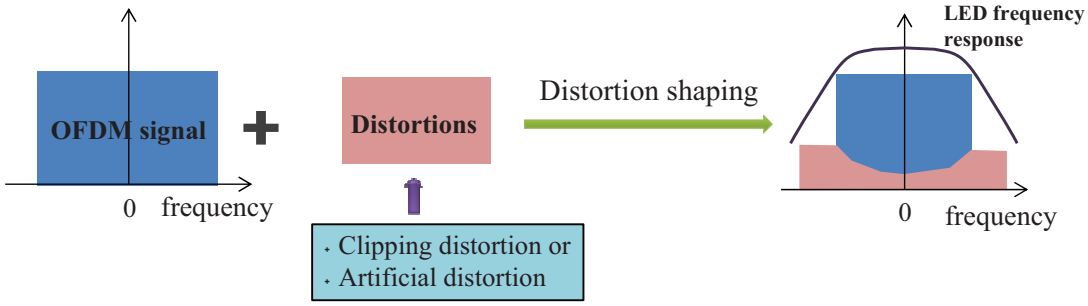

(b) PAPR reduction: distortion based

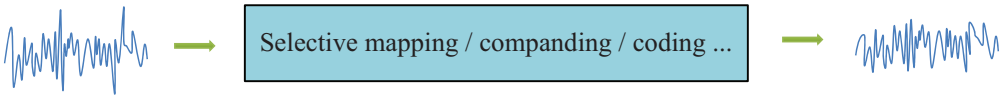

(c) PAPR reduction: side information method

Figure 8: PAPR reduction in dynamic-range-limited VLC-OFDM.

PPM encodes the information bits in the position of the pulse within a time period. 0 is represented by a positive pulse at the beginning of the period followed by a lower level pulse, and 1 is represented by a lower level pulse at the beginning of the period followed by a positive pulse. However, the main drawback of these single carrier modulation signals is their low spectrum utilization efficiency and transmission speed. In most cases, multi-carrier modulations like discrete multitone (DMT) modulation or orthogonal frequency division multiplexing (OFDM) are preferred.

2.2.2 PAPR reduction for OFDM

OFDM has been considered for VLC due to its ability to combat inter-symbol interference (ISI) and to boost the data rate [19–23]. In addition, OFDM can support bit-loading scheme, which applies different constellations (i.e. numbers of bits) to different subcarriers based on channel conditions or system requirements [22, 23, 56]. With IM/DD techniques, the baseband signal in VLC needs to be real-valued and unipolar (positive-valued). This constraint is different from radio frequency (RF) communication systems, where the baseband signals are complex-valued. Thus, Hermitian symmetry must be satisfied in the frequency-domain, where the right half subcarriers are the conjugate of the left half subcarriers [19–23]. In addition, a DC bias can be applied to convert a bipolar signal into unipolar format. Signal with such modifications is called DC biased optical OFDM (DCO-OFDM) [14].

Meanwhile, OFDM is also known for its disadvantage of high PAPR, which makes VLC-OFDM very sensitive to the dynamic-range-limited nonlinearity of LEDs [22,23]. PAPR reduction is an indispensable module in VLC-OFDM systems. However, traditional PAPR reduction methods for RF-OFDM cannot be applied to VLC-OFDM systems directly. First, RF-OFDM baseband signal is complex-valued and has only one PAPR. But for the real-valued bipolar VLC-OFDM signal like DCO-OFDM, the baseband signal $x(n)$ before biasing is zero mean and has one maximum value

and one minimum value. The maximum value of $x(n)$ can be seen as the positive peak, and the minimum value of $x(n)$ can be seen as the negative peak. We define the positive optical PAPR as $\max x(n)/\sigma_x$ and define the negative optical PAPR as $-\min x(n)/\sigma_x$, where σ_x denotes the standard deviation of $x(n)$. Note that we put a negative sign in negative optical PAPR because the minimum value of $x(n)$ is negative and the PAPR is always positive. It is worthwhile pointing out that when we calculate σ_x, both positive points and negative points are considered. We can also use second moment version to calculate PAPRs. Actually, they are equivalent when presented by dB. The positive peak and negative peak often have distinct constraints in VLC, depending on where the signal is biased within dynamic-range of LEDs. For example, in dimming condition, the DCO-OFDM is biased at the lower part of LEDs' dynamic-range, and thus the negative peak is more sensitive to the nonlinear distortions than the positive peak. In this case, we need to reduce more negative optical PAPR. Second, in VLC-OFDM systems, since LED acts as a low-pass filter and there is no out-of-band application, we do not need to consider the out-of-band interferences. This actually gives us additional degrees of freedom to design PAPR reduction schemes for VLC-OFDM systems.

2.2.2.1 Distortion-based

Distortion-based method distorts OFDM signals when reducing the PAPR. The benefit is that receiver side modifications are avoided, so that distortion-based method is practical for its low complexity. Clipping is the simplest distortion-based method to reduce the PAPR of OFDM signals. For real-valued OFDM signals, a pair of positive clipping level and negative clipping level are preset to serve as thresholds. All the time-domain signals that are beyond the thresholds will be set equal to them. Clipping generates distortions on all subcarriers in frequency-domain. If we only measure the signal-to-distortion ratio at the transmitter, clipping definitely degrades

the performance. However, if we take channel noise into consideration and measure the signal-to-noise-plus-distortion ratio, clipping may improve the effective SNR and the performance of the whole system since clipping enables larger scaling factor to the input signal. Thus, given the channel SNR, a pair of optimum clipping levels can be selected to maximize the effective SNR and achievable data rates. Generally, when channel SNR is large, more clipping distortions are allowed. When channel SNR is small, clipping distortions will dominate the noise source, thus mild clippings are favored.

The relative amounts for positive clipping and negative clipping are determined by the biasing level, or illumination scenario. If the OFDM signal is biased at the lower part of the dynamic-range of LED, negative peak should be clipped more severely than the positive peak, and vise versa. Besides deciding the amount of distortions, the other question is how to allocate the distortions in frequency-domain. In VLC, LEDs act as low-pass filters. Thus, for the low-frequency subcarriers, which have the strongest response, high-order constellation types can be used to load more bits. For the high-frequency subcarriers, we just apply low-order constellation types like QPSK. Since high-order constellations are more sensitive to noises than low-order constellations, given certain amount of distortions allowed, the ideal case would be allocating more distortions to high-frequency subcarriers and less distortions to low-frequency subcarriers. However, in simple clipping method, although we can control the total amount of distortions by adjusting the clipping thresholds, we are not able to determine the spectral shape of clipping distortions. Actually, the clipping distortions are almost equally distributed on all in-band subcarriers, which makes the low-frequency subcarriers with higher order modulations vulnerable to clippings noises [56]. This can degrade the performance of whole system.

This issue can be addressed by iterative clipping and noise shaping. In each iteration, after clipping the positive peak and negative peak, the clipping noises on different

subcarrier sets are scaled proportionally according to the order of modulations. After a number of iterations, more distortions will be allocated to high-frequency subcarriers [24]. To get an optimal solution, we can model a quadratically constrained linear optimization problem, in which the minimization of weighted positive optical PAPR and negative optical PAPR is set as the objective and the distortions for different subcarrier sets are constrained by different thresholds [56]. A customized interior point method can be developed for real-time implementation. Another aggressive allocation mechanism is pushing all distortions to out-of-band subcarrier, but oversampling is required.

2.2.2.2 Side-information-based

There have been a number of PAPR reduction proposals requiring receiver side modifications. Selective mapping (SLM) is one of these approaches [22]. In SLM, the phases of original OFDM frequency-domain symbols are rotated according to a predefined phase table. The phase table is assumed to be known to both transmitter and receiver. Then a mapped OFDM sequence with minimum PAPR is selected for transmission. For VLC-OFDM, the selection criteria is to minimize the maximum of weighted positive optical PAPR and negative optical PAPR. Rather than sending the selected phase sequence to the receiver, the transmitter only needs to send the index of selected phase sequence as side information. The number of bits included in side information depends on the size of phase table. At the receiver, the phase sequence is obtained by looking up the received index information from the phase table. This may be difficult to deploy in existing VLC systems. Such approaches also include companding, partial transmit sequence, tone injection, tone reservation, and coding [19, 21, 22, 26, 27].

Although the above discussions are based on DCO-OFDM signal, the PAPR reduction methods can be modified and generalized to other real-valued unipolar OFDM schemes, such as asymmetrically clipped optical OFDM (ACO-OFDM), unipolar OFDM (U-OFDM), and Flip-OFDM by considering only the positive optical PAPR.

2.3 Nonlinearity correction

Waveform-agnostic techniques mainly work by linearizing the overall system nonlinearity so that the input signal can be passed approximately undistorted within the dynamic-range. This linearization can take place at either the transmitter or the receiver.

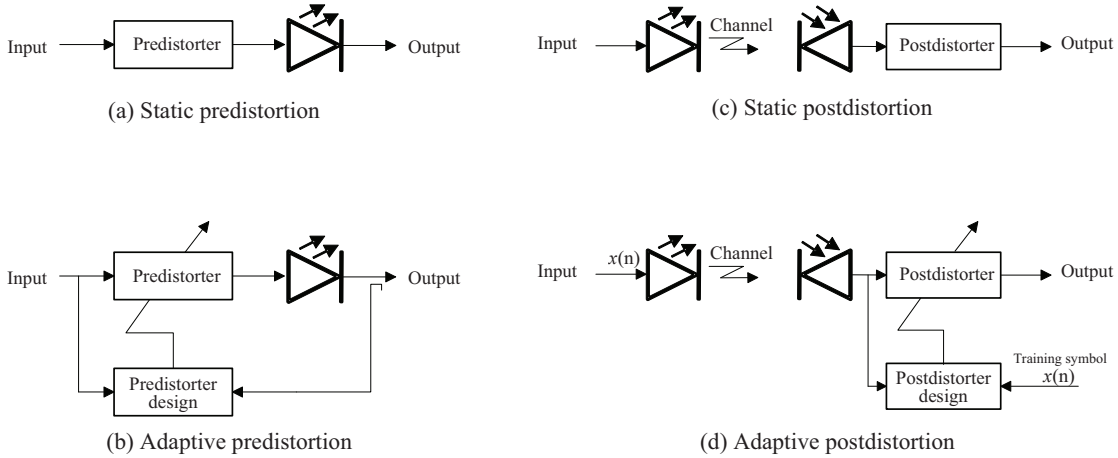

Figure 9: Waveform-agnostic mitigation methods.

2.3.1 Optimal nonlinear mapping

Recall that the LED nonlinearity belongs to a family of dynamic-range-limited nonlinearities. Different from the amplitude-limited nonlinearities in RF systems, the signal here is subject to a double-sided clipping to meet the dynamic-range constraint and a bias is always used to shift the signal to an appropriate level. In the next chapter, we will prove that the optimal nonlinear mapping in terms of signal-to-noise-plus-distortion ratio is a double-sided limiter with a certain linear gain and a certain bias

value, which can be expressed as

$$h(x) = \begin{cases} A_{min}, & x \leq \frac{A_{min}-B}{G}, \\ B + Gx, & \frac{A_{min}-B}{G} \leq x \leq \frac{A_{max}-B}{G}, \\ A_{max}, & x \geq \frac{A_{max}-B}{G}, \end{cases} \tag{6}$$

where B is the bias, G is the gain, and $[A_{min}, A_{max}]$ is the dynamic-range constraint. The choices of bias and gain values are also important. The selection of the bias can help put the most important part of the signal into the available dynamic-range. For the selection of the gain, there is a tradeoff between the signal power and the distortion. If the gain is large, the signal power is high but the distortion is severe. On the contrary, a small gain can help keep the signal less distorted but degrade the signal-to-noise ratio (SNR). Thus, the parameters require careful considerations and selections. Chapter 3 will introduce how to calculate these parameters theoretically based on the distribution of the input signal, noise power and dynamic-range constraint.

With the knowledge of the optimal nonlinear mapping, the next step is to modify the overall system mapping by predistortion or postdistortion.

2.3.2 Predistortion

To construct digital predistorters for LEDs, we can firstly identify the LED nonlinear transfer function and then find the inverse of it, so that the cascaded function is in accordance with the desired mapping that we design. This approach can be named as static predistortion. Fig. 9(a) shows a general structure of this approach. To simplify the description, we omit modulation, demodulation, DAC and ADC from the figure. In practice, for memory-less nonlinearities, the static predistorter can be easily implemented with look-up tables that map the original input constellation points to the desired locations after we know the LED nonlinearity. For nonlinearities with

memory, memory-less predistortion can only achieve limited linearization performance so that predistorters also need to have memory structures. Similar to nonlinearities modeling, the models for predistorters include the Volterra series and its special cases like the Hammerstein model and the memory polynomial model. When the system dynamic changes, the static predistortion is not suitable. Adaptive predistortion can be used.

In most cases, obtaining the inverse of a nonlinear system, especially with memory or time-varying characteristics, is not easy. Another type of approach is to model and estimate the predistorter directly from sampled data by reversing the data flow and assuming the output of the LED as the input of the predistorter and the input of the LED as the output of the predistorter. The advantage of this approach is that it eliminates the need for model assumption and parameter estimation of the LEDs.

Fig. 9(b) shows the general structure of this approach, which is also named as adaptive predistortion. The principle of the adaptive predistortion is shown as follows. We first choose the predistorter with a specific model such as memory polynomial model. Then we compare the output of the LED with the desired value so that we can adjust the parameters of the predistorter to minimize the difference. The difficulty is how to obtain the feedback of the LED output since we care about the light intensity. In RF predistortion systems, it is straightforward to tap off an electric signal after the power amplifier. However in VLC, the LED is the source of distortion and the output of the LED is light, which is harder to measure. One possible way is to put a PD beside the LED transmitter to feedback for predistorter training. However, the PD is a nonlinear device as well and the implementation cost is not favorable. For this reason, there is very little discussion of adaptive predistortion of LEDs in the literature.

2.3.3 Postdistortion

Postdistortion is a receiver-side technique to mitigate nonlinear distortion. Fig. 9(c) and (d) show the general structures of the static postdistortion and the adaptive postdistortion techniques. Similar to the static predistoriton, the static postdistortion only takes the off-line data of the nonlinearity and cannot support the LED nonlinearity dynamics. For dynamic postdistortion, no additional feedback physical circuits are needed like adaptive predistortion. In [28], compensation of an LED nonlinearity is achieved by means of Volterra receivers. Authors in [16] proposed an adaptive postdistortion technique with memory polynomial model and improved the system performance. Postdistortion can also be combined with frequency-domain equalization (FDE) to compensate for the memory effect caused by non-flat frequency response of LED [29].

In most cases, only the line-of-sight (LOS) link is considered for channel modeling since it is usually much stronger than the diffuse link. In addition, the signal bandwidth is narrow due to the limited LED response. Thus, the frequency response of IM/DD channel is relatively flat. However, if we consider multipath effects or the modulation bandwidth is relatively broad, then the channel response is no longer flat. In this case, pre-equalization or post-equalization may be necessary to be combined with predistortion or postdistortion to compensate for the channel response.

2.4 Conclusion

In this chapter, we summarize topics related to the LED nonlinearity distortion mitigation in VLC. First, we show different ways to model the LED nonlinearity, including memory-less/memory models and static/dynamic models. LED memory effects and time-varying dynamics should be taken into account to model the nonlinearity and design mitigation techniques, especially for high-speed transmission. Then, we present two major approaches for the mitigation techniques: the waveform-specific

mitigation and the waveform-agnostic mitigation. The waveform-specific mitigation focuses on how to select the signal waveforms to reduce the nonlinear distortions. The waveform-agnostic mitigation compensates for the nonlinear distortion with linearization methods. We show the optimal nonlinear mapping for the VLC system and then study how to linearize the overall system by predistortion and postdistortion. Additionally, both static and adaptive approaches are discussed. The nonlinear distortion mitigation is crucial in the future high-speed VLC system design. The dynamic characteristics caused by the device nature, environmental changes and illumination requirements can not be ignored. The designing of the robust mitigation techniques catching these dynamics is of value and challenge. Another challenge of the future work lies in the hardware implementation of these mitigation techniques, especially the adaptive predistorter and postdistorter.

CHAPTER III

OPTIMIZATION OF SIGNAL-TO-NOISE-PLUS-DISTORTION RATIO FOR DYNAMIC-RANGE-LIMITED NONLINEARITIES

Many components used in signal processing and communication applications, such as power amplifiers and analog-to-digital converters, are nonlinear and have a finite dynamic-range. The nonlinearity associated with these devices distorts the input, which can degrade the overall system performance. Signal-to-noise-plus-distortion ratio (SNDR) is a common metric to quantify the performance degradation. One way to mitigate nonlinear distortions is by maximizing the SNDR. In this chapter, we analyze how to maximize the SNDR of the nonlinearities in optical wireless communication (OWC) systems. Specifically, we answer the question of how to optimally predistort a double-sided memory-less nonlinearity that has both a "turn-on" value and a maximum "saturation" value. We show that the SNDR-maximizing response given the constraints is a double-sided limiter with a certain linear gain and a certain bias value. Both the gain and the bias are functions of the probability density function (PDF) of the input signal and the noise power. We also find a lower bound of the nonlinear system capacity, which is given by the SNDR and an upper bound determined by dynamic signal-to-noise ratio (DSNR). An application of the results herein is to design predistortion linearization of nonlinear devices like light emitting diodes (LEDs).

3.1 Introduction

In addition to being nonlinear, many components in a signal processing or communication system have a dynamic-range constraint. For example, light emitting diodes (LEDs) are dynamic-range-constrained devices that appear in intensity modulation (IM) and direct detection (DD) based optical wireless communication (OWC) systems [1, 2]. To drive an LED, the input electric signal must be positive and exceed the turn-on voltage of the device. On the other hand, the signal is also limited by the saturation point or maximum permissible value of the LED. Thus, the dynamic-range constraint can be modeled as two-sided clipping. The same situation may happen in other applications such as digital audio processing [30].

Both nonlinearity and clipping result in distortions which may cause system performance degradation. Signal-to-noise-plus-distortion ratio (SNDR) is a commonly used metric to quantify the distortion that is uncorrelated with the signal [31–34]. Previous work in this area mainly concentrated on a family of amplitude-limited nonlinearities that is common in radio frequency (RF) system design involving nonlinear components such as power amplifiers (PAs) and mixers.

Different from the previous work, our study discusses the class of nonlinearities with a two-sided dynamic-range constraint that is more commonly found in optical and acoustic systems. The authors in [10–13] illustrated the impact of LED nonlinearity and clipping noise in OWC systems. Some predistortion strategies were proposed in [35–37]. However, to the best of our knowledge, the optimal nonlinear mapping under the two-sided dynamic-range constraint has not been studied.

We consider two major differences from amplitude-limited nonlinearity. First, the signal will be subject to turn-on clipping and saturation clipping to meet the dynamic-range constraint. Second, dc biasing must be used to shift the signal to an appropriate level to minimize distortion. In this chapter, we will show that the ideal linearizer that maximizes the SNDR is a double-sided limiter that has an affine

response. The parameters of the response can be calculated from the distribution of the input signal and the noise power.

In addition to deriving the SNDR-optimal predistorter, we also relate a lower bound on channel capacity to the SNDR, further motivating the SNDR considerations. Finally, we employ another common distortion metric, dynamic signal-to-noise ratio (DSNR) to provide an upper bound on the double-sided clipping channel.

The remainder of this chapter is organized as follows: Section 3.2 introduces the system model for dynamic-range-limited nonlinearity and the corresponding SNDR definition. In Section 3.3, we derive the optimal nonlinear mapping that maximizes the SNDR and illustrate some examples. In Section 3.4, we relate the SNDR to the capacity of the nonlinear channel. Finally, Section 3.5 concludes the chapter. Detailed proofs in this chapter are deferred to the Appendices.

3.2 System model and SNDR definition

3.2.1 System model

Let us consider a system modeled by

$$y_{\mathrm{o}}(t) = h_{\mathrm{o}}[x_{\mathrm{o}}(t)] + v(t) \tag{7}$$

where $x_{\mathrm{o}}(t)$ is a real-valued signal with mean μ_x and variance σ_x^2; $v(t)$ is a zero-mean additive noise process with variance σ_v^2; $h_{\mathrm{o}}(\cdot)$ is a memory-less nonlinear mapping with dynamic-range constraint $A_1 \leq h_{\mathrm{o}}[x_{\mathrm{o}}(t)] \leq A_2$.

For notational simplicity, we omit the t-dependence in the memory-less system and replace $h_{\mathrm{o}}(\cdot)$ and $x_{\mathrm{o}}(t)$ by $h(\cdot) = h_{\mathrm{o}}(\cdot) - A_1$ and $x = x_{\mathrm{o}} - \mu_x$. Then we have an equivalent system modeled by

$$y = h(x) + v \tag{8}$$

where $h(\cdot)$ is a memory-less nonlinear mapping with dynamic-range constraint $0 \leq h(x) \leq A = A_2 - A_1$ and x is a zero-mean signal with variance σ_x^2.

3.2.2 SNDR definition

According to Bussgang's Theorem [38], the nonlinear mapping in (8) can be decomposed as

$$h(x) = \alpha x + d \tag{9}$$

where d is the distortion caused by $h(\cdot)$ and α is a constant, selected so that d is uncorrelated with x, i.e., $E[xd] = 0$. Thus

$$\alpha = \frac{E[xh(x)] - E[xd]}{E[x^2]} = \frac{E[xh(x)]}{E[x^2]} = \frac{E[xh(x)]}{\sigma_x^2}. \tag{10}$$

The distortion power is given by

$$\begin{aligned} \varepsilon_d &= E[d^2] - E^2[d] \\ &= E[h^2(x)] - \alpha^2\sigma_x^2 - E^2[h(x)], \end{aligned} \tag{11}$$

where we use the notation $E^2(\cdot) = [E(\cdot)]^2$. The signal-to-noise-plus-distortion ratio (SNDR) is defined as

$$\begin{aligned} \text{SNDR} &= \frac{\alpha^2\sigma_x^2}{\varepsilon_d + \sigma_v^2} \\ &= \frac{E^2[xh(x)]/\sigma_x^2}{E[h^2(x)] - E^2[xh(x)]/\sigma_x^2 - E^2[h(x)] + \sigma_v^2}. \end{aligned} \tag{12}$$

The definition of SNDR here is a little bit different from that in [34], because all the signals are real and the distortion contains dc biasing. Thus, the distortion power is modeled as variance rather than the second moment.

We see from (12) that the SNDR is related to the distribution of x, the noise power σ_v^2, and the nonlinear mapping $h(\cdot)$. Our aim in the next section is to determine the function $h(\cdot)$ that maximizes the SNDR given a signal distribution and the two-sided clipping constraint.

3.3 SNDR optimization and examples

3.3.1 Optimization of SNDR

Similar to [34], let us use a function $g(\cdot)$ to normalize the nonlinear mapping $h(\cdot)$:

$$h(x) = Ag\left(\frac{x}{\sigma_x}\right) \tag{13}$$

where $0 \leq g(\cdot) \leq 1$. Let $\gamma = x/\sigma_x$ and substitute (13) into (12) to obtain

$$\begin{aligned} \text{SNDR} &= \frac{E^2[\gamma g(\gamma)]}{E[g^2(\gamma)] - E^2[\gamma g(\gamma)] - E^2[g(\gamma)] + \sigma_v^2/A^2} \\ &= \frac{E^2[\gamma g(\gamma)]}{\text{var}[g(\gamma)] - E^2[\gamma g(\gamma)] + \sigma_v^2/A^2} \end{aligned} \tag{14}$$

where $\text{var}[g(\gamma)] = E[g^2(\gamma)] - E^2[g(\gamma)]$ is the variance of $g(\gamma)$.

The SNDR optimization problem can be stated as follows:

$$\max_{\substack{g(\cdot) \\ 0 \leq g(\cdot) \leq 1}} \quad \text{SNDR} \tag{15}$$

for a given distribution of γ, dynamic-range A and noise power σ_v^2.

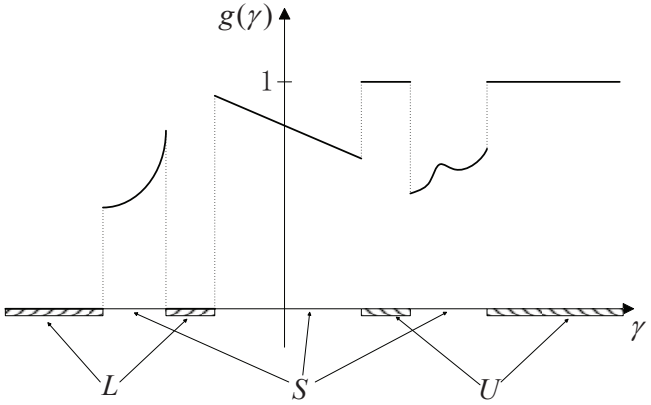

Figure 10: An example of nonlinear mapping $g(\cdot)$ that satisfies the $0 \leq g(\cdot) \leq 1$ constraint.

Fig. 10 illustrates an example of the $g(\cdot)$, where the region of γ is divided into three sets L, S and U:

$$g(\gamma) = 0, \quad \text{for} \quad \gamma \in L; \tag{16}$$

$$0 < g(\gamma) < 1, \quad \text{for} \quad \gamma \in S; \tag{17}$$

$$g(\gamma) = 1, \quad \text{for} \quad \gamma \in U. \tag{18}$$

Thus, to determine a nonlinear mapping $g(\cdot)$, we need to find the sets L, S, U and the shape of the function $g(\cdot)$ in S.

We will solve this problem with the following steps:

1. find the optimal $g(\cdot)$ given L, S, U;

2. show that S should be as large as possible;

3. determine L and U for the optimal solution.

Lemma 1. Assume that the sets L, S and U are known, and $L \cup S \cup U = R$. The $g(\cdot)$ function that maximizes the SNDR expression in (14) is of the form

$$g(\gamma) = \frac{\gamma}{\eta} + \beta \tag{19}$$

where

$$\begin{aligned} \eta &= \frac{C_0^U C_1^S + C_1^U - C_0^S C_1^U}{C_0^U - C_0^U C_0^S - (C_0^U)^2 + (1 - C_0^U)\sigma_v^2/A^2} \\ &= \frac{C_0^U C_1^S + C_1^U - C_0^S C_1^U}{C_0^U C_0^L + (1 - C_0^S)\sigma_v^2/A^2}, \end{aligned} \tag{20}$$

$$\beta = \frac{C_0^U C_1^S + C_0^U C_1^U + C_1^S \sigma_v^2/A^2}{C_0^U C_1^S + C_1^U - C_0^S C_1^U} \tag{21}$$

with

$$C_{\text{num}}^{\text{set}} = E[\gamma^{\text{num}} I_{\text{set}}(\gamma)] \tag{22}$$

and $I_{\text{set}}(\gamma)$ is the indicator function:

$$I_{\text{set}}(\gamma) = \begin{cases} 1, & \text{if } \gamma \in \text{set}, \\ 0, & \text{otherwise.} \end{cases} \tag{23}$$

This lemma holds if and only if S satisfies $0 < \frac{\gamma}{\eta} + \beta < 1$ for all $\gamma \in S$.

Proof See Appendix A.

This result rules out $g(\cdot)$ functions whose shape over S is nonlinear. Fig. 11 demonstrates examples of $g(\cdot)$ functions that may satisfy Lemma 1. Here, the slope of the linear curve in S can be either positive or negative.

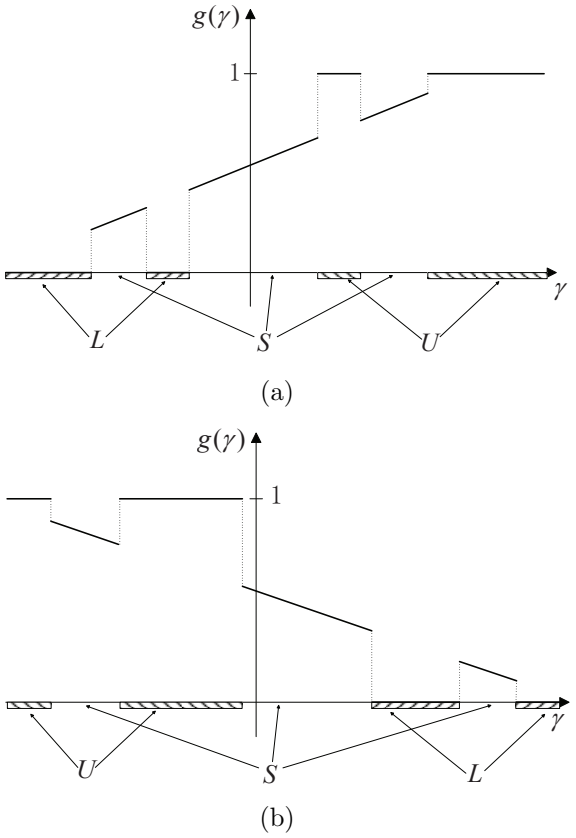

Figure 11: Examples of nonlinear mapping $g(\cdot)$ that may satisfy Lemma 1. (a) $\eta > 0$. (b) $\eta < 0$.

Lemma 1 answered the question pertaining to the best shape of the $g(\cdot)$ function with given L, S and U. The remaining question is how to determine the optimal sets L, S and U so that the SNDR is maximum. This turns out to be a very challenging problem since we are seeking joint optimization over multiple sets. Let us consider S first.

Lemma 2. Given sets L, S and U, if S can be enlarged to S^* such that $S \subset S^* \subseteq$

$(-\beta^*\eta^*, \eta^* - \beta^*\eta^*)$ or $(\eta^* - \beta^*\eta^*, -\beta^*\eta^*)$, then a higher SNDR can be achieved.

Proof See Appendix B.

Fig. 12 shows how Lemma 2 works. S in Fig. 12(a) can be enlarged by occupying the subsets of L and U as in Fig. 12(b). The larger the set S, the better the SNDR that can be achieved. Just as in Lemma 1, Lemma 2 holds if and only if S^* satisfies $0 < \frac{\gamma}{\eta^*} + \beta^* < 1$ for all $\gamma \in S^*$, that is, $S^* \subseteq (-\beta^*\eta^*, \eta^* - \beta^*\eta^*)$ or $(\eta^* - \beta^*\eta^*, -\beta^*\eta^*)$.

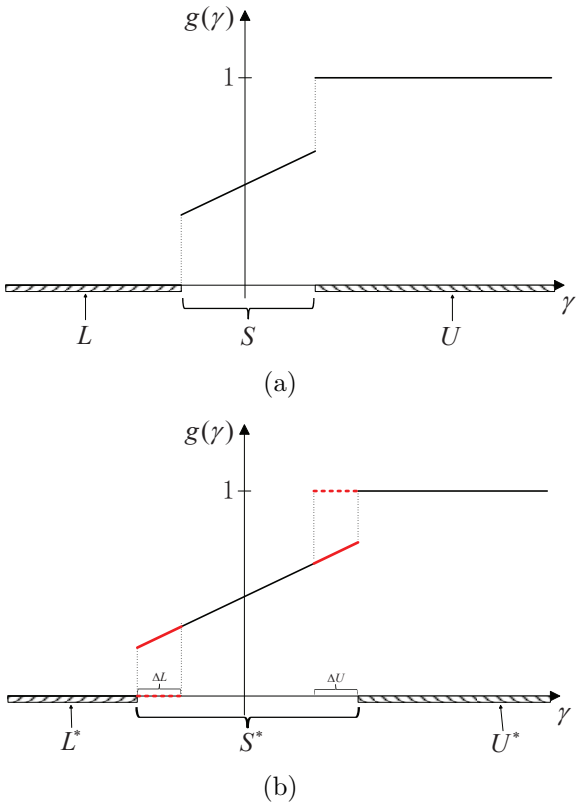

Figure 12: Illustration of Lemma 2. (a) L, S, U. (b) $L^* = L - \Delta L$, $S^* = S + \Delta L + \Delta U$, $U^* = U - \Delta U$.

Even with the set S determined, we still need to determine L and U.

Lemma 3. If $\eta > 0$, the $g(\cdot)$ that maximizes the SNDR satisfies $L \subset \mathbb{R}^-$ and $U \subset \mathbb{R}^+$; if $\eta < 0$, the $g(\cdot)$ that maximizes the SNDR satisfies $L \subset \mathbb{R}^+$ and $U \subset \mathbb{R}^-$.

Proof Let us compare the SNDR between Fig. 13(a) and Fig. 13(b). For $\eta > 0$, if there is a subset ΔL of L in $\mathbb{R}^+$ or a subset ΔU of U in $\mathbb{R}^-$, which is illustrated in Fig. 13(b), then we see that $E^2[\gamma g(\gamma)]$ is decreased while the variance of $g(\gamma)$ is increased. Thus, the SNDR $= \frac{E^2[\gamma g(\gamma)]}{\text{var}[g(\gamma)]-E^2[\gamma g(\gamma)]+\sigma_v^2/A^2}$ of Fig. 13(b) is less than the SNDR of Fig. 13(a). Similarly, we can draw the same conclusion for the case with $\eta < 0$.

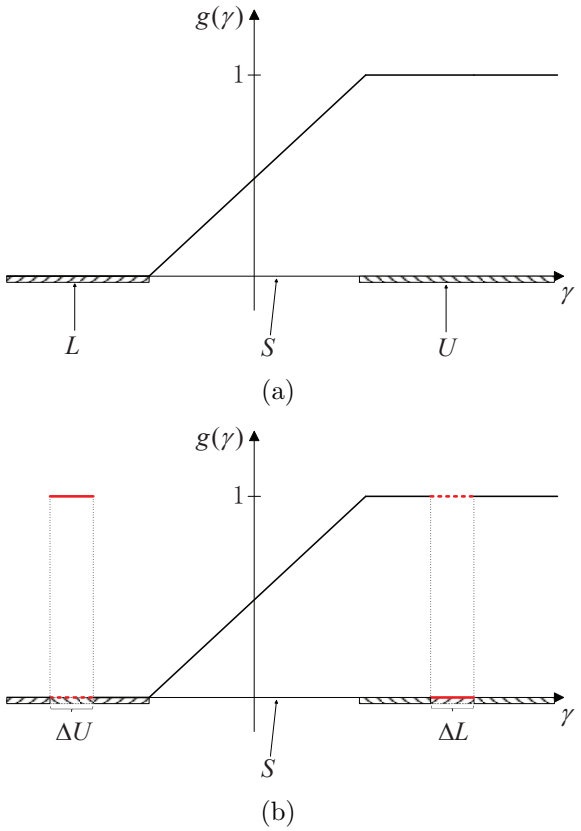

Figure 13: Illustration of Lemma 3. (a) $L \subset \mathbb{R}^-$, $U \subset \mathbb{R}^+$. (b) $\Delta L \subset \mathbb{R}^+$, $\Delta U \subset \mathbb{R}^-$.

In the final analysis, Lemma 1, 2, 3 imply that the optimal L, S and U, in the sense of maximizing the SNDR, are $L = (-\infty, -\beta\eta]$, $S = (-\beta\eta, \eta - \beta\eta)$ and $U = [\eta - \beta\eta, +\infty)$ if $\eta > 0$; or $L = [-\beta\eta, +\infty)$, $S = (\eta - \beta\eta, -\beta\eta)$ and $U = [-\infty, \eta - \beta\eta)$ if $\eta < 0$.

Theorem 1. Within the class of $g(\cdot)$ satisfying $0 \leq g(\cdot) \leq 1$, the following $g(\cdot)$ maximizes the SNDR expression in (14):

$$g(\gamma) = \begin{cases} 0, & \gamma \leq -\beta^\star\eta^\star, \\ \frac{\gamma}{\eta^\star} + \beta^\star, & -\beta^\star\eta^\star \leq \gamma \leq \eta^\star - \beta^\star\eta^\star, \\ 1, & \gamma \geq \eta^\star - \beta^\star\eta^\star \end{cases} \tag{24}$$

for $\eta^\star > 0$, or

$$g(\gamma) = \begin{cases} 1, & \gamma \leq \eta^\star - \beta^\star\eta^\star, \\ \frac{\gamma}{\eta^\star} + \beta^\star, & \eta^\star - \beta^\star\eta^\star \leq \gamma \leq -\beta^\star\eta^\star, \\ 0, & \gamma \geq -\beta^\star\eta^\star \end{cases} \tag{25}$$

for $\eta^\star < 0$, where the $\eta^\star$ and $\beta^\star$ are found by solving the following transcendental equations:

$$\eta^\star = \frac{C_0^{U^\star} C_1^{S^\star} + C_1^{U^\star} - C_0^{S^\star} C_1^{U^\star}}{C_0^{U^\star} C_0^{L^\star} + (1 - C_0^{S^\star})\sigma_v^2/A^2}, \tag{26}$$

$$\beta^\star = \frac{C_0^{U^\star} C_1^{S^\star} + C_0^{U^\star} C_1^{U^\star} + C_1^{S^\star}\sigma_v^2/A^2}{C_0^{U^\star} C_1^{S^\star} + C_1^{U^\star} - C_0^{S^\star} C_1^{U^\star}} \tag{27}$$

with

$$C_0^{U^\star} = \begin{cases} \int_{\eta^\star - \beta^\star\eta^\star}^{+\infty} p(\gamma)d\gamma, & \text{for } \eta^\star > 0, \\ \int_{-\infty}^{\eta^\star - \beta^\star\eta^\star} p(\gamma)d\gamma, & \text{for } \eta^\star < 0; \end{cases} \tag{28}$$

$$C_0^{S^\star} = \begin{cases} \int_{-\beta^\star\eta^\star}^{\eta^\star - \beta^\star\eta^\star} p(\gamma)d\gamma, & \text{for } \eta^\star > 0, \\ \int_{\eta^\star - \beta^\star\eta^\star}^{-\beta^\star\eta^\star} p(\gamma)d\gamma, & \text{for } \eta^\star < 0; \end{cases} \tag{29}$$

$$C_0^{L^\star} = \begin{cases} \int_{-\infty}^{-\beta^\star\eta^\star} p(\gamma)d\gamma, & \text{for } \eta^\star > 0, \\ \int_{-\beta^\star\eta^\star}^{\infty} p(\gamma)d\gamma, & \text{for } \eta^\star < 0; \end{cases} \tag{30}$$

$$C_1^{U^\star} = \begin{cases} \int_{\eta^\star-\beta^\star\eta^\star}^{+\infty} \gamma p(\gamma) d\gamma, & \text{for } \eta^\star > 0, \\ \int_{-\infty}^{\eta^\star-\beta^\star\eta^\star} \gamma p(\gamma) d\gamma, & \text{for } \eta^\star < 0; \end{cases} \tag{31}$$

$$C_1^{S^\star} = \begin{cases} \int_{-\beta^\star\eta^\star}^{\eta^\star-\beta^\star\eta^\star} \gamma p(\gamma) d\gamma, & \text{for } \eta^\star > 0, \\ \int_{\eta^\star-\beta^\star\eta^\star}^{-\beta^\star\eta^\star} \gamma p(\gamma) d\gamma, & \text{for } \eta^\star < 0 \end{cases} \tag{32}$$

and $p(\gamma)$ is the probability density function (PDF) of γ. The optimal SNDR is found as

$$\text{SNDR}^\star = \frac{1}{\frac{1}{R(\eta^\star,\beta^\star)} - 1} \tag{33}$$

where

$$R(\eta^\star, \beta^\star) = C_2^{S^\star} + \eta^\star C_1^{U^\star} + \eta^\star \beta^\star C_1^{S^\star} \tag{34}$$

and

$$C_2^{S^\star} = \begin{cases} \int_{-\beta^\star\eta^\star}^{\eta^\star-\beta^\star\eta^\star} \gamma^2 p(\gamma) d\gamma, & \text{for } \eta^\star > 0, \\ \int_{\eta^\star-\beta^\star\eta^\star}^{-\beta^\star\eta^\star} \gamma^2 p(\gamma) d\gamma, & \text{for } \eta^\star < 0. \end{cases} \tag{35}$$

Proof See the proofs of Lemma 1, 2, 3.

Theorem 1 establishes that the nonlinearity in the shape of Fig. 14 is optimal.

Predistortion is a well-known linearization strategy in many applications such as RF amplifier linearization. For dynamic-range-constrained nonlinearities like LED electrical-to-optical conversion, predistortion has been proposed to mitigate the nonlinear effects. Specifically, given a system nonlinearity $u(\cdot)$, it is possible to apply a predistortion mapping $f(\cdot)$ so the overall response is linear. According to Theorem 1, it is best to make $u[f(\cdot)]$ equal to the $g(\cdot)$ function given in (24) or (25) if $u(\cdot)$ is normalized with dynamic-range constraint $0 \leq u(\cdot) \leq 1$. Using the analytical tools presented above, we can answer the questions regarding the selection of the gain factor

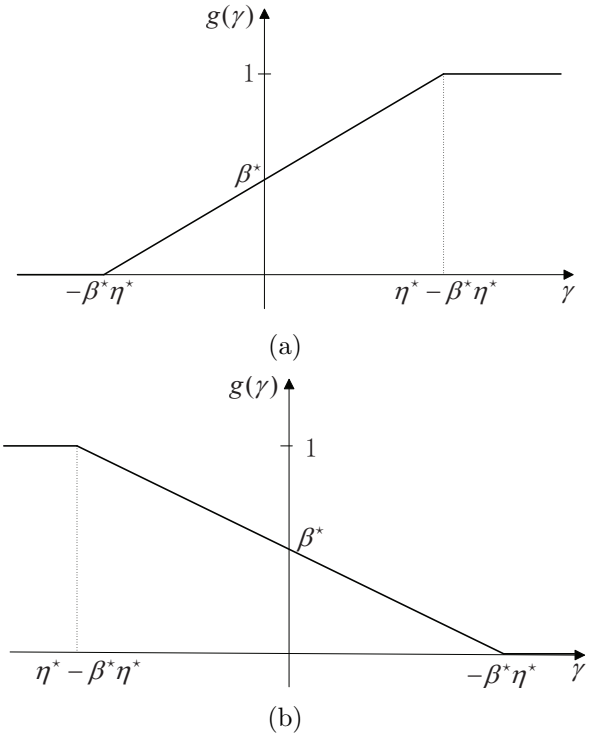

Figure 14: Illustration of optimal $g(\cdot)$ functions to maximize the SNDR. (a) $\eta^\star > 0$. (b) $\eta^\star < 0$.

$1/\eta$, dc biasing β, and the clipping regions on both sides, or equivalently, the sets L and U. Theorem 1 shows that these optimal parameters (in terms of SNDR) depend on the PDF of γ and the dynamic signal-to-noise ratio DSNR $= A^2/\sigma_v^2$. Thus, our work can serve as a guideline for the system design. In the next subsection, examples are given to illustrate the calculations of the optimal factors $\eta^\star$ and $\beta^\star$.

3.3.2 Examples for selections of optimal parameter values

In the last subsection, we learned that the optimal factors $\eta^\star$ and $\beta^\star$ can be calculated by solving two transcendental equations (26) and (27). However, there may not be closed-form expressions for the solutions. Additionally, solving (26) and (27) may result in multiple solutions, but we only keep the real-valued ones since all the signals here are real-valued. Moreover, we need to check and make sure that $U \bigcap W \neq \emptyset$ and $L \bigcap W \neq \emptyset$, where W is the feasible set of the input signal γ.

Here, let us take into account a specific class of input signals whose distributions exhibit axial symmetry, such as uniform and Gaussian distributions. When the distribution of the input signal is axially symmetric, the optimal clipping regions $L^\star$ and $U^\star$ are also symmetric. Thus, $C_0^{U^\star} = C_0^{L^\star}$, $C_1^{U^\star} = -C_1^{L^\star}$ and $C_1^{S^\star} = 0$. Then, the factors $\beta^\star$ and $\eta^\star$ can be calculated:

$$\beta^\star = \frac{C_0^{U^\star} C_1^{U^\star}}{C_0^{U^\star} C_1^{U^\star} + C_0^{L^\star} C_1^{U^\star}} = 0.5, \tag{36}$$

$$\eta^\star = \frac{2C_0^{U^\star} C_1^{U^\star}}{(C_0^{U^\star})^2 + 2C_0^{U^\star}\sigma_v^2/A^2} = \frac{2C_1^{U^\star}}{C_0^{U^\star} + 2\sigma_v^2/A^2}. \tag{37}$$

We see that the dc biasing will be the midpoint of the dynamic-range. When $\eta^\star > 0$, it can be further expressed as

$$\eta^\star = \frac{2\int_{0.5\eta^\star}^{+\infty} \gamma p(\gamma) d\gamma}{\int_{0.5\eta^\star}^{+\infty} p(\gamma) d\gamma + 2\sigma_v^2/A^2} \tag{38}$$

and when $\eta^\star < 0$, it can be expressed as

$$\eta^\star = \frac{2\int_{-\infty}^{0.5\eta^\star} \gamma p(\gamma) d\gamma}{\int_{-\infty}^{0.5\eta^\star} p(\gamma) d\gamma + 2\sigma_v^2/A^2}. \tag{39}$$

There is still no closed-form expression for the gain factor $\eta^\star$. Next, as examples, let us consider specific calculations for uniform and Gaussian distributions.

Example 1. When the original signal $x_{\mathrm{o}}(t)$ is uniformly distributed in the interval $[\mu_x - b, \mu_x + b]$, we infer that the normalized signal γ is uniformly distributed in the interval $[-\sqrt{3}, \sqrt{3}]$ with the PDF

$$p(\gamma) = \begin{cases} \frac{1}{2\sqrt{3}}, & -\sqrt{3} \le \gamma \le \sqrt{3}, \\ 0, & \text{otherwise.} \end{cases} \tag{40}$$

For the case of $\eta^\star > 0$, it is straightforward to calculate

$$C_1^{U^\star} = \int_{0.5\eta^\star}^{\sqrt{3}} \gamma \frac{1}{2\sqrt{3}} d\gamma = \frac{1}{4\sqrt{3}}(3 - \frac{1}{4}\eta^{\star 2}), \tag{41}$$

$$C_0^{U^\star} = \int_{0.5\eta^\star}^{\sqrt{3}} \frac{1}{2\sqrt{3}} d\gamma = \frac{\sqrt{3} - 0.5\eta^\star}{2\sqrt{3}}. \tag{42}$$

Substituting (41) and (42) into (38), we obtain

$$\eta^\star = \frac{\frac{1}{2\sqrt{3}}(3 - \frac{1}{4}\eta^{\star 2})}{\frac{\sqrt{3}-0.5\eta^\star}{2\sqrt{3}} + 2\sigma_v^2/A^2} \tag{43}$$

which can be rewritten as a quadratic equation

$$\eta^{\star 2} - (16\sqrt{3}\sigma_v^2/A^2 + 4\sqrt{3})\eta^\star + 12 = 0. \tag{44}$$

Thus, we obtain a closed-form solution for the optimal $\eta^\star$:

$$\eta^\star = 8\sqrt{3}\sigma_v^2/A^2 + 2\sqrt{3} - 4\sqrt{12\sigma_v^4/A^4 + 6\sigma_v^2/A^2}. \tag{45}$$

We know that there should be two solutions to (44). In fact, the other solution is $0.5\eta^\star > \sqrt{3}$, which means that both $C_0^{U^\star}$ and $C_1^{U^\star}$ are 0. Thus, the solution given by (45) is the unique optimal selection for the gain factor $\eta^\star > 0$. If $\eta^\star < 0$ is desired, the optimal solution is

$$\eta^\star = -8\sqrt{3}\sigma_v^2/A^2 - 2\sqrt{3} + 4\sqrt{12\sigma_v^4/A^4 + 6\sigma_v^2/A^2}. \tag{46}$$

Example 2. When the original signal $x_{\rm o}(t)$ is Gaussian distributed, then the normalized signal γ has a standard Gaussian distribution with the PDF

$$p(\gamma) = \frac{1}{\sqrt{2\pi}} e^{-\frac{1}{2}\gamma^2}. \tag{47}$$

For the case of $\eta^\star > 0$, we have

$$C_1^{U^\star} = \int_{0.5\eta^\star}^{+\infty} \gamma \frac{1}{\sqrt{2\pi}} e^{-\frac{1}{2}\gamma^2} = \frac{1}{\sqrt{2\pi}} e^{-\frac{1}{8}\eta^{\star 2}}, \tag{48}$$

$$C_0^{U^\star} = \frac{1}{2} - \frac{1}{2}\mathrm{erf}\left(\frac{\eta^\star}{2\sqrt{2}}\right) \tag{49}$$

where erf$(\cdot)$ is the error function with the definition

$$\text{erf}(z) = \frac{1}{\sqrt{\pi}} \int_{-z}^{z} e^{-\gamma^2} d\gamma. \tag{50}$$

Substituting (48) and (49) into (38) and simplifying, we obtain

$$\eta^\star \left[\frac{1}{2} - \frac{1}{2}\text{erf}\left(\frac{\eta^\star}{2\sqrt{2}} \right) + \frac{2\sigma_v^2}{A^2} \right] = \frac{2}{\sqrt{2\pi}} e^{-\frac{1}{8}\eta^{\star 2}}. \tag{51}$$

Here the optimal $\eta^\star$ does not have a closed-form expression, but can be easily calculated numerically. We can draw a similar conclusion for the case of $\eta^\star < 0$.

Fig. 15 shows how a double-sided limiter changes a standard Gaussian signal. Various biasing and gain factors result in different clipping regions of the input signal and the power of the output signal. There is a tradeoff between the clipping distortion and the signal power when we are choosing these factors. From this section, we know how to calculate the optimal factors for the double-sided limiter.

3.3.3 Numerical results

Fig. 16 shows the optimal $\eta^\star$ as a function of DSNR for the above examples.

Next, we illustrate the SNDR of two different nonlinear mappings: $g_1(\gamma)$ is the optimal solution chosen by Theorem 1, and $g_2(\gamma)$ is a fixed mapping given below:

$$g_2(\gamma) = \begin{cases} 0, & \gamma \leq -0.4, \\ \gamma + 0.4, & -0.4 \leq \gamma \leq 0.6, \\ 1, & \gamma \geq 0.6. \end{cases} \tag{52}$$

The corresponding SNDR curves are shown in Fig. 17. This example illustrates that the nonlinearity $g_1(\gamma)$ yields a higher SNDR as compared to the other nonlinearity, as expected according to Theorem 1.

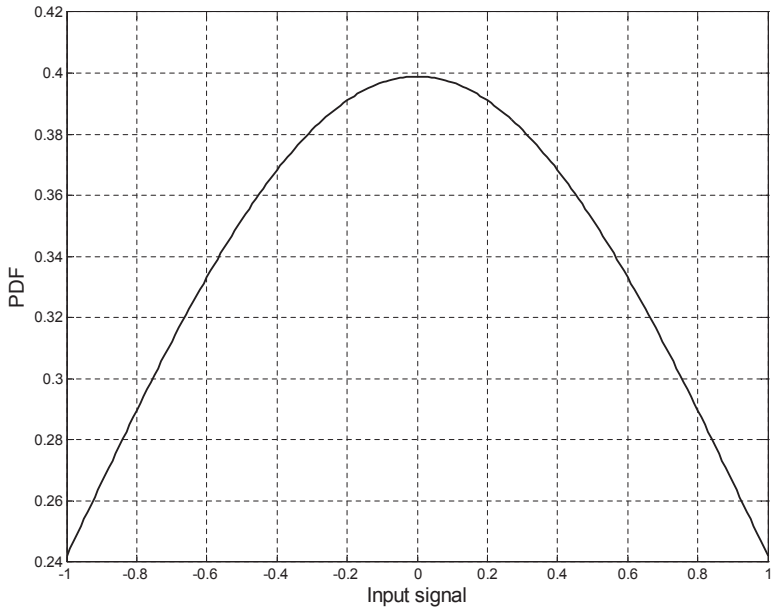

(a)

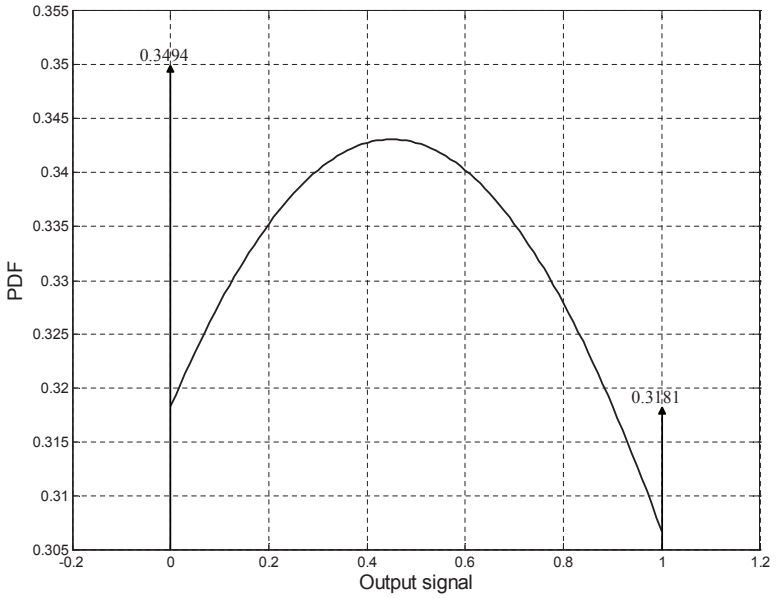

(b)

Figure 15: Illustration of a Gaussian signal passing through a double-sided limiter with $\eta = 0.86$ and $\beta = 0.45$. (a) Signal before nonlinear mapping. (b) Signal after nonlinear mapping.

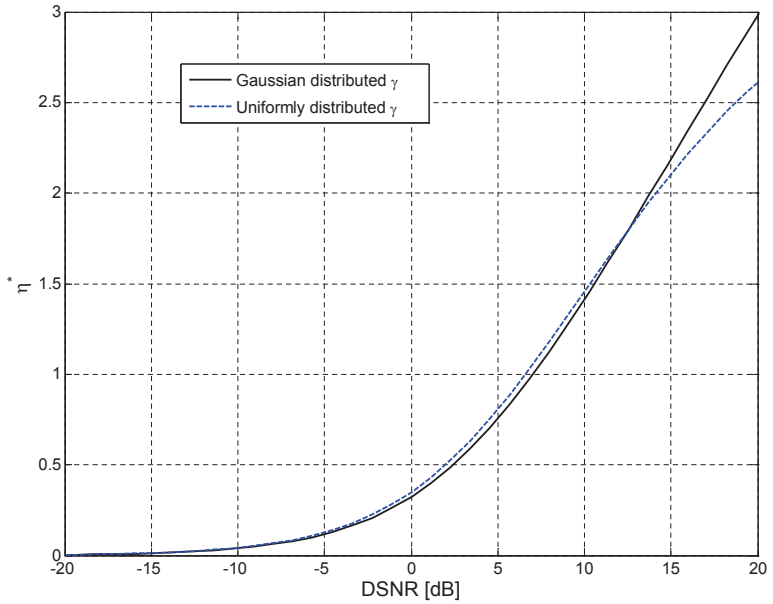

Figure 16: Optimal gain factor $\eta^\star$ as a function of DSNR for Example 1 and Example 2 with $\eta^\star > 0$.

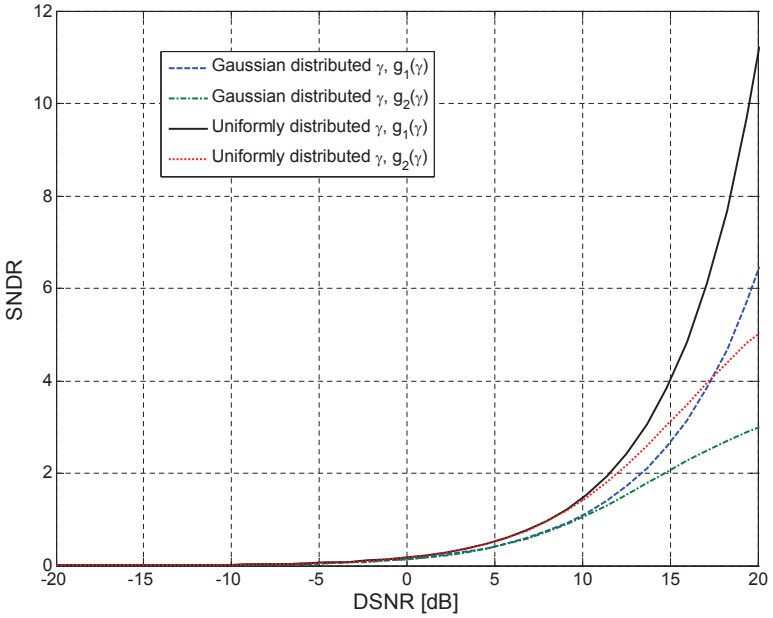

Figure 17: SNDR for uniformly and Gaussian distributed γ with different nonlinear mappings.

3.4 Relationship between SNDR and capacity

3.4.1 Lower bound on capacity

The capacity is given by

$$C = \max_{p_{x_\mathrm{o}}} I(y_\mathrm{o}; x_\mathrm{o}) = \max_{p_x} I(y; x) \tag{53}$$

where $I(y;x) = H(x) - H(x|y) = H(y) - H(y|x)$ is the mutual information between y and x [40]. To obtain the capacity of the dynamic-range-constrained channel, we need to solve the following optimization problem:

$$\max_{\substack{p_x, h(\cdot) \\ 0 \le h(\cdot) \le A}} \quad I(y;x) \tag{54}$$

for a specific zero-mean noise with variance σ_v^2. Moreover, (54) can be simplified as:

$$\max_{\substack{p_{x_\mathrm{s}} \\ 0 \le x_\mathrm{s} \le A}} \quad I(x_\mathrm{s} + v; x_\mathrm{s}) \tag{55}$$

which means that we need to find an input distribution in the interval $[0, A]$ to maximize the mutual information. Specially, when the noise v is Gaussian, the issue is similar to Smith's work in [39]. In this case, if DSNR is low, the capacity is achieved by an equal pair of mass points at 0 and A; if DSNR is high, the asymptotic capacity is the same as the information rate due to a uniformly distributed input in $[0, A]$ [39].

However, in most cases, we are most interested in the achievable data rate, given a nonlinear channel mapping with any input and any noise. Similar to the work in [34], we obtain a lower bound on the information rate:

$$
\begin{aligned}
& I(y;x) \\
\geq\ & H(x) - \frac{1}{2}\log(2\pi e\sigma_x^2) + \frac{1}{2}\log\left(\frac{\sigma_y^2}{\sigma_y^2 - \frac{\sigma_{xy}^2}{\sigma_x^2}}\right) \qquad (56) \\
=\ & H(x) - \frac{1}{2}\log(2\pi e\sigma_x^2) \\
+\ & \frac{1}{2}\log\left(\frac{\frac{A^2}{\sigma_v^2}\mathrm{var}[g(\gamma)] + 1}{\frac{A^2}{\sigma_v^2}\mathrm{var}[g(\gamma)] + 1 - \frac{A^2}{\sigma_v^2}E^2[\gamma g(\gamma)]}\right) \\
=\ & H(x) - \frac{1}{2}\log(2\pi e\sigma_x^2) + \frac{1}{2}\log(1+\mathrm{SNDR}) \qquad (57)
\end{aligned}
$$

by referring to (14). Since $C \geq I(y;x)$ for any input distribution p_x, by setting p_x to be the PDF of a zero-mean Gaussian r.v., we obtain

$$C \geq \frac{1}{2}\log(1+\mathrm{SNDR}) \qquad (58)$$

with the SNDR evalutated for a Gaussian x.

3.4.2 Upper bound on capacity

In this subsection, we find an upper bound for the capacity. Similar to [34], supposing p_y^* is the PDF of y that maximizes the capacity, i.e.,

$$p_y^* = \arg\max_{p_y}[H(y) - H(y|x)] \qquad (59)$$

we can write the capacity as

$$
\begin{aligned}
C = I(y;x)|_{p_y^*} &= H(y)|_{p_y^*} - H(y|x) \\
&= H(y)|_{p_y^*} - H(v). \qquad (60)
\end{aligned}
$$

Next, we bound the entropy $H(y)$ with the entropy of a Gaussian y, yielding

$$\begin{aligned} C &\leq \frac{1}{2}\log(2\pi e\sigma_y^2) - H(v) \\ &= \frac{1}{2}\log(2\pi e\sigma_y^2) - \frac{1}{2}\log(2\pi e\sigma_v^2) + \frac{1}{2}\log(2\pi e\sigma_v^2) - H(v) \\ &= \frac{1}{2}\log\left(1 + \frac{A^2\text{var}[g(\gamma)]}{\sigma_v^2}\right) + \frac{1}{2}\log(2\pi e\sigma_v^2) - H(v) \\ &\leq \frac{1}{2}\log\left(1 + \frac{A^2}{4\sigma_v^2}\right) + \frac{1}{2}\log(2\pi e\sigma_v^2) - H(v) \end{aligned} \tag{61}$$

where $\text{var}[g(\gamma)] \leq \frac{1}{4}$ with $g(\gamma) \in [0, 1]$. Specifically, if the noise is Gaussian, we have the upper bound:

$$C \leq \frac{1}{2}\log\left(1 + \frac{A^2}{4\sigma_v^2}\right). \tag{62}$$

Since $\varepsilon_d \geq 0$ and $\alpha^2\sigma_x^2 \leq \text{var}[h(\gamma)] \leq \frac{1}{4}A^2$, we must have

$$\text{SNDR} = \frac{\alpha^2\sigma_x^2}{\varepsilon_d + \sigma_v^2} \leq \frac{A^2}{4\sigma_v^2}. \tag{63}$$

Here, $\frac{A^2}{\sigma_v^2}$ is the defined DSNR, which is the same as that in [14].

3.4.3 Example of bounds

Since SNDR is determined by DSNR and the distribution of the signal, we plot the bounds as functions of DSNR for a Gaussian distributed signal, which is shown in Fig. 18. We also compare the lower bounds given by two different nonlinear mappings $g_1(\gamma)$ and $g_2(\gamma)$, which were introduced in the last section. This example illustrates that the nonlinearity $g_1(\gamma)$ chosen according to Theorem 1 yields a tighter lower bound as compared to the other nonlinearities. In addition, we can see that the capacity of a Gaussian channel, as determined by Smith [39], is between the lower and upper bounds that we have derived.

3.5 Conclusion

The main contribution of this chapter is the SNDR optimization within the family of dynamic-range-constrained memory-less nonlinearities. We showed that, under

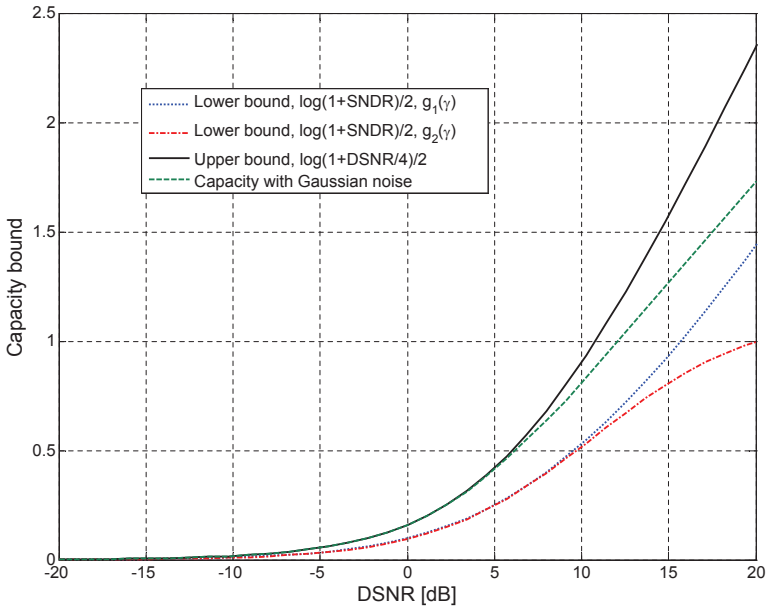

Figure 18: Bounds on capacity.

the dynamic-range constraint, the optimal nonlinear mapping that maximizes the SNDR is a double-sided limiter with a particular gain and a particular bias level, which are determined based on the distribution of the input signal and the DSNR. In addition, we found that $\frac{1}{2}\log(1+\text{SNDR})$ provides a lower bound on the nonlinear channel capacity, and $\frac{1}{2}\log(1+\frac{1}{4}\text{DSNR})$ serves as the upper bound. The results of this chapter can be applied for optimal linearization of nonlinear components and efficient transmission of signals with double-sided clipping.

CHAPTER IV

CONSTRAINED CLIPPING FOR PAPR REDUCTION IN VLC SYSTEMS WITH DIMMING CONTROL

As it is mentioned in Chapter 1 and Chapter 2, recently, OFDM has been considered for VLC to boost data rates and combat inter-symbol interference. However, VLC-OFDM inherits the disadvantage of high PAPR from traditional RF systems. Unlike RF signaling, both the maximum and minimum of VLC signals must be considered. Additionally, in order to support dimming control, the positive and negative dynamic-range constraints could be asymmetric. Clipping is the simplest way to satisfy the dynamic-range constraints, but it does not allow for any EVM distortion control. In this chapter, we use the constrained clipping method which can mitigate the distortions so that the clipping levels can be more aggressive than the simple clipping to further reduce the PAPRs. Numerical results validate the proposed constrained clipping technique.

4.1 Introduction

Recently, visible light communication (VLC) has attracted significant interest in both academia and industry due to the ever growing demand in wireless data and the massive deployment of light emitting diodes (LEDs) [1, 2]. Orthogonal frequency division multiplexing (OFDM) has been proposed for VLC due to its high spectral efficiency and ability to combat inter-symbol interference [19–23].

As mentioned in previous chapters, similar to OFDM in radio frequency (RF) systems, VLC-OFDM has a disadvantage of high peak-to-average power ratio (PAPR), which makes VLC-OFDM very sensitive to the operation range of LEDs and

causes serious degradation of optical power efficiency. Clipping is a simple and direct way to reduce the PAPRs without the modification of receivers. Unfortunately, to meet the system or channel requirements, the distortion should be constrained so that the clipping levels have to be above certain thresholds [9, 14, 21]. Thus, the PAPR performance of the simple clipping is limited.

To improve upon simple clipping and provide more control over the clipping distortion, we can add constraints in frequency-domain to the OFDM signal. By constraining how the distortion spreads amongst the subcarriers, we can control the bit error rate (BER) with more precision. This chapter outlines our proposal for a simple method to control clipping in VLC-OFDM systems.

There are two VLC-specific characteristics we would like to emphasize. First, signals in VLC systems are subject to double-sided clipping, which will be discussed in details in Section 4.2. In this case, we care about PAPRs on both the upper side and the lower side. Additionally, the LED acts as a low-pass filter, we do not need to consider the out-of-band interferences. This actually gives us additional degrees of freedom to develop PAPR reduction methods [54].

4.2 Double-sided clipping

VLC systems employ intensity modulation (IM) and direct detection (DD) so that the transmitted OFDM time-domain signals should be real-valued. In this case, Hermitian symmetry must be satisfied in the frequency-domain, i.e.,

$$X_k = X_{-k}^*, 1 \leq k \leq N/2 - 1, \tag{64}$$

where N is the size of inverse DFT (IDFT) and $*$ denotes complex conjugate. Since the subcarriers are independently modulated and then added up, according to central limit theorem, when N is large, the time-domain signals $x_n = \text{IDFT}(X_k)$ are approximately Gaussian distributed and can present high peaks [9,21]. The 0th and $-N/2$th

subcarriers contain no information and we set them to be null, i.e., $X_0 = X_{-N/2} = 0$. In our following discussions, the input OFDM signals are real-valued and zero mean.

In addition, the input OFDM signals cannot be transmitted by LEDs directly because VLC systems are dynamic-range-limited. To drive an LED, the input electric signal must be positive and exceed the turn-on voltage A_{min}. On the other hand, the signal is also constrained by the maximum permissible value or the saturation point of the LED, which is denoted by A_{max}. Thus, before transmitted through an LED, the original OFDM signal should be preprocessed to meet the requirement of the dynamic-range, which is shown in Fig. 19(a). A bias B can help convert the bipolar OFDM signal into the unipolar (positive) one. A reasonable gain G can guarantee that the dynamic-range of the LED can be fully utilized. Comparing two signals with the same variance, i.e., the same signal power, the one with lower peaks can be amplified by a larger gain so that a higher signal-to-noise power ratio (SNR) can be achieved. That is the reason why PAPR reduction is so important in OFDM systems.

Clipping is the simplest way to reduce the PAPR. Fig. 19(b) shows a basic example for clipping. Comparing Fig. 19(a) and Fig. 19(b), we see that the clipped signal can be amplified by a larger gain to achieve a higher transmitted signal power. However, clipping results in signal distortions. Hence, there is a tradeoff between the signal power and the clipping distortion, which was theoretically proved in [58].

Signals in VLC systems are subject to both turn-on clipping and saturation clipping, namely, double-sided clipping, due to the dynamic-range constraint, which is one of the most important differences from amplitude-limited RF systems. The clipped signal satisfies:

$$\bar{x}_n = \begin{cases} x_{max}, & x_n > x_{max}, \\ x_n, & x_{min} \leq x_n \leq x_{max}, \\ x_{min}, & x_n < x_{min}. \end{cases} \tag{65}$$

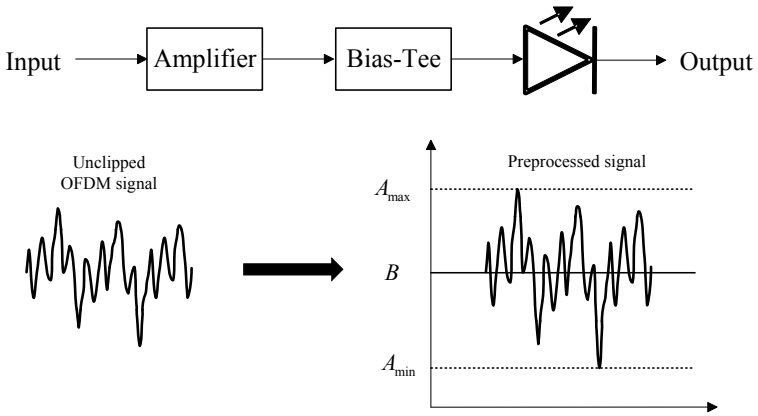

(a) Without clipping

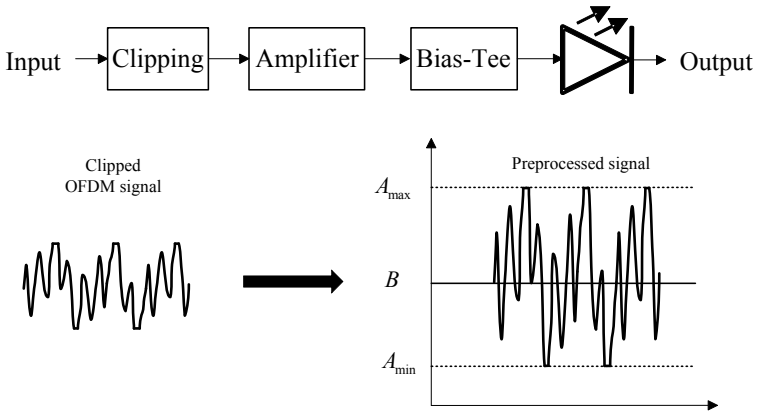

(b) With clipping

Figure 19: Illustration of preprocessing in VLC.

where $x_{max} = \frac{A_{max}-B}{G}$ and $x_{min} = \frac{A_{min}-B}{G}$. Thus, we care about both the upper (positive) PAPR and the lower (negative) PAPR of the input OFDM signal. According to [22, 23], we define the upper PAPR (UPAPR) of signal x_n as

$$\mathcal{U}(x_n) \triangleq \frac{\left(\max\limits_{0\le n\le N-1} x_n\right)^2}{\sigma_x^2} \tag{66}$$

and the lower PAPR (LPAPR) as

$$\mathcal{L}(x_n) \triangleq \frac{\left(\min\limits_{0\le n\le N-1} x_n\right)^2}{\sigma_x^2}, \tag{67}$$

where σ_x^2 is the signal power of input OFDM signal x_n.

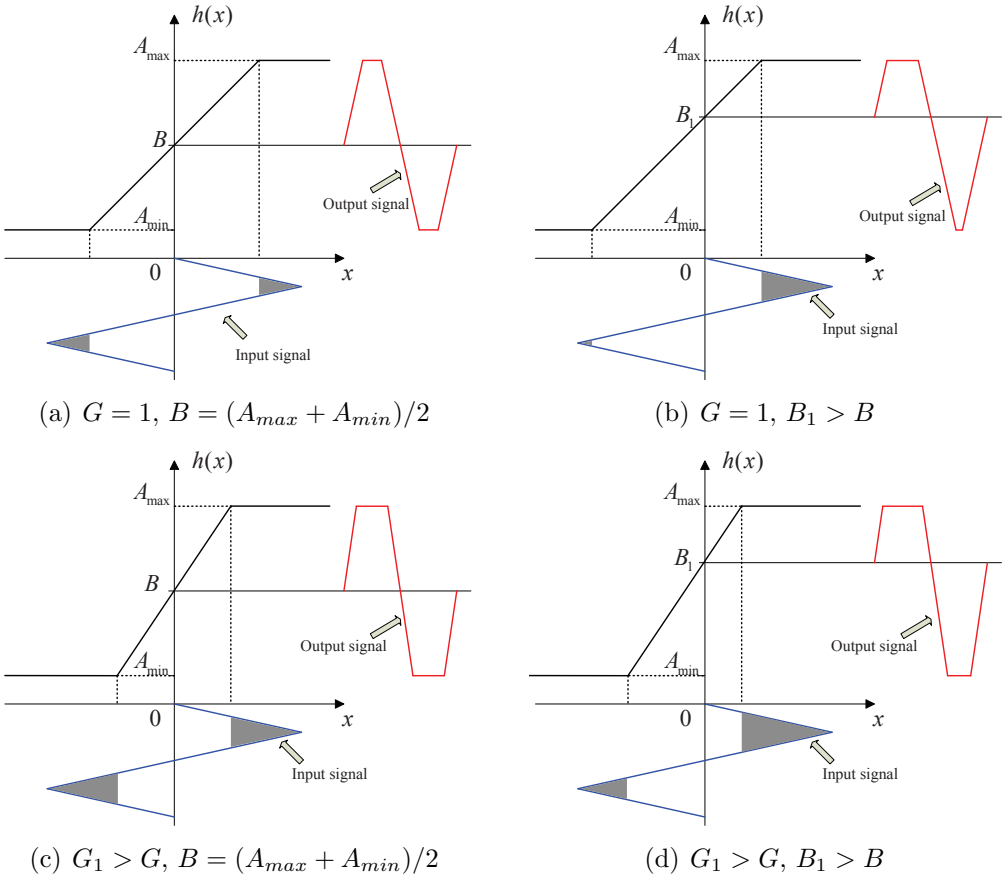

(a) $G = 1$, $B = (A_{max} + A_{min})/2$ (b) $G = 1$, $B_1 > B$

(c) $G_1 > G$, $B = (A_{max} + A_{min})/2$ (d) $G_1 > G$, $B_1 > B$

Figure 20: Some system mappings under the dynamic-range constraint.

The overall system mapping can be modeled as a double-sided limiter with a certain bias and a certain gain, which is shown in Fig. 20. The clipping ratios on both

sides are determined by the bias and the gain of the system mapping. For Gaussian distributed OFDM signals, the optimal bias to maximize signal-to-noise-plus-distortion ratio (SNDR) is the midpoint of the dynamic-range: $B = \frac{A_{max}+A_{min}}{2}$ [58]. In this case, signals are equally clipped on upper side and lower side, which is shown in Fig. 20(a). However, in practical VLC system, the biasing level is often determined by the illumination function. If the bias is a little larger (smaller) than the midpoint, more (less) signals on upper side will be clipped than lower side, which is shown in Fig. 20(b). Comparing Fig. 20(c) and 20(d) with Fig. 20(a) and 20(b), we see that a larger gain factor implies more clipping distortions.

For a fixed system mapping with a certain bias and a certain gain, one of the best ways to avoid too much clipping is to reduce PAPRs of the input OFDM signal on both upper and lower sides, which is a focus of this chapter. In addition, dimming control should be supported since the principal functionality of VLC systems is for lighting [2]. The required illumination level determines the bias point. We notice that the requirements for UPAPR and LPAPR can be different and this asymmetry is determined by the dynamic-range and the bias. We introduce asymmetric factor [56]:

$$\rho \triangleq \frac{(A_{max} - B)^2}{(A_{min} - B)^2}. \tag{68}$$

For example, if UPAPR is required to be less than 6 dB and the asymmetric factor is 1 dB, then the LPAPR should be less than 5 dB. In this case, we care about the joint complementary cumulative distribution function (CCDF) of UPAPR and LPAPR [23, 56]:

$$\begin{aligned} &\text{CCDF}\{\mathcal{U}(x_n), \mathcal{L}(x_n), \gamma, \rho\} \\ &\triangleq 1 - Pr\{\mathcal{U}(x_n) \leq \gamma, \mathcal{L}(x_n) \leq \gamma/\rho\}. \end{aligned} \tag{69}$$

4.3 Constrained clipping

Clipping in time-domain is the direct way to reduce PAPR, but results in distortion in frequency-domain. Error vector magnitude (EVM) is a commonly used metric to

quantify these distortions [14, 42, 43]. The error at the kth subcarrier is denoted by

$$E_k = \bar{X}_k - X_k, \tag{70}$$

where $\bar{X}_k = \mathrm{DFT}(\bar{x}_n)$. Then the EVM is calculated by

$$\mathrm{EVM} \triangleq \frac{1}{\sigma_X}\sqrt{\frac{1}{N}\sum_{k\in\mathcal{I}}|E_k|^2}, \tag{71}$$

where σ_X is the root mean square power of the original symbol X_k and $\mathcal{I}$ denotes the set of all the in-band subcarriers. The minimum requirement of EVM depends on the constellation type and system/channel conditions. According to 3GPP LTE specification, the EVM thresholds are 17.5% (QPSK), 12.5% (16-QAM), and 8.0% (64-QAM), respectively [42].

Too much clipping results in severe distortion. The clipping ratio can be presented by the normalized clipping levels on upper side and lower side:

$$\lambda_{upper} = \frac{x_{max}}{\sigma_x}, \tag{72}$$

$$\lambda_{lower} = -\frac{x_{min}}{\sigma_x}. \tag{73}$$

and we also have $\lambda_{upper} = \sqrt{\rho}\lambda_{lower}$.

To satisfy the EVM requirement, clipping levels cannot be very low. Thus, the traditional clipping method may be too conservative. If we can modify and mitigate the clipping distortions, clipping levels can be further lowered to reduce PAPR. In this chapter, we introduce the constrained clipping method, which was first proposed for RF systems [43]. However, there are two major differences between VLC systems and RF systems. We concern about the reduction for both UPAPR and LPAPR since VLC systems are dynamic-range-limited. Additionally, since LED acts as a low-pass filter, we do not need to consider the out-of-band emission [54].

The structure of the constrained clipping method is shown in Fig. 21. To begin with, the input signal x_n is simply clipped at preset clipping ratios λ_{upper} and λ_{lower}.

Then we transform the clipped signal $\bar{x}_n$ to the frequency-domain and try to mitigate the distortion. Thanks to Hermitian symmetry, we only need to deal with subcarriers indexed from 1 to $N/2-1$. We set $\hat{\mathcal{I}} = \{1, \cdots, N/2-1\}$.

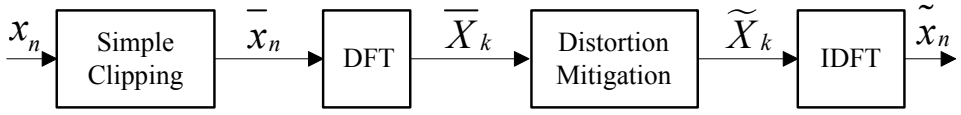

Figure 21: Block diagram of the constrained clipping method for VLC-OFDM.

The goal of distortion mitigation is to guarantee that the EVM satisfies the minimum requirement, which is denoted by Th. We first sort $|E_k|$ in ascending order and then find the largest subset $\mathcal{M}$ satifying

$$\frac{1}{\sigma_X}\sqrt{\frac{1}{|\mathcal{M}|}\sum_{k\in\mathcal{M}}|E_k|^2} \leq Th, \tag{74}$$

and we have $|E_p| \leq |E_q|, \forall p \in \mathcal{M}, q \in \hat{\mathcal{I}}\backslash\mathcal{M}$.

We keep subcarriers in $\mathcal{M}$ unchanged:

$$\tilde{X}_k = \bar{X}_k, \quad k \in \mathcal{M}. \tag{75}$$

However, for $\bar{X}_k, k \in \hat{\mathcal{I}}\backslash\mathcal{M}$, they violate the EVM constraint. Hence, we select $\tilde{X}_k$ so that

$$|\tilde{E}_k| = |\tilde{X}_k - X_k| = \sigma_X Th, \quad k \in \hat{\mathcal{I}}\backslash\mathcal{M}. \tag{76}$$

By using Hermitian symmetry and setting $\tilde{X}_0 = \tilde{X}_{-N/2} = 0$, we reconstruct all the in-band subcarriers. It can be easily proved that

$$\text{EVM}\{\tilde{x}_n\} \leq Th. \tag{77}$$

Next, we need to consider the PAPR of the revised signal. Modifying frequency-domain symbols will change the time-domain signals. Since the clipped signal $\bar{x}_n$ has low UPAPR and LPAPR, we hope to make the difference between $\tilde{x}_n$ and $\bar{x}_n$ as small

as possible so that the revised signal $\tilde{x}_n$ can also have low PAPRs. According to Parsevals Theorem

$$\sum_{n=0}^{N-1} |\tilde{x}_n - \bar{x}_n|^2 = \sum_{k \in \mathcal{I}} |\tilde{X}_k - \bar{X}_k|^2, \tag{78}$$

equivalently, we try to minimize $|\tilde{X}_k - \bar{X}_k|$. Considering (76), we select

$$\tilde{X}_k = X_k + Th \cdot \sigma_X e^{j\angle E_k}, \quad k \in \hat{\mathcal{I}} \backslash \mathcal{M}. \tag{79}$$

4.4 Numerical results

In this section, we would like to use simulations to evaluate the performance of the constrained clipping in VLC-OFDM system. Without loss of generality, we use a QPSK constellation, $N = 256$ and asymmetric factor $\rho = 1$ dB in all simulations.

One of the goals for the constrained clipping is to mitigate the distortion caused by clipping so that the EVM constraint can be satisfied. Fig. 22 shows the constellation maps of different clipping strategies. The clipping ratios are set as $\lambda_{upper} = 6$ dB and $\lambda_{lower} = 5$ dB. We see that the proposed constrained clipping method is robust to revise the OFDM symbols to meet the various EVM requirements.

Next, we evaluate the PAPR performance. Fig. 23 shows the joint CCDFs of UPAPR and LPAPR for various upper clipping levels and lower clipping levels. The EVM requirement is fixed to be 10%. The joint CCDF is calculated based on 50000 VLC-OFDM blocks. Comparing with the original OFDM signal, $3 \sim 4$ dB PAPR reduction can be achieved in most cases. Different clipping levels influence the PAPR performance. The original idea is to decrease the clipping levels so that we may further reduce the PAPR. However, if the clipping levels are too low, large positive/negative peak regrowths happen when modifying $\bar{x}_n$ to produce $\tilde{x}_n$. Thus, there is a tradeoff for the choice of clipping levels.

Fig. 24 shows an example of clipping level optimization for a specific PAPR requirement. We hope the UPAPR and LPAPR can be less than 9 dB and 8 dB respectively. Thus, we simulate the probability that an OFDM signal will exceed 9

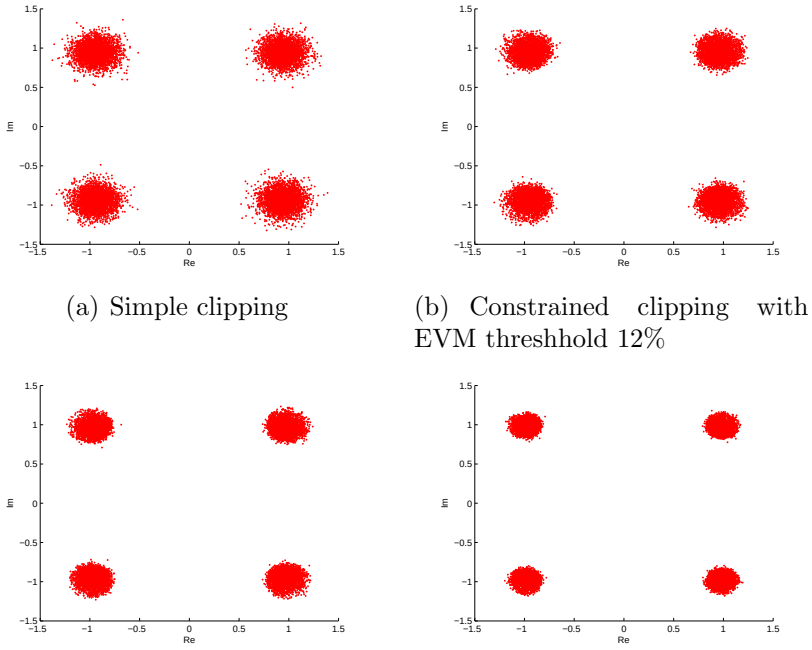

(a) Simple clipping

(b) Constrained clipping with EVM threshhold 12%

(c) Constrained clipping with EVM threshhold 10%

(d) Constrained clipping with EVM threshhold 8%

Figure 22: Constellations for different clipping strategies ($\lambda_{upper} = 6$ dB and $\lambda_{lower} = 5$ dB).

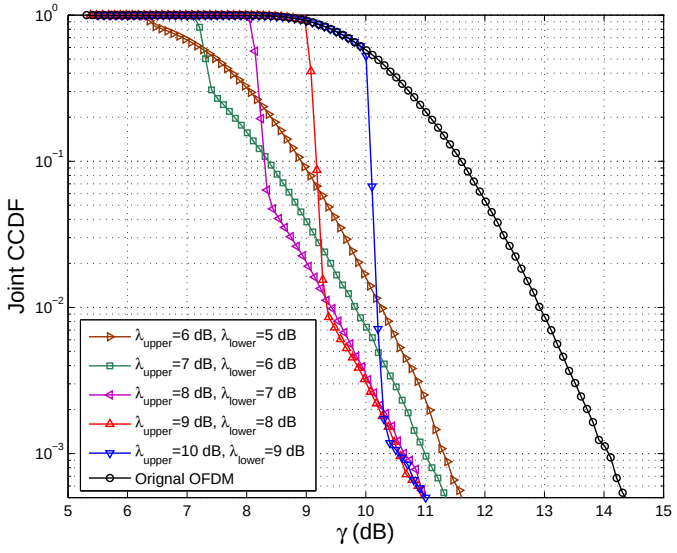

Figure 23: Performances of PAPR reduction with various upper clipping levels and lower clipping levels.

dB in UPAPR or 8 dB in LPAPR with various clipping levels. From the figure, we see that the optimal upper clipping ratio is 8.6 dB and the corresponding lower clipping ratio is 7.6 dB, when the PAPR outage probability is the smallest. In the practical systems, the parameter optimization can be done offline.

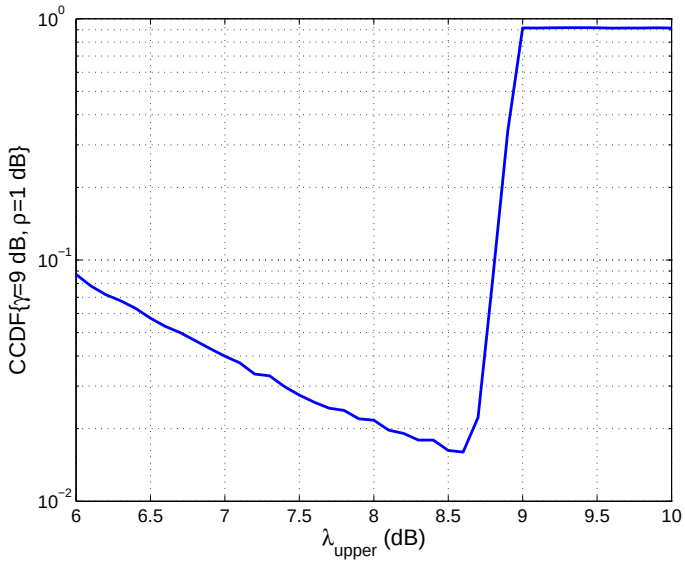

Figure 24: Probability that an OFDM signal will exceed 9 dB in UPAPR or 8 dB in LPAPR versus the upper clipping ratio λ_{upper} ($\rho = 1$ dB).

4.5 Conclusion

The objective of this chapter is to address the high PAPRs of the VLC-OFDM systems. We take into account both UPAPR and LPAPR since the VLC system has a dynamic-range constraint. Moreover, the requirements for UPAPR and LPAPR are always asymmetric, which is determined by the illumination level. Simple clipping on both sides is the direct way to reduce the PAPRs, but the performance is limited since the high clipping distortion should be avoided. In this chapter, we demonstrate a constrained clipping method, which can further clip the signal to achieve lower PAPRs and simultaneously mitigate the distortion to meet the EVM requirement. Simulation results show that the proposed method can obtain an impressive PAPR

reduction while maintaining the preset EVM threshold.

CHAPTER V

MIMO TRANSCEIVER DESIGN IN DYNAMIC-RANGE-LIMITED VLC SYSTEMS

Recently, multiple-input multiple-output (MIMO) has been proposed in visible light communications (VLC) systems to boost the data rate by utilizing spatial multiplexing. Unlike RF systems in VLC, lighting requirements, such as dimming control, should be taken into consideration for the design of a VLC transceiver. Moreover, VLC systems are inherently nonlinear and dynamic-range-limited. To drive an LED transmitter, the signal is bounded by a turn-on value and a saturation value. In this chapter, we show how the dynamic-range constraint and dimming control impact the design of MIMO transceiver. Three different MIMO schemes are proposed and studied by theoretical analysis and simulation.

5.1 Introduction

Recently, visible light communications (VLC) have received significant attention in both academia and industry. VLC can serve as a complementary solution to meet the growing demand in wireless data with the benefits of energy efficiency, safety and so on [1, 2]. However, the low modulation bandwidth of the light emitting diode (LED) transmitter limits the data rates of VLC systems. Thus, optical multiple-input multiple-output (MIMO) has been proposed to achieve high-rate transmission by utilizing spatial multiplexing to obtain parallel data streams [44–53].

Since VLC uses the intensity modulation and direct detection (IM/DD), the channel correlation is a bottleneck for optical MIMO. Currently, some methods have been studied for VLC MIMO channel decorrelation, such as cross links blocking (opaque

boundaries or narrow field-of-view) [44], power imbalance [45], artificial neural network (ANN) equalizer [46], angle adjusting [47], and imaging receiver [48, 49].

Besides the channel decorrelation, MIMO transceiver design is another important issue, which has been widely investigated. For instance, the simplest way is to apply the inversion or pseudo-inversion of the channel matrix at the receiver side [46–50], which may result in noise amplification [51]. Another way is to borrow traditional schemes from RF systems, such as singular value decomposition (SVD) scheme [45,52]. These current studies for optical MIMO only consider the nonnegativity of VLC transmission. However, VLC systems are dynamic-range-limited. To drive an LED, the input electric signal must be positive and exceed a turn-on voltage and not surpass the saturation point or maximum permissible value of the LED [13, 54, 55]. Moreover, dimming control places extra limitations on VLC system design since the primary function of LEDs is for lighting. Therefore, optical MIMO transceivers should be further enhanced to capture these features.

In this chapter, under VLC-specific constraints, both traditional SVD scheme and minimum mean-square error (MMSE) scheme are discussed. Additionally, maximum likelihood (ML) detection and equalization-based detection are compared. We demonstrate the impact of dimming control and dynamic-range constraints on the design of MIMO transceiver. Moreover, our analysis and simulation show that the SVD-based transceiver is not suitable to a dynamic-range-limited system. Our proposed MMSE scheme can be a practical solution to achieve high performance under the VLC-specific constraints.

Notation: For convenience, we summarize the mathematical notations here. In this chapter, uppercase and lowercase letters denote matrices and vectors, respectively; operator $(\cdot)^T$, $(\cdot)^H$, $(\cdot)^{-1}$ denote the transpose, conjugate transpose and inverse of a matrix/vector, respectively; $\mathbf{I}_N$ is an $N \times N$ identity matrix; $\mathbb{E}\{\cdot\}$ denotes

the statistical expectation; $Tr(\cdot)$ is the trace of a matrix; $\| \cdot \|$ denotes the Frobenius norm; min$(\cdot)$ denotes an element-wise minimum operator; and abs$(\cdot)$ denotes an element-wise absolute operator.

5.2 System model

Fig. 25 shows the MIMO VLC system with N_t LEDs in the transmitter and N_r photo detectors (PDs) in the receiver. The MIMO channel is modeled as an $N_r \times N_t$ matrix, whose element h_{mn} indicates the channel gain between the nth LED and the mth PD. Here, we assume that the channel response in each transmission period is flat.

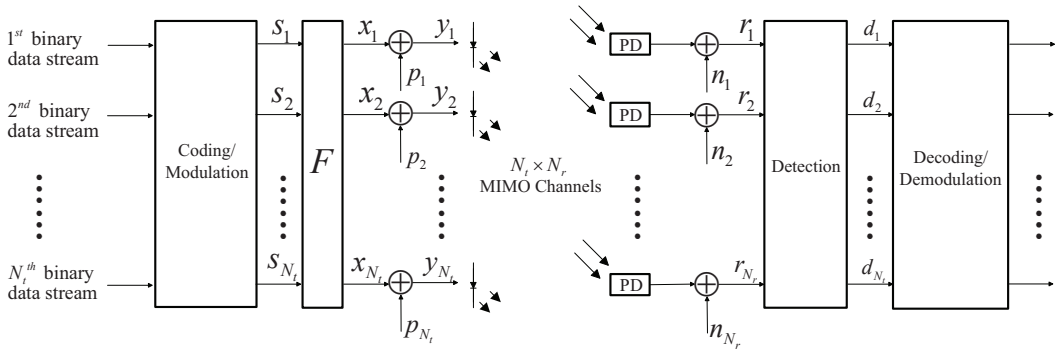

Figure 25: MIMO VLC system.

5.2.1 Transmitter side

N_t binary data streams are coded/modulated into source data vector $\mathbf{s}(\tau) = [s_1(\tau), \cdots, s_{N_t}(\tau)]^T$. For convenience, we omit the time index τ in the rest of the chapter. The source data s_k is assumed to be zero-mean and bounded as

$$-b_k \leq s_k \leq b_k. \tag{80}$$

The multi-level pulse amplitude modulation (PAM) and orthogonal frequency division multiplexing (OFDM) can be practical examples. The pulse position/width modulation (PPM/PWM) is not considered here, because different pulse positions and various pulse widths (caused by dimming control) from different LEDs make

MIMO detection more complicated than the case of PAM. Since the VLC employs intensity modulation and direct detection, the signals must be real-valued. Thus, all vectors/matrices are real-valued in this chapter.

The source data streams can not drive the LEDs directly. To support dimming control and satisfy the dynamic-range constraints of LEDs, the source data vector will be multiplied by a $N_t \times N_t$ precoder matrix $\mathbf{F}$ and then added by the DC biasing vector $\mathbf{p} = [p_1, \cdots, p_{N_t}]^T$, which is shown in Fig. 25. Such a MIMO VLC transmitter structure was firstly introduced in our previous work [53], but only the nonnegativity of the LED transmission signals was considered.

The transmitted signal can be presented by

$$\mathbf{y} = \mathbf{F}\mathbf{s} + \mathbf{p} \tag{81}$$

where we assume that the LED electrical-to-optical conversion is linearized by some methods [54] and the overall gain is chosen as 1 for convenience without loss of generality. In other words, we mainly study how to avoid double-sided clipping distortion in this chapter. We can calculate the optical power of each LED:

$$\mathbb{E}\{y_i\} = \sum_{k=1}^{N_t} f_{i,k}\mathbb{E}\{s_k\} + p_i = p_i \tag{82}$$

where $f_{i,k}$ is the element of the precoder matrix $\mathbf{F}$. Then dimming control can be supported by adjusting the DC bias.

As we mentioned before, the LED is a dynamic-range-limited device which is bounded by a turn-on value and a saturation value. Thus, for each LED, we should have

$$0 < l_i \leq y_i = \sum_{k=1}^{N_t} s_k f_{i,k} + p_i \leq u_i \tag{83}$$

where $[l_i, u_i]$ is the dynamic-range constraint of the ith LED.

According to (80), the signal after precoder satisfies

$$-\sum_{k=1}^{N_t} b_k |f_{i,k}| \leq \sum_{k=1}^{N_t} s_k f_{i,k} \leq \sum_{k=1}^{N_t} b_k |f_{i,k}|. \tag{84}$$

Comparing (83) and (84), we need

$$\sum_{k=1}^{N_t} b_k |f_{i,k}| \leq p_i - l_i, \tag{85}$$

$$\sum_{k=1}^{N_t} b_k |f_{i,k}| \leq u_i - p_i \tag{86}$$

to avoid the violation of the dynamic-range, i.e., double-sided clipping distortion. We can rewrite (85) and (86) as

$$\text{abs}(\mathbf{F})\mathbf{b} \leq \min\{\mathbf{p} - \mathbf{l}, \mathbf{u} - \mathbf{p}\}, \tag{87}$$

where $\mathbf{l} = [l_1, \cdots, l_{N_t}]^T$ and $\mathbf{u} = [u_1, \cdots, u_{N_t}]^T$. Since the DC bias vector is determined by the illumination level, our goal is to design a high-performance precoder under the constraint (87).

5.2.2 Receiver side

At receiver, N_r PDs are used to convert the optical signals to electric signals. The received signals can be presented by

$$\mathbf{r} = \mathbf{H}\mathbf{y} + \mathbf{n} = \mathbf{H}\mathbf{F}\mathbf{s} + \mathbf{H}\mathbf{p} + \mathbf{n}, \tag{88}$$

where $\mathbf{n}$ is the additive white Gaussian noise with zero mean and independent of the data vector. Considering the path loss of the optical links, the received signal is small while the dynamic-range that the receiver can handle is relatively large [54]. Thus, only the dynamic-range constraint at the transmitter is considered.

After removing DC components, there are several detection techniques to estimate the source data. As it is well known, maximum likelihood (ML) detection is optimal in the sense of minimizing the error probability. In our system, the ML detector can be presented by

$$\hat{\mathbf{s}} = \arg\min_{\mathbf{s}\in\mathbb{S}} \left\| \mathbf{r} - \mathbf{H}\mathbf{p} - \mathbf{H}\mathbf{F}\mathbf{s} \right\|^2 \tag{89}$$

where $\mathbb{S}$ is the set of all possible source data vectors. For $M-$ary PAM, the complexity order of the ML detection is $O(M^{N_t})$.

Equalization-based detection is another popular technique in MIMO systems. The received signal will be multiplied by an equalization matrix $\mathbf{G}$. The detected data vector is

$$\hat{\mathbf{s}} = Q\{\mathbf{Gr} - \mathbf{GHp}\} \tag{90}$$

where $Q\{\cdot\}$ is element-wise quantization according to the data alphabet. The complexity order of the equalization-based detection is $O(N_t)$, which is much less complex than that of the ML detection.

5.3 Transceiver design

In this section, we focus on designing the MIMO transceiver with the knowledge of the channel state information. Specifically, given the channel matrix $\mathbf{H}$, our goal is to determine the precoder matrix $\mathbf{F}$ or the equalization matrix $\mathbf{G}$.

5.3.1 Revised SVD-based transceiver

SVD-based transceiver is widely used in RF MIMO systems, since it can generate independent parallel links. Different from RF systems, dynamic-range constraints should be taken into account to design VLC transceiver. The SVD of the channel matrix is given by

$$\mathbf{H} = \mathbf{U}\mathbf{\Lambda}\mathbf{V}^T \tag{91}$$

where $\mathbf{U} \in \mathbb{R}^{N_r \times N_t}$, $\mathbf{V} \in \mathbb{R}^{N_t \times N_t}$ and $\mathbf{\Lambda}$ is an $N_t \times N_t$ diagonal matrix whose diagonal elements are the singular values of the channel matrix $\mathbf{H}$ [52].

We can set $\mathbf{F} = \alpha\mathbf{V}$, where α is the gain factor to control the transmitted signal power. To satisfy the dynamic-range constraint and maintain a high transmission

power, we can select the gain factor as

$$\begin{aligned} &\max \quad \alpha, \\ &s.t. \quad \text{abs}(\alpha \mathbf{V})\mathbf{b} \leq \min\{\mathbf{p}-\mathbf{l}, \mathbf{u}-\mathbf{p}\}. \end{aligned} \tag{92}$$

The equalization matrix is chosen as $\mathbf{G} = \mathbf{U}^T$.

5.3.2 Iterative MMSE transceiver

We can jointly design the precoder and equalizer to minimize the mean-square error (MSE)

$$\begin{aligned} &MSE(\mathbf{r}, \mathbf{s}, \mathbf{F}, \mathbf{G}) \\ &= \mathbb{E}\{\left\| \mathbf{Gr} - \mathbf{GHp} - \mathbf{s} \right\|^2\} \\ &= Tr(\mathbf{GHFR_s}(\mathbf{GHF})^H) + Tr(\mathbf{GR_nG}^H) \\ &+ Tr(\mathbf{R_s}) - Tr(\mathbf{GHFR_s}) - Tr(\mathbf{R_s}(\mathbf{GHF})^H) \end{aligned} \tag{93}$$

where $\mathbf{R_n} = \mathbb{E}\{\mathbf{nn}^H\}$ and $\mathbf{R_s} = \mathbb{E}\{\mathbf{ss}^H\}$. The MSE optimization problem is not convex in terms of $\mathbf{G}$ and $\mathbf{F}$, so that the solution cannot be found directly.

Similar to [53], we can also use an iterative scheme to figure out the optimal $\mathbf{F}$ and $\mathbf{G}$. Here the "optimal" means $\mathbf{F}$ (or $\mathbf{G}$) can be solved optimally when fixing $\mathbf{G}$ (or $\mathbf{F}$).

Given $\mathbf{F}$, by setting $\partial MSE(\mathbf{r}, \mathbf{s}, \mathbf{F}, \mathbf{G})/\partial \mathbf{G} = 0$, we have the MMSE equalizer:

$$\mathbf{G} = \mathbf{R_s}(\mathbf{HF})^H(\mathbf{HFR_s}(\mathbf{HF})^H + \mathbf{R_n})^{-1}. \tag{94}$$

When fixing $\mathbf{G}$, the objective is quadratic in terms of f_{ij} and the feasible set given by (87) is convex. Thus, we can solve this optimization problem by CVX, a software package for convex programs [57].

We can calculate $\mathbf{F}$ or $\mathbf{G}$ iteratively by fixing one of them to update the other. During each iteration, the MSE is decreased and bounded by zero, so that the algorithm is converged. It cannot be guaranteed that the final solution is global optimal

but the performance should still be attractive.

5.4 Numerical results and discussions

In the simulation, we consider a 4×4 MIMO VLC system. As examples, we select two channel matrices measured in [47]:

$$\mathbf{H}_1 = 10^{-6} \begin{bmatrix} 0 & 0.2083 & 0.6285 & 0.2083 \\ 0.2083 & 0 & 0.2083 & 0.6285 \\ 0.6285 & 0.2083 & 0 & 0.2083 \\ 0.2083 & 0.6285 & 0.2083 & 0 \end{bmatrix}, \tag{95}$$

$$\mathbf{H}_2 = 10^{-6} \begin{bmatrix} 0.4961 & 0.4936 & 0.4906 & 0.4931 \\ 0.1995 & 0.6526 & 0.4115 & 0.0529 \\ 0 & 0.0879 & 0.5623 & 0.2001 \\ 0.0075 & 0 & 0.0538 & 0.4057 \end{bmatrix}. \tag{96}$$

The singular values of both matrices are calculated as $\mathbf{sv}_1 = 10^{-5} \times [0.1045\ 0.0629\ 0.0628\ 0.0212]$ and $\mathbf{sv}_2 = 10^{-5} \times [0.1309\ 0.0498\ 0.0389\ 0.0173]$. Thus, the condition number of $\mathbf{H}_2$ is larger than that of $\mathbf{H}_1$, which means $\mathbf{H}_2$ is more ill-conditioned than $\mathbf{H}_1$.

The dynamic-ranges of LEDs are selected as $\mathbf{l} = [1, 1, 1, 1]^T$ and $\mathbf{u} = [9, 9, 9, 9]^T$. We assume the signals and the noises are i.i.d., then we have $\mathbf{R_s} = \sigma_s^2 \mathbf{I}_4$ and $\mathbf{R_n} = \sigma_n^2 \mathbf{I}_4$. Since the precoder will adaptively adjust the transmitted signal power, here we just set $\sigma_s^2 = 1$. Additionally, 2-PAM is used, thus, the source data symbol is generated from 1 and -1. The actual electrical power is determined by both the dynamic-range and the DC bias. If the dynamic-range of the LED is fully utilized, the maximum electrical power of an LED can be 42 dBm. From the selected channel matrices, we can see that the path loss is around 120 dB, which is common in practical

VLC scenarios. For the SNR consideration, the noise power σ_n^2 is selected from the range $[-98, -80]$ dBm.

Three different MIMO schemes are compared in our simulations. The first scheme uses the MMSE precoder and the MMSE equalizer derived from the iterative algorithm in Section 5.3.2. In the second scheme, the same MMSE precoder is applied but the equalization-based detection is replaced by ML detection. The third scheme is the revised SVD-based transceiver described in Section 5.3.1.

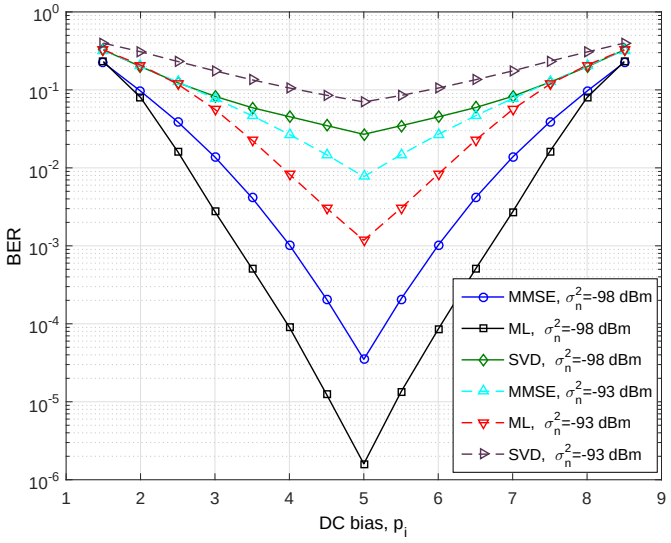

Figure 26: BER performance of the different transceivers with various illumination levels (for the case of $\mathbf{H}_1$).

To begin with, we take into account the impact of dimming control and the bit error rate (BER) is simulated as the metric to evaluate the performance. We adjust the DC bias of each LED simultaneously from 1 to 9. The simulation result for the case of $\mathbf{H}_1$ is shown in Fig. 26. The BER curves of three different schemes are marked by "MMSE", "ML" and "SVD", respectively. From Fig. 26, we can see that the BER performance is the best when the DC bias is chosen as 5, which is the midpoint of the dynamic-range. Such phenomenon also matches with the single-input single-output (SISO) scenario [55, 58]. When the illumination level is low, the lower peaks of the

signals are constrained by the turn-on values of LEDs. When the DC bias is high, the upper peaks of the signals are limited by the saturation values of LEDs. Only if the DC bias is right in the middle can the dynamic-ranges of LEDs be fully exploited, which equivalently means a high electrical SNR can be achieved. We can draw the same conclusion for $\mathbf{H}_2$, so the plot is omitted here.

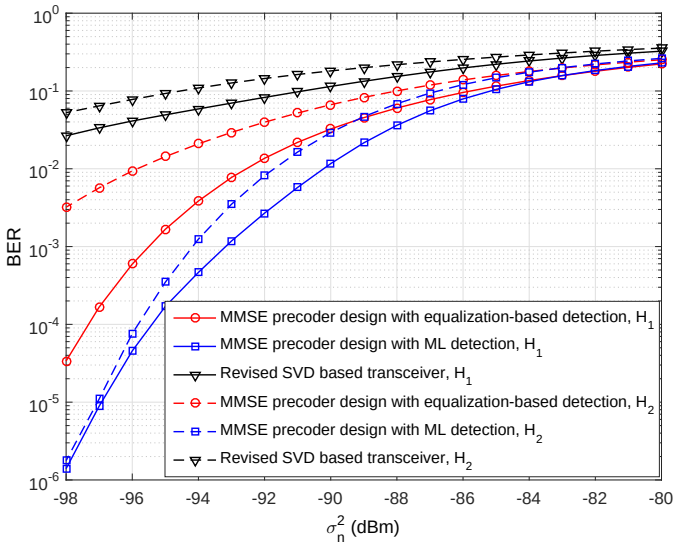

Figure 27: BER of the different transceivers with various noise levels.

We also simulate the BER performance of the different transceivers with various noise levels for both two channel realizations, which is shown in Fig. 27. The DC bias is fixed as 5. From both Fig. 26 and Fig. 27, we see that the ML detection is better than the equalization-based detection. However, the complexity of the ML detection is much higher than that of the equalization-based detection that we analyzed in Section 5.2.2. In addition, the SVD-based transceiver is not suitable to the dynamic-range-limited VLC system. The dynamic-range of the LED cannot be utilized adequately because the SVD-based transceiver should not violate the dynamic-range constraint while maintaining orthogonality. On the other hand, the BER gap between equalization-based detection and ML detection for $\mathbf{H}_2$ is larger than that for $\mathbf{H}_1$, which means equalization-based detection is more sensitive to the

channel correlation than ML detection.

Although the iterative MMSE transceiver is a little computationally expensive, it is still acceptable because the indoor VLC system is static in most cases. The channel matrix does not change frequently. The precoder matrix and equalizer matrix obtained by our iterative scheme can be adopted for a long time.

5.5 Conclusion

In this chapter, we studied a MIMO VLC system with dimming control. In contrast to RF systems, VLC systems are dynamic-range-limited. To avoid double-sided clipping distortion, the transmitter should guarantee that the signal is above the turn-on value and below the saturation value of the LED. Under these VLC-specific requirements, we discussed three MIMO schemes: MMSE precoder with MMSE equalizer, MMSE precoder with ML detection, and SVD-based transceiver. From our analysis and simulation, we conclude that the BER performance is not very good when the illumination level requires the DC bias close to the lower bound or upper bound of the dynamic-range. When the DC bias is in the middle, the BER performance is the best because the dynamic-range of the LED is fully utilized. In addition, we observe that the traditional SVD-based transceiver is not suitable for dynamic-range-limited systems because it can not exploit the dynamic-range of LEDs adequately. ML detection is better than equalization-based detection at the expense of additional complexity. Since the indoor VLC scenario is static, the proposed iterative MMSE transceiver design can be a practical solution to achieve high performance under the constraints of dimming control and dynamic-range limitation.

CHAPTER VI

CONSTRAINED CLIPPING FOR PAPR REDUCTION IN BIT-LOADED VLC-OFDM SYSTEMS WITH DIMMING CONTROL

As mentioned in previous chapters, recently, bit-loaded OFDM has been proposed in VLC systems to boost the data rate and combat the frequency-selectivity caused by the low-pass nature of LEDs. However, the high PAPR introduced by OFDM makes the signal sensitive to the dynamic-range-limited nonlinearity of the LED and decreases the power efficiency. In this chapter, we consider a distortion-based PAPR reduction method based on simple clipping, which is called constellation-wise constrained clipping. Comparing to simple clipping, the proposed constrained clipping can further reduce PAPR with lower clipping levels and revise the introduced clipping distortions to meet the various EVM requirements of different in-band subcarriers. Simulation results validate the performance of the proposed scheme.

6.1 Introduction

In recent years, with the wide deployment of light emitting diodes (LEDs) and the ever growing demand in wireless data, visible light communication (VLC) has been proposed as a complementary solution in both academia and industry [1, 2]. In addition, orthogonal frequency division multiplexing (OFDM) is considered for VLC due to its ability to combat inter-symbol interference (ISI) and to boost the data rate [19–23]. Another benefit from OFDM is that bit-loading among the subcarriers can help fully exploit the available modulation bandwidth, since the LED response exhibits frequency-selectivity [56].

Unfortunately, optical OFDM inherits the disadvantage of high peak-to-average power ratio (PAPR) [9, 14, 19–23, 56], which degrades the optical power efficiency and makes VLC-OFDM very sensitive to the dynamic-range of LEDs. Thus, PAPR reduction is also an important issue in VLC-OFDM system design.

There are two major categories of methods for PAPR reduction. One is side-information-based. At the transmitter side, the signal is modified into the one with lower PAPR according to some rules such as companding [19], selective mapping [22, 26], and coding [21, 27]. Then the original signal can be recovered at the receiver side with the provided rules. In this case, side information should be provided and receiver side modifications are required.

The other method is distortion-based. This method distorts OFDM signals when reducing the PAPR and the distorted signal may not be recovered to the original one at the receiver side. The benefit is that receiver side modifications are avoided, so that distortion-based method is more practical. For example, clipping is the simplest distortion-based method [14, 21].

However, there are two limitations of simple clipping. Firstly, the clipping distortions should be constrained to meet the system/channel requirements, so that the clipping levels have to be above certain thresholds [14, 21]. Secondly, the clipping distortions are equally distributed among all the subcarriers [56]. Thus, in bit-loaded OFDM systems, the subcarriers with highest modulation order limit the selection of the clipping level. Since more distortions can be allowed into subcarriers with lower modulation orders, such a constellation-agnostic method is too conservative.

In this chapter, to improve upon simple clipping with more control over the clipping distortion, we add constellation-wise constraints in the frequency-domain to the OFDM signal. Different from our preliminary work in Chapter 4, by constraining how the distortion spreads amongst the different subcarriers with various modulation orders, we can control the bit error rate (BER) with more precision. The introduced

complexity is relatively low and receiver side modifications are not needed, so that the proposed constellation-wise constrained clipping method can be a practical solution to reduce PAPR in VLC-OFDM systems.

Moreover, three VLC-specific characteristics are considered into the technique design. First of all, the VLC signal is real-valued and dynamic-range-limited due to the intensity modulation of LEDs. Unlike amplitude-limited system such as radio frequency (RF) systems, we care about PAPRs on both the lower side and the upper side in VLC systems [22, 23]. Secondly, dimming control is supported to meet the lighting requirement. DC bias adjustment is considered here so that upper clipping and lower clipping can be asymmetric and changeable. Thirdly, LEDs act as low-pass filters and there is no out-of-band application [54]. Thus, we omit oversampling and corresponding processing/analysis of out-of-band-emission here.

6.2 Bit-loaded VLC-OFDM systems

Same as we discuss in Chapter 4, the transmitted OFDM time-domain signals should be real-valued, which requires Hermitian symmetry in the frequency-domain, i.e., $X_k = X_{-k}^*, 1 \leq k \leq N/2-1$, where $*$ denotes complex conjugate and N is the number of in-band subcarriers. The 0th and $-N/2$th subcarriers do not contain any information and we set them as $X_0 = X_{-N/2} = 0$. In this chapter, we also use $\mathcal{I}$ to denote the set of all the in-band subcarriers. However, in most cases, we only deal with subcarriers containing primary information, so we also set $\hat{\mathcal{I}} = \{1, \cdots, N/2-1\}$.

According to the tests of some commercial LEDs [29], it is well known that the 3-dB bandwidth of LEDs is only a few MHz. In other words, LEDs act as low-pass filters and exhibits frequency-selectivity. Instead of using pre-equalization or power loading, in this chapter, we would like to apply bit-loading among different subcarriers, so that the available modulation bandwidth of LEDs, which can be larger than the 3-dB bandwidth, will be fully exploited. Fig. 28 serves as an example. According to the

LED frequency response, for the low-frequency subcarriers, which have the strongest response, high-order constellation types like 64-QAM can be used to load more bits. For the high-frequency subcarriers, which may be beyond the 3-dB bandwidth, we just apply QPSK. Thus, the in-band subcarriers can be further divided into some subgroups and each subgroup adopts a kind of constellation type:

$$\mathcal{I} = \bigcup_{1 \le i \le V} \mathcal{I}_i \quad \text{or} \quad \hat{\mathcal{I}} = \bigcup_{1 \le i \le V} \hat{\mathcal{I}}_i \tag{97}$$

where V is number of constellation types used by in-band subcarriers.

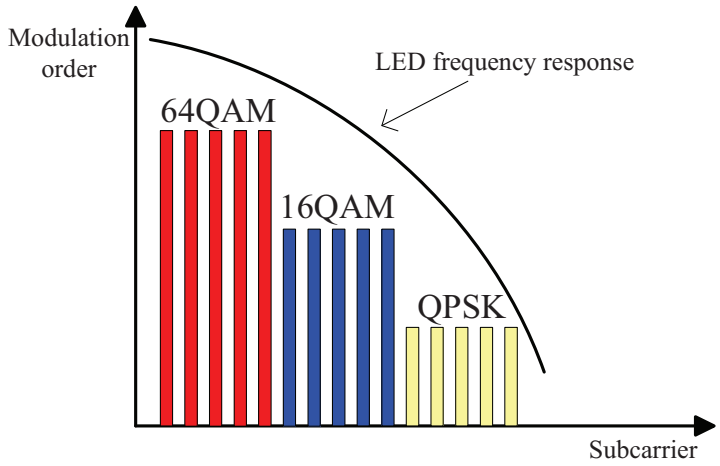

Figure 28: An example of bit-loading in VLC-OFDM systems.

6.3 Double-sided PAPR considerations

In OFDM systems, subcarriers are independently modulated and then added up. As a result, the time-domain signals are approximately Gaussian distributed according to central limit theorem, and can present high peaks [9, 21]. In other words, VLC-OFDM inherits the disadvantage of high PAPR. However, due to the VLC-specific requirements, there are some special considerations on the VLC-OFDM signal and its PAPR issue.

To begin with, thanks to Hermitian symmetry, real-valued signals can be produced

for intensity modulation:

$$x_n = \frac{2}{\sqrt{N}} \sum_{k=1}^{N/2-1} \left(Re(X_k) \cos\left(\frac{2\pi kn}{N}\right) - Im(X_k) \sin\left(\frac{2\pi kn}{N}\right) \right), 0 \leq n \leq N-1 \tag{98}$$

where $Re(\cdot)$ denotes the real part value and $Im(\cdot)$ denotes the imaginary part value. Since $X_0 = X_{-N/2} = 0$, the unprocessed time-domain signal x_n is zero-mean.

In addition to the real-value requirement, dynamic-range constraint is another VLC-specific limitation. To drive the LED, the electric signal must exceed a positive turn-on voltage A_{min} and should be less than the maximum permissible value or the saturation point of the LED, which is denoted by A_{max}. Thus, a bias B and an amplifier gain G are applied to x_n so that the dynamic-range of the LED can be fully utilized:

$$A_{min} \leq Gx_n + B \leq A_{max}. \tag{99}$$

Here, we assume that the LED electrical-to-optical conversion within the dynamic-range is pre-distorted by some techniques [54], which means only clipping distortions for signals beyond the dynamic-range is considered.

Generally speaking, the bias B converts the bipolar OFDM signal to be positive and guarantees that most of the signal can be within the dynamic-range. There is an optimal bias, which has been theoretically proved in [58]. But, in VLC systems, it is determined by the illumination requirement due to the dimming control. The bias does not contain any information and will be removed at the receiver side.

The amplifier gain G is used to control the electrical signal power. A large amplifier gain enables signals with high power. However, there is a tradeoff since the amplified signal will break out the dynamic-range. Intuitively, with the same average power, the signal with higher peak should work with a lower gain to avoid the violation of the dynamic-range constraint. That is the reason why PAPR reduction is so important.

Different from amplitude-limited systems, we care about both the upper PAPR (positive peak) and the lower PAPR (negative peak) of the input VLC-OFDM signal. Since we have discussed the special characteristics of double-sided PAPR considerations for VLC in Chapter 4, here we just recall the definitions of upper PAPR (UPAPR), lower PAPR (LPAPR), asymmetric factor ρ and joint CCDF of UPAPR and LPAPR for signal x_n:

$$\mathcal{U}(x_n) \triangleq \frac{\left(\max\limits_{0\leq n\leq N-1} x_n\right)^2}{\sigma_x^2}, \tag{100}$$

$$\mathcal{L}(x_n) \triangleq \frac{\left(\min\limits_{0\leq n\leq N-1} x_n\right)^2}{\sigma_x^2}, \tag{101}$$

$$\rho \triangleq \frac{(A_{max}-B)^2}{(A_{min}-B)^2}, \tag{102}$$

and

$$\begin{aligned} &\mathrm{CCDF}\{\mathcal{U}(x_n), \mathcal{L}(x_n), \gamma, \rho\} \\ &\triangleq 1 - Pr\{\mathcal{U}(x_n) \leq \gamma, \mathcal{L}(x_n) \leq \gamma/\rho\}, \end{aligned} \tag{103}$$

where σ_x^2 is the electrical signal power (variance) of input OFDM signal x_n.

6.4 Constellation-wise constrained clipping

In this chapter, we discuss a distortion-based PAPR reduction method based on clipping.

6.4.1 Simple clipping in time-domain

Clipping in time-domain is the simplest way to reduce the PAPR. As we mentioned in Chapter 4, the clipped signal satisfies:

$$\bar{x}_n = \begin{cases} x_{max}, & x_n > x_{max}, \\ x_n, & x_{min} \leq x_n \leq x_{max}, \\ x_{min}, & x_n < x_{min}. \end{cases} \tag{104}$$

where $x_{max} = \frac{A_{max}-B}{G}$ and $x_{min} = \frac{A_{min}-B}{G}$. The absolute values of the clipping levels are inversely proportional to the amplifier gain G. In other words, more parts of the signal on both sides will be clipped if we want to use a higher amplifier gain G. Here we recall the clipping ratios, which are given by the normalized clipping levels on upper side and lower side:

$$\lambda_{upper} = \frac{x_{max}}{\sigma_x}, \tag{105}$$

$$\lambda_{lower} = -\frac{x_{min}}{\sigma_x} \tag{106}$$

and the asymmetric requirement: $\lambda_{upper} = \sqrt{\rho}\lambda_{lower}$.

6.4.2 Distortion in frequency-domain

The disadvantage of simple clipping is the introduced distortions in frequency-domain, which can disrupt information bits. To quantify these distortions, we continue to use error vector magnitude (EVM). However, different from the preliminary work in Chapter 4, in bit-loaded OFDM systems here, EVMs for different subgroups are supposed be considered and calculated separately:

$$\text{EVM}_i \triangleq \frac{1}{\sigma_X}\sqrt{\frac{1}{|\mathcal{I}_i|}\sum_{k\in\mathcal{I}_i}|E_k|^2}, \tag{107}$$

where $E_k = \bar{X}_k - X_k$, $\bar{X}_k = \text{DFT}(\bar{x}_n)$ and σ_X is the root mean square power (standard deviation) of the original symbol X_k. Since power loading is not considered here, σ_X

remains the same for different subcarriers. The minimum requirements of EVM vary for different subcarriers due to the selections of the constellation types. For example, the EVM thresholds are 17.5% (QPSK), 12.5% (16-QAM), and 8.0% (64-QAM), respectively, in 3GPP systems [42].

For simple clipping, the EVM is determined by the clipping ratios. To avoid too severe distortion, the clipping levels cannot be very low. On the other hand, the clipping distortions are equally distributed among all the subcarriers [56]. Thus, the clipping ratios are dominated by the subcarriers with the highest constellation order, even though the subcarriers with lower modulation order can tolerate more distortions. It motivates us to figure out a more aggressive and efficient clipping method to further reduce the PAPRs.

6.4.3 Constrained clipping with constellation-wise distortion mitigation

The constrained clipping is firstly proposed for RF OFDM systems [43]. The basic idea is to mitigate the distortions in frequency-domain so that the time-domain signal can be clipped more aggressively to further reduce the PAPR. In our VLC-OFDM systems, there are three special considerations. First of all, PAPR reduction is required for both sides and the requirements can be asymmetric. Secondly, we only care about in-band subcarriers, since there is no out-of-band application and LEDs act as low-pass filters [54]. Thirdly, different subcarriers use different modulation schemes so that the distortion mitigation in frequency-domain should be constellation-wise.

The basic structure of the constellation-wise constrained clipping method is shown in Fig. 29. At the beginning, the input time-domain signal x_n is simply clipped at preset clipping ratios λ_{upper} and λ_{lower}. Then the clipped signal $\bar{x}_n$ is transformed into the frequency-domain by DFT. Our objective is to mitigate the distortions caused by the simple clipping. Since different subcarriers use different constellations, the requirements of EVM will be subcarrier-dependent. Thus, in the next step, we divide

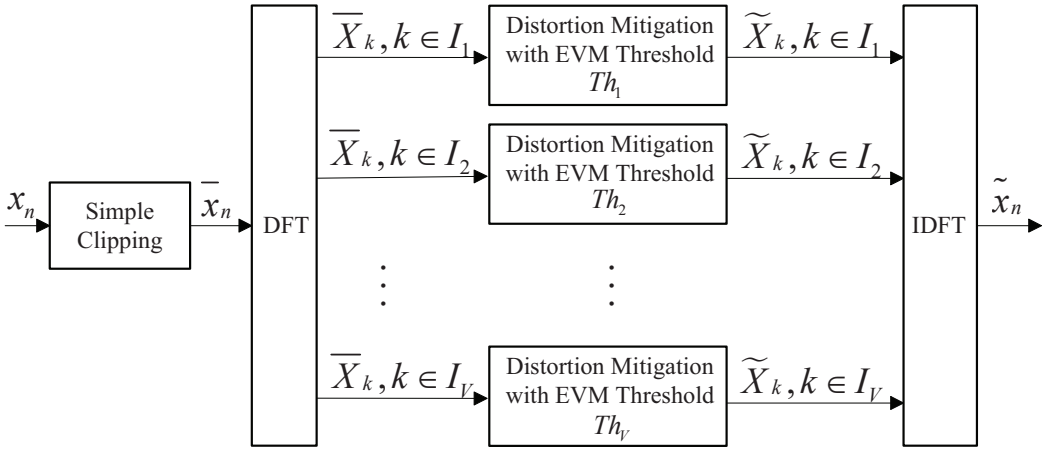

Figure 29: Block diagram of the constellation-wise constrained clipping method for VLC-OFDM.

the frequency-domain signal $\bar{X}_k$ into subgroups according to their selections of the modulation schemes. Each subgroup of subcarriers must satisfy the minimum EVM requirement, which is denoted by $Th_i, 1 \leq i \leq V$.

Actually, we only need to process the subcarriers in $\hat{\mathcal{I}}$, since the remaining subcarriers can be easily constructed by Hermitian symmetry or set as 0 (for 0th and $-N/2$th subcarriers). Next, we will show the details of the distortion mitigation. For subgroup $\hat{\mathcal{I}}_i, 1 \leq i \leq V$, to begin with, we sort $|E_k|$ in ascending order and find the largest subset $\mathcal{M}_i$ satisfying

$$\frac{1}{\sigma_X}\sqrt{\frac{1}{|\mathcal{M}_i|}\sum_{k\in\mathcal{M}_i}|E_k|^2} \leq Th_i, \tag{108}$$

where $|E_p| \leq |E_q|, \forall p \in \mathcal{M}_i, q \in \hat{\mathcal{I}}_i \backslash \mathcal{M}_i$.

From (108), we see that subcarriers in $\mathcal{M}_i$ satisfy the EVM requirement, so we keep them unchanged:

$$\tilde{X}_k = \bar{X}_k, \quad k \in \mathcal{M}_i. \tag{109}$$

For $\bar{X}_k, k \in \hat{\mathcal{I}}_i \backslash \mathcal{M}_i$, the distortions violate the EVM requirement so that they should be mitigated. A direct way is to select $\tilde{X}_k$ such that

$$|\tilde{E}_k| = |\tilde{X}_k - X_k| = \sigma_X Th_i, \quad k \in \hat{\mathcal{I}}_i \backslash \mathcal{M}_i. \tag{110}$$

Table 1: An example of bit-loading for VLC-OFDM systems ($N = 256$)

Subcarriers subset	Constellation type	EVM requirement
$\hat{\mathcal{I}}_1 = \{1, 2, \ldots, 42\}$	64-QAM	8%
$\hat{\mathcal{I}}_2 = \{43, 44, \ldots, 84\}$	16-QAM	12.5%
$\hat{\mathcal{I}}_3 = \{85, 86, \ldots, 127\}$	4-QAM	17.5%

Combining (108) and (110), we have the revised signal satisfying the constellation-wise EVM requirement $\text{EVM}_i\{\tilde{x}_n\} \leq Th_i, 1 \leq i \leq V$.

According to equation (110), the value of $\tilde{E}_k$ is not unique. On the other hand, revising signal in frequency-domain will change the signal in time-domain. Since the clipped time-domain signal $\bar{x}_n$ already has low UPAPR and LPAPR, we want the change between $\tilde{x}_n$ and $\bar{x}_n$, which is caused by distortion mitigation, to be minimized. Considering Parseval's theorem

$$\sum_{n=0}^{N-1} |\tilde{x}_n - \bar{x}_n|^2 = \sum_{1 \leq i \leq V} \sum_{k \in \mathcal{I}_i} |\tilde{X}_k - \bar{X}_k|^2, \tag{111}$$

It is equivalent to minimize $|\tilde{X}_k - \bar{X}_k|$. Thus, the optimal solution is

$$\tilde{X}_k = X_k + Th_i \cdot \sigma_X e^{j\angle E_k}, \quad k \in \hat{\mathcal{I}}_i \backslash \mathcal{M}_i. \tag{112}$$

By Hermitian symmetry and setting $\tilde{X}_0 = \tilde{X}_{-N/2} = 0$, we obtain all the subcarriers. After IDFT, we have the revised time-domain signal $\tilde{x}_n$, which satisfies constellation-wise EVM requirements and has low UPAPR and LPAPR.

6.5 Numerical results

In this section, we would like to evaluate the constellation-wise constrained clipping by simulations. Without loss of generality, we select $N = 256$ and asymmetric factor $\rho = 1$ dB. The bit-loading scheme is shown in Table 1 and the EVM requirements are chosen according to 3GPP specification.

As we mentioned before, without distortion mitigation, the clipping ratios on both sides are dominated by the subcarriers using the highest modulation order. Thus, the PAPR performance of simple clipping is limited.

For constrained clipping, the strategy is much more aggressive. For example, we select much higher clipping ratios $\lambda_{upper} = 5$ dB and $\lambda_{lower} = 4$ dB. Both UPAPR and LPAPR are further reduced, but the EVM turns to be around 20%. Moreover, the distortions are equally distributed among all the subcarriers no matter which constellation types are chosen, which is shown in Fig.30(a)-30(c). In this case, subcarriers with QPSK may be demodulated successfully, while subcarriers with 16QAM and 64QAM are severely corrupted so that the data transmission is unreliable.

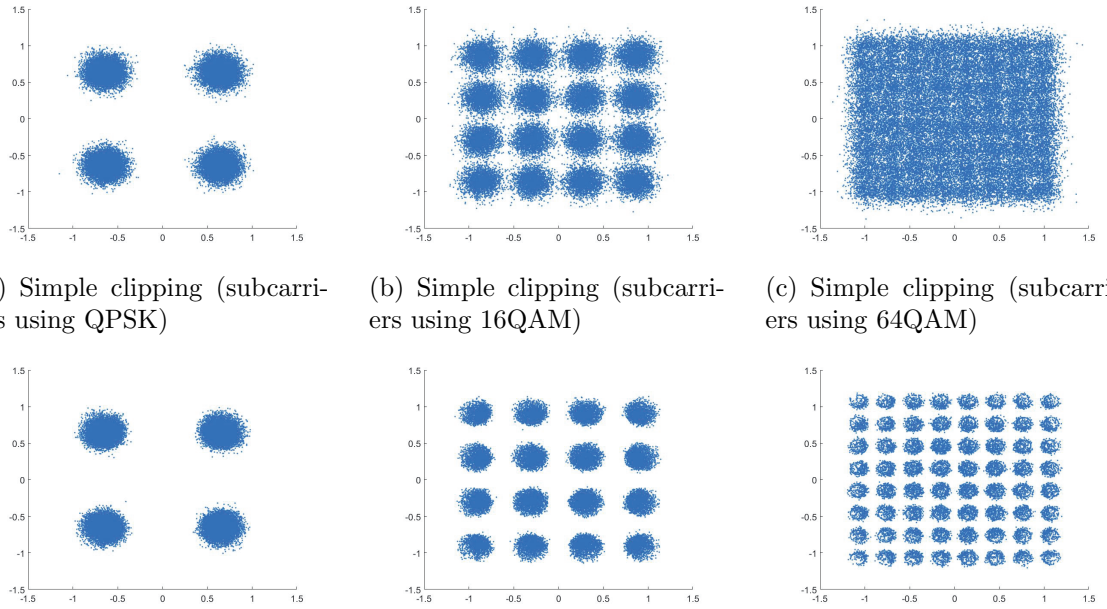

(a) Simple clipping (subcarriers using QPSK)

(b) Simple clipping (subcarriers using 16QAM)

(c) Simple clipping (subcarriers using 64QAM)

(d) Constellation-wise constrained clipping with EVM threshold 17.5% (subcarriers using QPSK)

(e) Constellation-wise constrained clipping with EVM threshold 12.5% (subcarriers using 16QAM)

(f) Constellation-wise constrained clipping with EVM threshold 8% (subcarriers using 64QAM)

Figure 30: Constellations of different subcarriers before and after distortion mitigation ($\lambda_{upper} = 5$ dB and $\lambda_{lower} = 4$ dB).

Thanks to the constellation-wise distortion mitigation, subcarriers with different modulation schemes are revised separately to meet the various EVM requirements. From Fig.30(d)-30(e), we see that the EVM of each subgroup is within the minimum requirement after the constrained clipping. In other words, the proposed constrained clipping helps "allocate" the clipping distortions among all the in-band subcarriers

reasonably and wisely to guarantee a reliable data transmission.

After making sure that all the EVM requirements are met, we would like to show the PAPR performance given by the constrained clipping. On the other hand, there are a lot of choices for preset upper and lower clipping ratios. Thus, we plot the joint CCDFs of the original OFDM signal and the processed signals after constrained clipping with various preset upper and lower clipping ratios in Fig. 31. The joint CCDFs are calculated from 50000 OFDM symbols. We see that the constellation-wise constrained clipping can achieve up to 4-dB PAPR reduction comparing to the original OFDM signal.

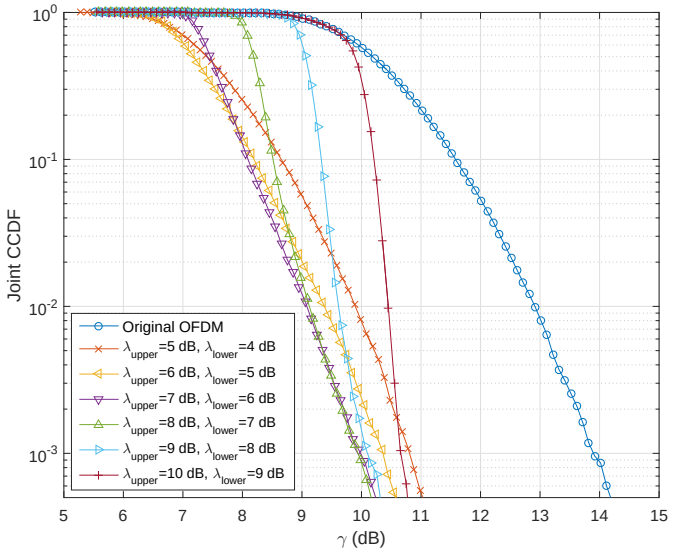

Figure 31: PAPR performances of constellation-wise constrained clipping with various upper clipping levels and lower clipping levels.

When it comes to the selections of the preset upper clipping ratio and lower clipping ratio, there is a tradeoff between peaks reduction by simple clipping and peaks regrowth by distortion mitigation. According to Fig. 31, we can use low preset clipping ratios to further reduce the PAPRs. However, if the clipping ratios are too low, there is a high possibility that the peaks on both sides will regrow after distortion mitigation in frequency-domain.

To better evaluate the tradeoff, we set an example of clipping level optimization for specific PAPR requirements in Fig. 32. We would like to minimize the probability that the OFDM signal will exceed 9 dB in UPAPR or 8 dB in LPAPR. Thus, we simulate the PAPR outage probability versus various clipping ratios. From Fig. 32, we see that the optimal upper clipping ratio is around 7.5 dB while the corresponding lower clipping ratio is 6.5 dB.

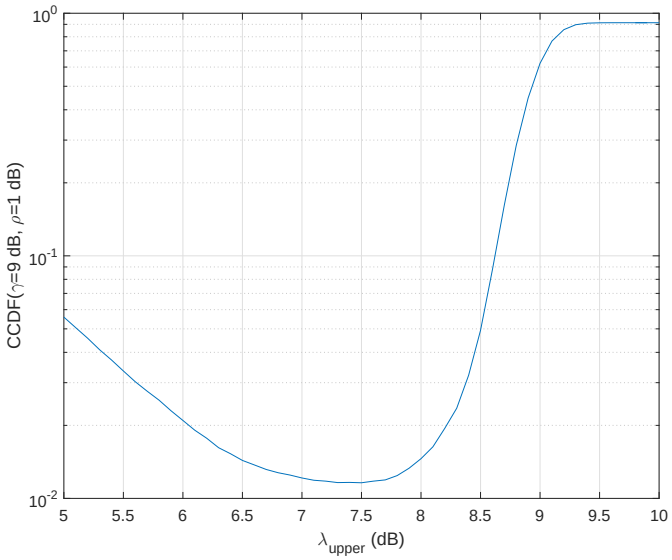

Figure 32: Probability that an OFDM signal exceeds 9 dB in UPAPR or 8 dB in LPAPR versus the upper clipping ratio λ_{upper} (ρ = 1 dB) by constellation-wise constrained clipping.

In the practical system design, the optimized preset clipping ratios can be calculated offline and stored in a look-up table. Then, the transmitter can adaptively select the preset clipping ratio according to the PAPR performance requirements. In Fig. 33, we plot the PAPR performances of constellation-wise constrained clipping with optimized preset upper clipping ratios and lower clipping ratios. Comparing to the original OFDM signal, we can always obtain 4-dB PAPR reduction.

In Fig. 33, we also plot the PAPR performance of the optimal distortion-based PAPR reduction method in [56] for comparison. The curve is theoretically optimal with the constellation-wise EVM constraints. However, we need to solve an

optimization problem for each OFDM symbol. Hence, it may not be suitable to a practical real-time VLC system. Comparing to the optimal solution, the proposed constellation-wise constrained clipping based on simple clipping is much less complicated. It does not require receiver side modifications, either. Although there is a 1-dB gap, the PAPR reduction performance is still very attractive. In the final analysis, the proposed constellation-wise constrained clipping can be a practical PAPR reduction solution in bit-loaded VLC-OFDM systems.

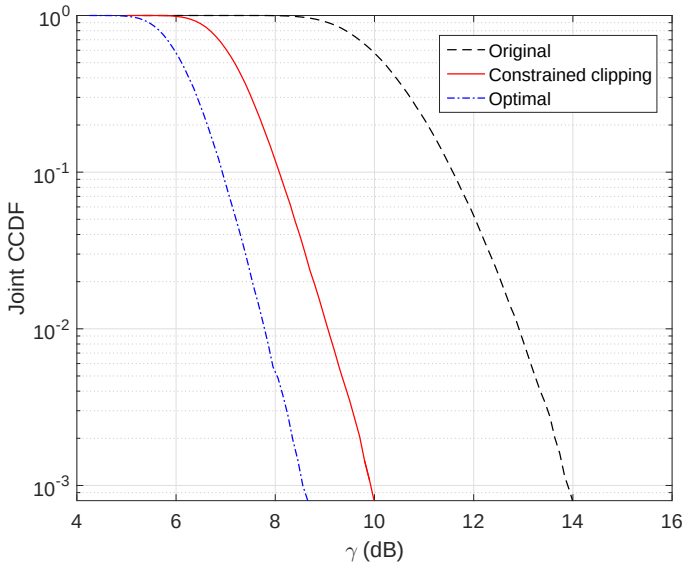

Figure 33: PAPR performances of constellation-wise constrained clipping with optimized preset upper clipping ratios and lower clipping ratios ($\rho = 1$ dB).

6.6 Conclusion

OFDM is applied in VLC systems due to its high spectrum efficiency and ability to combat ISI. On the other hand, bit-loading enables VLC-OFDM to better utilize the modulation bandwidth since the low-pass nature of LEDs results in frequency-selectivity. However, VLC-OFDM inherits the disadvantage of high PAPR, which has a negative impact on the power efficiency and utilization of system working range. Moreover, there are some special PAPR considerations according to the VLC-specific

requirements. VLC systems are real-valued and dynamic-range-limited, so both positive peaks and negative peaks should be taken into account. Since dimming control is important for illumination, the PAPR requirements on both upper side and lower side can be asymmetric and influenced by the DC bias. In this chapter, we consider a distortion-based PAPR reduction method based on simple clipping, which is named as constellation-wise constrained clipping. Such a method can be a practical solution in VLC-OFDM systems, because it has a relatively low complexity and there is no need for receiver modifications. Comparing to simple clipping, constrained clipping allows us to decrease the double-sided clipping levels to further reduce the UPAPR and LPAPR. In addition, the constellation-wise distortion mitigation helps revise and "relocate" the distortions among all the subcarriers reasonably. The simulation results validate the performance of double-sided PAPR reductions given by the constellation-wise constrained clipping.

CHAPTER VII

CONCLUSION

7.1 Contributions

This dissertation studied nonlinearities and nonlinear distortion mitigation techniques in optical wireless communications. Primary contributions of this dissertation are summarized here:

- We modeled/analyzed nonlinearities in OWC systems and summarized nonlinear distortion mitigation techniques. It can be a guideline to address the nonlinear issues in practical OWC system designs.
- We theoretically derived and proved an optimal input-output transfer function to minimize the nonlinear effects in dynamic-range-limited systems like OWC systems. The results can be applied for optimal linearization of nonlinear components and efficient transmission of signals with double-sided limitation.
- We studied double-sided PAPR reduction by taking into account some VLC-specific requirements and proposed a distortion-based method evolving from simple double-sided clipping. The proposed method can further reduce PAPRs on both sides with clipping distortion revision and it does not require modifications in receiver side.
- We designed optical MIMO transceiver to avoid double-sided clipping distortions and to fully utilize the spatial multiplexing. The proposed MMSE precoder/equalizer design can be a practical and efficient solution for indoor VLC-MIMO systems.

- We extended the constrained clipping method to the bit-loaded VLC-OFDM systems. With the proposed constellation-wise clipping distortion mitigation, the upper/lower PAPR performance can be enhanced and EVM requirements of all the in-band subcarriers can be satisfied.

Following is the list of publications related to the work presented in this dissertation.

Journal papers

J1. K. Ying, Z. Yu, R. J. Baxley and G. T. Zhou, "Optimization of signal-to-noise-plus-distortion ratio for dynamic-range-limited nonlinearities," *Digital Signal Processing*, vol. 36, pp. 104-114, Jan. 2015.

J2. K. Ying, Z. Yu, R. J. Baxley, H. Qian, G.-K. Chang and G. T. Zhou, "Nonlinear distortion mitigation in visible light communications," *IEEE Wireless Communications*, vol. 22, no. 2, pp. 36-45, Apr. 2015.

J3. K. Ying, H. Qian, R. J. Baxley and S. Yao, "Joint optimization of precoder and equalizer in MIMO VLC systems," *IEEE Journal on Select Areas in Communications*, vol. 33, no. 9, pp. 1949-1958, Sept. 2015.

J4. K. Ying, H. Qian, R. J. Baxley and G. T. Zhou, "MIMO transceiver design in dynamic-range-limited VLC systems," *IEEE Photonics Technology Letters*, vol. 28, no. 22, pp. 2593-2596, Nov. 2016.

J5. K. Ying, Z. Yu, R. J. Baxley and G. T. Zhou, "Constrained clipping for PAPR reduction in bit-loaded VLC-OFDM systems with dimming control," *Journal of Lightwave Technology*, under review.

J6. J. Wang, Z. Yu, K. Ying, J. Zhang, F. Lu, M. Xu, L. Cheng, X. Ma and G.-K. Chang, "Digital mobile fronthaul based on delta-sigma modulation for carrier

aggregation of LTE and FBMC signals," *Journal of Optical Communications and Networking*, to appear.

J7. J. Zhang, M. Xu, J. Wang, F. Lu, L. Cheng, H. Cho, K. Ying, J. Yu and G.-K. Chang, "Full-duplex quasi-gapless carrier-aggregation using FBMC in centralized radio-over-fiber heterogeneous networks," *Journal of Lightwave Technology*, to appear.

Conference papers

C1. K. Ying, Z. Yu, R. J. Baxley and G. T. Zhou, "Constrained clipping for PAPR reduction in VLC Systems with dimming control," in *Proc. IEEE Global Conference on Signal and Information Processing (GlobalSIP) 2015*, Orlando, FL, USA, Dec. 2015.

C2. Z. Yu, K. Ying, R. J. Baxley and G. T. Zhou, "PAPR reduction for bit-loaded OFDM in visible light communications," in *Proc. IEEE Wireless Communications and Networking Conference (WCNC) 2015*, New Orleans, LA, USA, Mar. 2015.

C3. J. Wang, Z. Yu, K. Ying, J. Zhang, F. Lu, M. Xu and G.-K. Chang, "Delta-sigma modulation for digital mobile fronthaul enabling carrier aggregation of 32 4G-LTE / 30 5G-FBMC signals in a single-λ 10-Gb/s IM-DD channel," in *Proc. Optical Fiber Communication Conference (OFC) 2016*, Anaheim, CA, USA, Mar. 2016.

C4. J. Wang, Z. Yu, K. Ying, J. Zhang, F. Lu, M. Xu, L. Cheng, X. Ma and G.-K. Chang, "10-Gbaud OOK / PAM4 digital mobile fronthaul based on one-bit / two-bit delta-sigma modulation supporting carrier aggregation of 32 LTE-A signals with up to 256 and 1024QAM," to appear in *Proc. European Conference on Optical Communications (ECOC) 2016*, Dsseldorf, Germany, Sept. 2016.

7.2 Future work

The work presented in this dissertation can be extended to the following topics:

- Study double-sided PAPR reductions in optical MIMO-OFDM systems.
- Mitigate nonlinear distortions with memory effects and time-varying characteristics.
- Implement hardware designs of MIMO-VLC systems.

APPENDIX A

PROOF OF LEMMA 1

Since we are solving the optimization problem w.r.t. a function, the functional derivative is introduced here [34,41]. By using the Dirac delta function $\delta(\cdot)$ as a test function, the notion of functional derivative is defined as:

$$\frac{\delta F[g(\gamma)]}{\delta g(\gamma_0)} = \lim_{\epsilon \to 0} \frac{F[g(\gamma) + \epsilon \delta(\gamma - \gamma_0)] - F[g(\gamma)]}{\epsilon}. \tag{113}$$

Just as the ordinary derivative operation, the linear property, product rule, and chain rule hold for functional derivatives. In addition, from (113), we infer that

$$\frac{\delta g(\gamma)}{\delta g(\gamma_0)} = \delta(\gamma - \gamma_0), \tag{114}$$

$$\frac{\delta g^2(\gamma)}{\delta g(\gamma_0)} = 2g(\gamma)\delta(\gamma - \gamma_0). \tag{115}$$

To maximize the SNDR w.r.t $g(\cdot)$, we need

$$\frac{\delta \text{SNDR}}{\delta g(\gamma_0)} = 0, \quad \forall \gamma_0 \in S. \tag{116}$$

We infer that

$$\begin{aligned} E[g(\gamma)] &= E[I_L(\gamma)g(\gamma)] + E[I_S(\gamma)g(\gamma)] + E[I_U(\gamma)g(\gamma)] \\ &= E[I_S(\gamma)g(\gamma)] + E[I_U(\gamma)] \\ &= E[I_S(\gamma)g(\gamma)] + C_0^U \end{aligned} \tag{117}$$

where C_0^U is defined as in (22). Similarly,

$$E[\gamma g(\gamma)] = E[I_S(\gamma)\gamma g(\gamma)] + C_1^U, \tag{118}$$

$$E[g^2(\gamma)] = E[I_S(\gamma)g^2(\gamma)] + C_0^U. \tag{119}$$

It easily follows that

$$C_0^L + C_0^S + C_0^U = 1, \tag{120}$$

$$C_1^L + C_1^S + C_1^U = 0 \tag{121}$$

and

$$C_0^L, C_0^S, C_0^U \geq 0. \tag{122}$$

Substituting (117), (118), and (119) into (14)

$$\text{SNDR} = \frac{N[g(\gamma)]}{D[g(\gamma)]} \tag{123}$$

where

$$Q[g(\gamma)] = E[I_S(\gamma)\gamma g(\gamma)] + C_1^U, \tag{124}$$

$$N[g(\gamma)] = Q^2[g(\gamma)], \tag{125}$$

$$Y[g(\gamma)] = E[I_S(\gamma)g(\gamma)] + C_0^U, \tag{126}$$

$$\begin{aligned} D[g(\gamma)] = E[I_S(\gamma)g^2(\gamma)] + C_0^U + \frac{\sigma_v^2}{A^2} \\ - Q^2[g(\gamma)] - Y^2[g(\gamma)]. \end{aligned} \tag{127}$$

Denote by $p(\gamma)$ the PDF of the random variable γ. Then

$$E[I_S(\gamma)g^2(\gamma)] = \int I_S(\gamma)g^2(\gamma)p(\gamma)d\gamma. \tag{128}$$

Taking the functional derivative w.r.t $g(\gamma_0)$, we obtain

$$\begin{aligned} & \frac{\delta E[I_S(\gamma)g^2(\gamma)]}{\delta g(\gamma_0)} \\ = & \int I_S(\gamma)2g(\gamma)\delta(\gamma - \gamma_0)p(\gamma)d\gamma \qquad (129) \\ = & \; 2g(\gamma_0)p(\gamma_0). \qquad (130) \end{aligned}$$

Similarly,

$$\frac{\delta E[I_S(\gamma)\gamma g(\gamma)]}{\delta g(\gamma_0)} = \gamma_0 p(\gamma_0), \tag{131}$$

$$\frac{\delta E[I_S(\gamma)g(\gamma)]}{\delta g(\gamma_0)} = p(\gamma_0). \tag{132}$$

Therefore,

$$\frac{\delta N[g(\gamma)]}{\delta g(\gamma_0)} = 2Q[g(\gamma)]\gamma_0 p(\gamma_0), \tag{133}$$

$$\frac{\delta D[g(\gamma)]}{\delta g(\gamma_0)} = 2g(\gamma_0)p(\gamma_0) - 2Q[g(\gamma)]\gamma_0 p(\gamma_0) - 2Y[g(\gamma)]p(\gamma_0). \tag{134}$$

Condition (116) requires

$$\frac{\delta N[g(\gamma)]}{\delta g(\gamma_0)} D[g(\gamma)] = \frac{\delta D[g(\gamma)]}{\delta g(\gamma_0)} N[g(\gamma)]. \tag{135}$$

Substituting and simplifying, we obtain

$$g(\gamma_0) = \frac{\gamma_0}{\eta} + \beta \tag{136}$$

where

$$\eta = \frac{E[I_S(\gamma)\gamma g(\gamma)] + C_1^U}{E[I_S(\gamma)g^2(\gamma)] + C_0^U - \beta^2 + \sigma_v^2/A^2}, \tag{137}$$

$$\beta = E[g(\gamma)] = E[I_S(\gamma)g(\gamma)] + C_0^U \tag{138}$$

as the solution to (116). Since (136) holds $\forall \gamma_0 \in S$, we must have

$$g(\gamma) = \frac{\gamma}{\eta} + \beta, \quad \forall \gamma \in S. \tag{139}$$

Substituting (139) into (137) and (138), we obtain

$$\eta = \frac{C_1^U + C_2^S/\eta + C_1^S\beta}{C_0^U + C_2^S/\eta^2 + 2\beta C_1^S/\eta + \beta^2 C_0^S - \beta^2 + \sigma_v^2/A^2}, \tag{140}$$

$$\beta = C_0^U + C_1^S/\eta + \beta C_0^S \tag{141}$$

where C_0^S, C_1^S and C_2^S are given by (22).

Solving for η and β, and simplifying, we obtain (20) and (21).

In summary, under the dynamic-range constraint, the optimal $g(\cdot)$ that maximizes the SNDR is given by (139), where η and β are given by (20) and (21).

APPENDIX B

PROOF OF LEMMA 2

Comparing (17) with (139), we infer that $0 < \frac{\gamma}{\eta} + \beta < 1$ on S. Therefore, the set S must be a subset of $S^\star = (-\beta\eta, \eta - \beta\eta)$ if $\eta > 0$ or $S^\star = (\eta - \beta\eta, -\beta\eta)$ if $\eta < 0$. The objective here is to determine the optimal S such that the SNDR is maximized.

To further this objective, we rewrite SNDR as

$$\text{SNDR}^{-1} = \frac{E[g^2(\gamma)] - E^2[g(\gamma)] + \frac{\sigma_v^2}{A^2}}{E^2[\gamma g(\gamma)]} - 1. \tag{142}$$

Since $g(\gamma) = \frac{\gamma}{\eta} + \beta$ for $\gamma \in S$, we infer that

$$\begin{aligned} E[g(\gamma)] &= C_0^U + C_1^S/\eta + \beta C_0^S, & (143)\\ E[g^2(\gamma)] &= C_0^U + C_2^S/\eta^2 + 2\beta C_1^S/\eta + \beta^2 C_0^S, & (144)\\ E[\gamma g^2(\gamma)] &= C_1^U + C_2^S/\eta + C_1^S\beta. & (145) \end{aligned}$$

From (140), we have

$$\begin{aligned} \sigma_v^2/A^2 = {} & C_1^U/\eta + C_2^S/\eta^2 + C_1^S\beta/\eta + \beta^2 \\ & - C_0^U - C_2^S/\eta^2 - 2\beta C_1^S/\eta - \beta^2 C_0^S. \end{aligned} \tag{146}$$

Thus, (142) can be further simplified to

$$\begin{aligned} \text{SNDR}^{-1} &= \frac{C_1^U/\eta + C_2^S/\eta^2 + C_1^S\beta/\eta}{(C_1^U + C_2^S/\eta + C_1^S\beta)^2} - 1 & (147)\\ &= (C_2^S + \eta C_1^U + \eta C_1^S\beta)^{-1} - 1. & (148) \end{aligned}$$

As a result, the original problem can be written as

$$\max_{\substack{L,S,U \\ L\cup S\cup U = R \\ S\subseteq(-\beta\eta,\eta-\beta\eta) \text{ or } (\eta-\beta\eta,-\beta\eta)}} \quad C_2^S + \eta C_1^U + \eta C_1^S\beta \tag{149}$$

Recall that C_2^S, C_1^S, C_1^U, η, and β are all functions of L, S, and U. Set

$$\begin{aligned} & R(L,S,U) \\ = \; & C_2^S + \eta(L,S,U)\beta(L,S,U)C_1^S + \eta(L,S,U)C_1^U \\ = \; & \frac{N_0(L,S,U)}{D_0(L,S,U)} \end{aligned} \tag{150}$$

where

$$\begin{aligned} & N_0(L,S,U) \\ & = C_2^S C_0^U C_0^L + C_0^U (C_1^S)^2 + 2C_0^U C_1^U C_1^S + (C_1^U)^2 \\ & - C_0^S (C_1^U)^2 + C_2^S (1 - C_0^S)\sigma_v^2/A^2 + (C_1^S)^2 \sigma_v^2/A^2 \end{aligned} \tag{151}$$

and

$$D_0(L,S,U) = C_0^U C_0^L + (1 - C_0^S)\sigma_v^2/A^2. \tag{152}$$

Differing from the traditional optimization problem, the variables here are sets. Let us consider two cases.

Case 1. Suppose that (L, S, U) is a feasible solution. Let us consider a set $S_1 \subset S$ where

$$S_1 = S - \Delta_1, \tag{153}$$

$$L_1 = L + \Delta_1, \tag{154}$$

$$U_1 = U \tag{155}$$

which means a subset of S is partitioned into L.

Fig. 34 demonstrates an example of Case 1. Then we have

$$R(L_1,S_1,U_1) = \frac{N_1(L_1,S_1,U_1)}{D_1(L_1,S_1,U_1)} \tag{156}$$

where

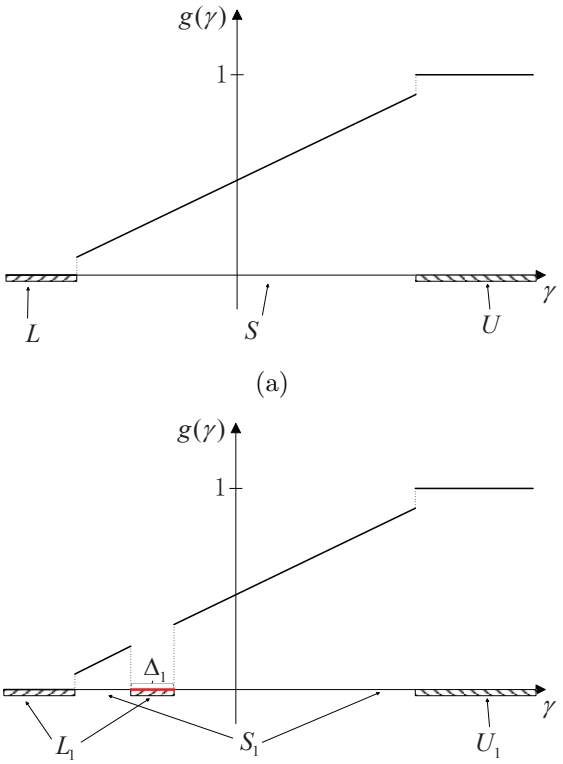

Figure 34: Example of Case 1. (a) L, S, U. (b) $L_1 = L + \Delta_1$, $S_1 = S - \Delta_1$, $U_1 = U$.

$$
\begin{aligned}
& N_1(L_1, S_1, U_1) \\
&= (C_2^S - C_2^{\Delta_1}) C_0^U (C_0^L + C_0^{\Delta_1}) + C_0^U (C_1^S - C_1^{\Delta_1})^2 \\
&+ 2C_0^U (C_1^S - C_1^{\Delta_1}) C_1^U - (C_0^S - C_0^{\Delta_1})(C_1^U)^2 \\
&+ (C_2^S - C_2^{\Delta_1})(1 - C_0^S + C_0^{\Delta_1})\sigma_v^2/A^2 \\
&+ (C_1^S - C_1^{\Delta_1})^2 \sigma_v^2/A^2 + (C_1^U)^2 \\
&= N_0(L, S, U) + C_2^S C_0^U C_0^{\Delta_1} - C_0^U C_0^L C_2^{\Delta_1} \\
&- C_0^U C_2^{\Delta_1} C_0^{\Delta_1} - 2C_0^U C_1^S C_1^{\Delta_1} + C_0^U (C_1^{\Delta_1})^2 \\
&- 2C_0^U C_1^U C_1^{\Delta_1} + (C_1^U)^2 C_0^{\Delta_1} - C_2^{\Delta_1} C_0^{\Delta_1} + (C_1^{\Delta_1})^2 \\
&+ [C_2^S C_0^{\Delta_1} - (1 - C_0^S) C_2^{\Delta_1} - 2C_1^S C_1^{\Delta_1}]\sigma_v^2/A^2
\end{aligned} \tag{157}
$$

and

$$
\begin{aligned}
& D_1(L_1, S_1, U_1) \\
&= C_0^U (C_0^L + C_0^{\Delta_1}) + (1 - C_0^S + C_0^{\Delta_1})\sigma_v^2/A^2 \\
&= D_0(L, S, U) + C_0^U C_0^{\Delta_1} + C_0^{\Delta_1}\sigma_v^2/A^2.
\end{aligned} \tag{158}
$$

Next, we compare $R(L_1, S_1, U_1)$ and $R(L, S, U)$ to help us establish the optimal S maximizing the SNDR. However, it is a challenge to make the comparison directly since there are too many terms in the objective expression. Here, we utilize a two-step comparison.

First, rewrite

$$
\begin{aligned}
& N_1(L_1, S_1, U_1) \\
&= N_0(L, S, U) + [C_2^S C_0^U + (C_1^U)^2] C_0^{\Delta_1} - C_0^U C_0^L C_2^{\Delta_1} \\
&- 2C_0^U (C_1^S + C_1^U) C_1^{\Delta_1} + C_0^U [(C_1^{\Delta_1})^2 - C_2^{\Delta_1} C_0^{\Delta_1}] \\
&+ [C_2^S C_0^{\Delta_1} - (1 - C_0^S) C_2^{\Delta_1} - 2C_1^S C_1^{\Delta_1}] \sigma_v^2 / A^2 \\
&+ [(C_1^{\Delta_1})^2 - C_2^{\Delta_1} C_0^{\Delta_1}] \sigma_v^2 / A^2 \\
&\leq N_0(L, S, U) + [C_2^S C_0^U + (C_1^U)^2] C_0^{\Delta_1} \\
&- C_0^U C_0^L C_2^{\Delta_1} + 2C_0^U C_1^L C_1^{\Delta_1} \\
&+ [C_2^S C_0^{\Delta_1} - (1 - C_0^S) C_2^{\Delta_1} - 2C_1^S C_1^{\Delta_1}] \sigma_v^2 / A^2 \\
&= \hat{N}_1(L_1, S_1, U_1)
\end{aligned}
\tag{159}
$$

where

$$
(C_1^{\Delta_1})^2 \leq C_2^{\Delta_1} C_0^{\Delta_1} \tag{160}
$$

by the Cauchy-Schwartz inequality $E^2[\theta\phi] \leq E[\theta^2]E[\phi^2]$ with $\theta = \gamma I_{\Delta_1}(\gamma)$ and $\phi = I_{\Delta_1}(\gamma)$.

Next, we use $\hat{N}_1(L_1, S_1, U_1)$ instead of $N_1(L_1, S_1, U_1)$ to make the comparison. Consider

$$
\begin{aligned}
& \frac{\hat{N}_1(L_1, S_1, U_1)}{D_1(L_1, S_1, U_1)} - \frac{N_0(L, S, U)}{D_0(L, S, U)} \\
&= \frac{\hat{N}_1(L_1, S_1, U_1) D_0(L, S, U) - N_0(L, S, U) D_1(L_1, S_1, U_1)}{D_1(L_1, S_1, U_1) D_0(L, S, U)}
\end{aligned}
\tag{161}
$$

where

$$
\hat{N}_1(L_1, S_1, U_1) D_0(L, S, U) - N_0(L, S, U) D_1(L_1, S_1, U_1) \leq 0 \tag{162}
$$

which is further expanded as

$$
\begin{aligned}
&\hat{N}_1(L_1,S_1,U_1)D_0(L,S,U) - N_0(L,S,U)D_1(L_1,S_1,U_1)\\
&= \{[C_2^S C_0^U + (C_1^U)^2]D_0(L,S,U) - C_0^U N_0(L,S,U)\}C_0^{\Delta_1}\\
&+ [C_2^S D_0(L,S,U) - N_0(L,S,U)]C_0^{\Delta_1}\sigma_v^2/A^2\\
&- C_0^U C_0^L D_0(L,S,U)C_2^{\Delta_1} - (1-C_0^S)D_0(L,S,U)C_2^{\Delta_1}\sigma_v^2/A^2\\
&+ 2C_0^U C_1^L D_0(L,S,U)C_1^{\Delta_1} - 2C_1^S D_0(L,S,U)C_1^{\Delta_1}\sigma_v^2/A^2\\
&= 2(C_0^U C_1^L - C_1^S\sigma_v^2/A^2)[C_0^U C_0^L + (1-C_0^S)\sigma_v^2/A^2]C_1^{\Delta_1} - (C_1^S\sigma_v^2/A^2 - C_0^U C_1^L)^2 C_0^{\Delta_1}\\
&- [C_0^U C_0^L + (1-C_0^S)\sigma_v^2/A^2]^2 C_2^{\Delta_1}\\
&\le 2|C_0^U C_1^L - C_1^S\sigma_v^2/A^2|[C_0^U C_0^L + (1-C_0^S)\sigma_v^2/A^2]|C_1^{\Delta_1}| - (C_1^S\sigma_v^2/A^2 - C_0^U C_1^L)^2 C_0^{\Delta_1}\\
&- [C_0^U C_0^L + (1-C_0^S)\sigma_v^2/A^2]^2 C_2^{\Delta_1}\\
&= 2\underbrace{|C_0^U C_1^L - C_1^S\sigma_v^2/A^2|[C_0^U C_0^L + (1-C_0^S)\sigma_v^2/A^2]}_{\ge 0}\underbrace{\left(|C_1^{\Delta_1}| - \sqrt{C_0^{\Delta_1}}\sqrt{C_2^{\Delta_1}}\right)}_{\le 0}\\
&- \underbrace{\left\{|C_1^S\sigma_v^2/A^2 - C_0^U C_1^L|\sqrt{C_0^{\Delta_1}} - [C_0^U C_0^L + (1-C_0^S)\sigma_v^2/A^2]\sqrt{C_2^{\Delta_1}}\right\}^2}_{\ge 0}\\
&\le 0.
\end{aligned}
\tag{163}
$$

Since both $D_1(L_1,S_1,U_1)$ and $D_0(L,S,U)$ are greater than zero, it can be concluded that

$$
R(L_1,S_1,U_1) \le \frac{\hat{N}_1(L_1,S_1,U_1)}{D_1(L_1,S_1,U_1)} \le R(L,S,U). \tag{164}
$$

Case 1 demonstrates that the SNDR will be decreased if any subset of S is occupied by L. Let us now consider another case.

Case 2. $S_2 \subset S$ where

$$S_2 = S - \Delta_2, \tag{165}$$

$$L_2 = L, \tag{166}$$

$$U_2 = U + \Delta_2 \tag{167}$$

which means a subset of S is partitioned into U.

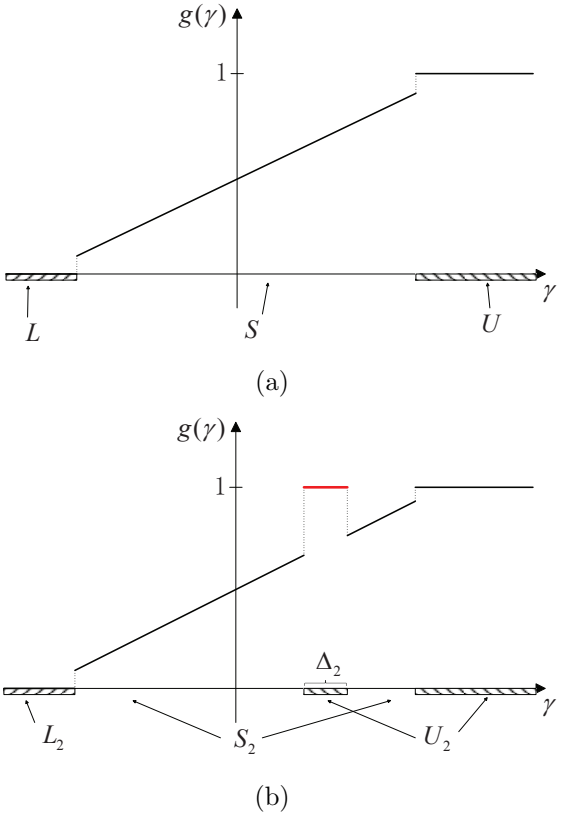

Figure 35: Example of Case 2. (a) L, S, U. (b) $L_2 = L$, $S_2 = S - \Delta_2$, $U_2 = U + \Delta_2$.

Fig. 35 demonstrates an example of Case 2. Then we have

$$R(L_2, S_2, U_2) = \frac{N_2(L_2, S_2, U_2)}{D_2(L_2, S_2, U_2)} \tag{168}$$

where

$$
\begin{aligned}
&N_2(L_2, S_2, U_2) \\
&= (C_2^S - C_2^{\Delta_2})(C_0^U + C_0^{\Delta_2})C_0^L + (C_0^U + C_0^{\Delta_2})(C_1^S - C_1^{\Delta_2})^2 \\
&+ 2(C_0^U + C_0^{\Delta_2})(C_1^U + C_1^{\Delta_2})(C_1^S - C_1^{\Delta_2}) \\
&+ (C_1^U + C_1^{\Delta_2})^2 - (C_0^S - C_0^{\Delta_2})(C_1^U + C_1^{\Delta_2})^2 \\
&+ (C_2^S - C_2^{\Delta_2})(1 - C_0^S + C_0^{\Delta_2})\sigma_v^2/A^2 + (C_1^S - C_1^{\Delta_2})^2\sigma_v^2/A^2 \\
&= N_0(L, S, U) + C_2^S C_0^L C_0^{\Delta_2} - C_0^U C_0^L C_2^{\Delta_2} - C_0^L C_2^{\Delta_2} C_0^{\Delta_2} \\
&- 2C_0^U C_1^S C_1^{\Delta_2} + C_0^U (C_1^{\Delta_2})^2 + (C_1^S)^2 C_0^{\Delta_2} - 2C_1^S C_0^{\Delta_2} C_1^{\Delta_2} \\
&+ C_0^{\Delta_2}(C_1^{\Delta_2})^2 + 2C_0^U C_1^S C_1^{\Delta_2} + 2C_1^U C_1^S C_0^{\Delta_2} \\
&+ 2C_1^S C_0^{\Delta_2} C_1^{\Delta_2} - 2C_0^U C_1^U C_1^{\Delta_2} - 2C_0^U (C_1^{\Delta_2})^2 \\
&- 2C_1^U C_0^{\Delta_2} C_1^{\Delta_2} - 2C_0^{\Delta_2}(C_1^{\Delta_2})^2 + 2C_1^U C_1^{\Delta_2} + (C_1^{\Delta_2})^2 \\
&- 2C_0^S C_1^U C_1^{\Delta_2} - C_0^S (C_1^{\Delta_2})^2 + (C_1^U)^2 C_0^{\Delta_2} + 2C_1^U C_0^{\Delta_2} C_1^{\Delta_2} \\
&+ C_0^{\Delta_2}(C_1^{\Delta_2})^2 + [C_2^S C_0^{\Delta_2} - (1 - C_0^S)C_2^{\Delta_2} - C_2^{\Delta_2} C_0^{\Delta_2} \\
&+ (C_1^{\Delta_2})^2 v - 2C_1^S C_1^{\Delta_2}]\sigma_v^2/A^2
\end{aligned} \tag{169}
$$

and

$$
\begin{aligned}
&D_2(L_2, S_2, U_2) \\
&= (C_0^U + C_0^{\Delta_2})C_0^L + (1 - C_0^S + C_0^{\Delta_2})\sigma_v^2/A^2 \\
&= D_0(L, S, U) + C_0^L C_0^{\Delta_2} + C_0^{\Delta_2}\sigma_v^2/A^2.
\end{aligned} \tag{170}
$$

In Case 2, we also try to determine the difference between $R(L_2, S_2, U_2)$ and $R(L, S, U)$ by utilizing the two-step comparison.

First, rewrite

$$
\begin{aligned}
&N_2(L_2, S_2, U_2) \\
&= N_0(L, S, U) + [C_2^S C_0^L + (C_1^U + C_1^S)^2] C_0^{\Delta_2} - C_0^U C_0^L C_2^{\Delta_2} \\
&+ 2C_0^L C_1^U C_1^{\Delta_2} + C_0^L [(C_1^{\Delta_2})^2 - C_2^{\Delta_1} C_0^{\Delta_1}] \\
&+ [C_2^S C_0^{\Delta_2} - (1 - C_0^S) C_2^{\Delta_2} - 2C_1^S C_1^{\Delta_2}] \sigma_v^2 / A^2 \\
&+ [(C_1^{\Delta_2})^2 - C_2^{\Delta_2} C_0^{\Delta_2}] \sigma_v^2 / A^2 \\
&\leq N_0(L, S, U) + [C_2^S C_0^L + (C_1^L)^2] C_0^{\Delta_2} \\
&- C_0^U C_0^L C_2^{\Delta_2} + 2C_0^L C_1^U C_1^{\Delta_2} \\
&+ [C_2^S C_0^{\Delta_2} - (1 - C_0^S) C_2^{\Delta_2} - 2C_1^S C_1^{\Delta_2}] \sigma_v^2 / A^2 \\
&= \hat{N}_2(L_2, S_2, U_2)
\end{aligned}
\tag{171}
$$

where by the Cauchy-Schwartz inequality,

$$
(C_1^{\Delta_2})^2 \leq C_2^{\Delta_2} C_0^{\Delta_2}. \tag{172}
$$

Second, consider

$$
\begin{aligned}
&\frac{\hat{N}_2(L_2, S_2, U_2)}{D_2(L_2, S_2, U_2)} - \frac{N_0(L, S, U)}{D_0(L, S, U)} \\
&= \frac{\hat{N}_2(L_2, S_2, U_2) D_0(L, S, U) - N_0(L, S, U) D_2(L_2, S_2, U_2)}{D_2(L_2, S_2, U_2) D_0(L, S, U)}
\end{aligned}
\tag{173}
$$

where

$$
\hat{N}_2(L_2, S_2, U_2) D_0(L, S, U) - N_0(L, S, U) D_2(L_2, S_2, U_2) \leq 0 \tag{174}
$$

which is further expanded as

$$
\begin{aligned}
&\hat{N}_2(L_2,S_2,U_2)D_0(L,S,U) - N_0(L,S,U)D_2(L_2,S_2,U_2)\\
&= \{[C_2^S C_0^L + (C_1^L)^2]D_0(L,S,U) - C_0^L N_0(L,S,U)\}C_0^{\Delta_2}\\
&+ [C_2^S D_0(L,S,U) - N_0(L,S,U)]C_0^{\Delta_2}\sigma_v^2/A^2\\
&- C_0^U C_0^L D_0(L,S,U)C_2^{\Delta_2} - (1-C_0^S)D_0(L,S,U)C_2^{\Delta_2}\sigma_v^2/A^2\\
&+ 2C_0^L C_1^U D_0(L,S,U)C_1^{\Delta_2} - 2C_1^S D_0(L,S,U)C_1^{\Delta_2}\sigma_v^2/A^2\\
&= 2(C_0^L C_1^U - C_1^S\sigma_v^2/A^2)[C_0^U C_0^L + (1-C_0^S)\sigma_v^2/A^2]C_1^{\Delta_1}\\
&- (C_1^S\sigma_v^2/A^2 - C_0^L C_1^U)^2 C_0^{\Delta_2} - [C_0^U C_0^L + (1-C_0^S)\sigma_v^2/A^2]^2 C_2^{\Delta_2}\\
&\le 2|C_0^L C_1^U - C_1^S\sigma_v^2/A^2|[C_0^U C_0^L + (1-C_0^S)\sigma_v^2/A^2]|C_1^{\Delta_2}|\\
&- (C_1^S\sigma_v^2/A^2 - C_0^L C_1^U)^2 C_0^{\Delta_2} - [C_0^U C_0^L + (1-C_0^S)\sigma_v^2/A^2]^2 C_2^{\Delta_2}\\
&= 2\underbrace{|C_0^L C_1^U - C_1^S\sigma_v^2/A^2|[C_0^U C_0^L + (1-C_0^S)\sigma_v^2/A^2]}_{\ge 0}\underbrace{\left(|C_1^{\Delta_2}| - \sqrt{C_0^{\Delta_2}}\sqrt{C_2^{\Delta_2}}\right)}_{\le 0}\\
&- \underbrace{\left\{|C_1^S\sigma_v^2/A^2 - C_0^L C_1^U|\sqrt{C_0^{\Delta_2}} - [C_0^U C_0^L + (1-C_0^S)\sigma_v^2/A^2]\sqrt{C_2^{\Delta_2}}\right\}^2}_{\ge 0}\\
&\le 0.
\end{aligned}
\tag{175}
$$

Since both $D_2(L_2,S_2,U_2)$ and $D_0(L,S,U)$ are greater than zero, it can be concluded

$$
R(L_2,S_2,U_2) \le \frac{\hat{N}_2(L_2,S_2,U_2)}{D_2(L_2,S_2,U_2)} \le R(L,S,U). \tag{176}
$$

Case 2 demonstrates that the SNDR will also be decreased if any subset of S is occupied by U.

Additionally, Case 1 and Case 2 also imply that the SNDR can be increased if S can be enlarged by occupying the subsets of L and U. Thus, Lemma 2 holds and the optimal S is $S^\star = (-\beta\eta, \eta - \beta\eta)$ if $\eta > 0$ or $S^\star = (\eta - \beta\eta, -\beta\eta)$ if $\eta < 0$.

REFERENCES

[1] H. Elgala, R. Mesleh and H. Haas, "Indoor optical wireless communication: Potential and state-of-the-art," *IEEE Communications Magazine*, vol. 49, no. 9, pp. 56-62, Dec. 2011.

[2] IEEE Std 802.15.7, IEEE Standard for Local and metropolitan area networks - Part 15.7: Short-range wireless optical communication using visible light, Sept. 2011.

[3] A. Jovicic, J. Li and T. Richardson, "Visible light communication: opportunities, challenges and the path to market," *IEEE Communications Magazine*, vol. 51, no. 12, pp. 26-32, Dec. 2013.

[4] E. F. Schubert, *Light Emitting Diodes*, 2nd ed. Cambridge, U.K.: Cambridge Univ. Press, 2006.

[5] J. M. Kahn and J. R. Barry, "Wireless Infrared Communications," *Proc. IEEE*, vol. 85, no. 2, pp. 265-298, Feb. 1997.

[6] B. Inan, S. C. J. Lee, S. Randel, I. Neokosmidis, A. M. J. Koonen and J. W. Walewski, "Impact of LED nonlinearity on discrete multitone modulation," *Journal of Optical Communications and Networking*, vol. 1, no. 5, pp. 439-451, Oct. 2009.

[7] I. Neokosmidis, T. Kamalakis, J. W. Walewski, B. Inan, and T. Sphicopoulos, "Impact of nonlinear LED transfer function on discrete multi-tone modulation: analytical approach," *Journal of Lightwave Technology*, vol. 27, no. 22, pp. 4970-4978, Nov. 2009.

[8] H. Elgala, R. Mesleh and H. Haas, "Non-linearity effects and predistortion in optical OFDM wireless transmission using LEDs," *International Journal of Ultra Wideband Communications and Systems*, vol. 1, no. 2, pp. 143-150, Nov. 2009.

[9] D. Tsonev, S. Sinanovic, H. Haas, "Complete modeling of nonlinear distortion in ofdm-based optical wireless communication," *Journal of Lightwave Technology*, vol. 31, no. 18, pp. 3064-3076, Sept. 2013.

[10] H. Elgala, R. Mesleh and H. Haas, "A study of LED nonlinearity effects on optical wireless transmission using OFDM," in *Proc. IFIP International Conference on Wireless and Optical Communications Networks*, pp. 1-5, Apr. 2009.

[11] J. Vucic, C. Kottke, S. Nerreter, K. D. Langer and J. W. Walewski "513 Mbit/s visible light communications link based on DMT-modulation of a white LED," *Journal of Lightwave Technology*, vol. 28, no. 24, pp. 3512-3518, Dec. 2010.

[12] H. Elgala, R. Mesleh and H. Haas, "An LED model for intensity-modulated optical communication systems," *IEEE Photonics Technology Letters*, vol. 22, no. 11, pp. 835-837, June 2010.

[13] I. Stefan, H. Elgala and H. Haas, "Study of dimming and LED nonlinearity for ACO-OFDM based VLC systems," in *Proc. IEEE Wireless Communications and Networking Conference (WCNC)*, pp. 990-995, Apr. 2012.

[14] Z. Yu, R. J. Baxley and G. T. Zhou, "EVM and achievable data rate analysis of clipped OFDM signals in visible light communication," *EURASIP Journal on Wireless Communications and Networking*, vol. 2012, no. 321, pp. 1-16, Oct., 2012.

[15] T. Kamalakis, J. W. Walewski, G. Ntogari, and G. Mileounis, "Empirical Volterra-series modeling of commercial lightemitting diodes," *Journal of Lightwave Technology*, vol. 29, no. 14, pp. 2146-2155, Jul. 2011.

[16] H. Qian, S. Yao, S. Cai and T. Zhou, "Adaptive postdistortion for nonlinear LEDs in visible light communications," *IEEE Photonics Journal*, vol. 6, no. 4, pp. 1-8, Aug. 2014.

[17] T.-P. Sun and C.-H. Wang, "Specially designed driver circuits to stabilize LED light output without a photodetector," *IEEE Transactions on Power Elctronics*, vol. 27, no. 9, pp. 4140-4152, Sept. 2012.

[18] K. H. Loo, W.-K. Lun, S.-C. Tan, Y. M. Lai and C. K. Tse, "On driving techniques for LEDs: toward a generalized methodology," *IEEE Transactions on Power Elctronics*, vol. 24, no. 12, pp. 2967-2976, Dec. 2009.

[19] K. Bandara, P. Niroopan and Y.-H. Chung, "PAPR reduced OFDM visible light communication using exponential nonlinear companding," in *Proc. IEEE International Conference on Microwaves, Communications, Antennas and Electronic Systems (COMCAS)*, pp. 1 - 5, Oct. 2013.

[20] H. Zhang, Y. Yuan and W. Xu, "PAPR reduction for DCO-OFDM visible light communications via semidefinite relaxation," *IEEE Photonics Technology Letters*, vol. 26, no. 17, pp. 1718-1721, Sept. 2014.

[21] R. Mesleh, H. Elgala and H. Haas, "LED nonlinearity mitigation techniques in optical wireless OFDM communication systems," *Journal of Optical Communications and Networking*, vol. 4, no. 11, pp. 865-875, Nov. 2012.

[22] Z. Yu, R. J. Baxley and G. T. Zhou, "Peak-to-average power ratio and illumination-to-communication efficiency considerations in visible light OFDM systems," in *Proc. IEEE International Conference on Acoustics, Speech and Signal Processing (ICASSP)*, pp. 5397-5401, May 2013.

[23] Z. Yu, R. J. Baxley and G. T. Zhou, "Distributions of upper PAPR and lower PAPR of OFDM signals in visible light communications,"in *Proc. IEEE International Conference on Acoustics, Speech and Signal Processing (ICASSP)*, pp. 355-359, May 2014.

[24] Z. Yu, R. J. Baxley and G. T. Zhou, "Iterative clipping for PAPR reduction in visible light OFDM communications," in *Proc. IEEE Military Communications Conference*, pp. 1681-1686, Oct. 2014.

[25] Z. Yu, R. J. Baxley and G. T. Zhou, "Impulses injection for PAPR reduction in visible light OFDM communications," in *Proc. IEEE Global Conference on Signal and Information Processing (GlobalSIP)*, pp. 73-77, Dec. 2014.

[26] W. O. Popoola, Z. Ghassemlooy and B. G. Stewart, "Pilot-assisted PAPR reduction technique for optical OFDM communication systems," *Journal of Lightwave Technology*, vol. 32, no. 71, pp. 1374-1382, Apr., 2014.

[27] S. Slimane, "Reducing the peak-to-average power ratio of OFDM signals through precoding," *IEEE Transactions on Vehicular Technology*, vol. 56, no. 2, pp. 686-395, Mar., 2007.

[28] G. Stepniak, J. Siuzdak and P. Zwierko, "Compensation of a VLC phosphorescent white LED nonlinearity by means of Volterra DFE," *IEEE Photonics Technology Letters*, vol. 25, no. 16, pp. 1597-1600, Aug. 2013.

[29] Y. Wang, X. Huang, J. Zhang, Y. Wang and N. Chi, "Enhanced performance of visible light communication employing 512-QAM N-SC-FDE and DD-LMS," *Optics Express*, vol. 22, no. 13, pp. 15328-15334, June 2014.

[30] U. Zolzer, *Digital Audio Signal Processing*. New York: Wiley, 1997.

[31] H. Ochiai and H. Imai, "Performance analysis of deliberately clipped OFDM signals," *IEEE Transactions on Commmunications*, vol. 50, no. 1, pp. 89-101, Jan. 2002.

[32] H. Ochiai and H. Imai, "Performance of the deliberate clipping with adaptive symbol selection for strictly band-limited OFDM systems," *IEEE Journal on Select Areas in Commmunications*, vol. 18, no. 11, pp. 2270-2277, Nov. 2000.

[33] J. Rinne and M. Renfors, "The behavior of orthogonal frequency division multiplexing signals in an amplitude limiting channel," in *Proc. IEEE International Conference on Communications (ICC)*, vol. 1, pp. 381-385, May 1994.

[34] R. Raich, H. Qian and G. T. Zhou, "Optimization of SNDR for amplitude-limited nonlinearities," *IEEE Transactions on Commmunications*, vol. 53, no. 11, pp. 89-101, Nov. 2005.

[35] H. Elgala, R. Mesleh and H. Haas, "Non-linearity effects and predistortion in optical OFDM wireless transmission using LEDs," *International Journal of Ultra Wideband Communications and Systems*, vol. 1, no. 2, pp. 143-150, Nov. 2009.

[36] A. M. Khalid, G. Cossu, R. Corsini, P. Choudhury and E. Ciaramella, "1-Gb/s transmission over a phosphorescent white LED by using rate-adaptive discrete multitone modulation," *IEEE Photonics Journal*, vol. 4, no. 5, pp. 1465-1473, Oct. 2012.

[37] G. Stepniak, J. Siuzdak and P. Zwierko, "Compensation of a VLC phosphorescent white LED nonlinearity by means of Volterra DFE," *IEEE Photonics Technology Letters*, vol. 25, no. 16, pp. 1597-1600, Aug. 2010.

[38] J. Bussgang, "Crosscorrelation functions of amplitude-distorted gaussian signals," *NeuroReport*, vol. 17, no. 2, 1952.

[39] J. G. Smith, "The information capacity of amplitude- and variance-constrained scalar Gaussian channels," *Information and Control*, vol. 18, no. 3, pp. 203-219, Apr. 1971.

[40] T. M. Cover and J. A. Thomas, *Elements of Information Theory*. NY: Wiley, 1991.

[41] I. M. Gelfand and S. V. Fomin, *Calculus of Variations*. Englewood Cliffs, NJ: Prentice-Hall, 1963.

[42] S. Kowlgi, P. Mattheijssen, C. Berland and T. Ridgers, "EVM considerations for convergent multi-standard cellular basestation transmitters," in *Proc. IEEE 22nd International Symposium on Personal, Indoor and Mobile Radio Communications*, pp. 1865-1869, Sept. 2011.

[43] R. J. Baxley, C. Zhao and G. T. Zhou, "Constrained clipping for crest factor reduction in OFDM," *IEEE Transactions on Broadcasting*, vol. 52, no. 4, pp. 570-575, Dec. 2006.

[44] T. Fath and H. Haas, "Performance comparison of MIMO techniques for optical wireless communications in indoor environments," *IEEE Transactions on Communications*, vol. 61, no. 2, pp. 733-742, Feb. 2013.

[45] K. H. Park, Y. C. Ko and M. S. Alouini, "On the power and offset allocation for rate adaptation of spatial multiplexing in optical wireless MIMO channels," *IEEE Transactions on Communications*, vol. 61, no. 4, pp. 1535-1543, April 2013.

[46] P. A. Haigh, Z. Ghassemlooy, I. Papakonstantinou and F. Tedde, "A MIMO-ANN system for increasing data rates in organic visible light communications systems," in *Proc. IEEE International Conference on Communications (ICC)*, pp. 5322-5327, June 2010.

[47] A. Nuwanpriya, S.-W. Ho and C. S. Chen, "Indoor MIMO visible light communications novel angle diversity receivers for mobile users," *IEEE Journal on Select Areas in Commmunications*, vol. 33, no. 9, pp. 1980-1992, Sept. 2015.

[48] K. D. Dambul, D. C. O'Brien and G. Faulkner, "Indoor optical wireless MIMO system with an imaging receiver," *IEEE Photonics Technology Letters*, vol. 23, no. 2, pp. 97-99, Jan. 2011.

[49] L. Zeng, D. C. O'Brien, H. L. Minh, G. E. Faulkner, K. Lee, D. Jung, Y. Oh and E. T. Won, "High data rate multiple input multple output (MIMO) optical wireless communications using white LED lighting," *IEEE Journal on Select Areas in Commmunications*, vol. 27, no. 9, pp. 1654-1662, Dec. 2009.

[50] A. H. Azhar, T.-A. Tran and D. C. O'Brien, "A gigabit/s indoor wireless transmission using MIMO-OFDM visible-light communications," *IEEE Photonics Technology Letters*, vol. 25, no. 2, pp. 171-174, Jan. 2013.

[51] A. Burton, H. L. Minh, Z. Ghassemlooy, E. Bentley and C. Botella, "Experimental demonstration of 50-Mb/s visible light communications using 4×4 MIMO," *IEEE Photonics Technology Letters*, vol. 26, no. 9, pp. 945-948, May 2014.

[52] P. M. Butala, H. Elgala and T. D. C. Little, "SVD-VLC: A novel capacity maximizing VLC MIMO system architecture under illumination constraints," in *Proc. IEEE Globecom Workshop on Optical Wireless Communications (OWC 2013)*, pp. 1087-1092, Dec. 2013.

[53] K. Ying, H. Qian, R. J. Baxley and S. Yao, "Joint optimization of precoder and equalizer in MIMO VLC systems," *IEEE Journal on Select Areas in Commmunications*, vol. 33, no. 9, pp. 1949-1958, Sept. 2015.

[54] K. Ying, Z. Yu, R. J. Baxley, H. Qian, G. K. Chang and G. T. Zhou, "Nonlinear distortion mitigation in visible light communicaitons," *IEEE Wireless Communications*, vol. 22, no. 2, pp. 36-45, Apr. 2015.

[55] I. Stefan, H. Elgala, R. Mesleh, D. O Brien and H. Haas, "Optical wireless OFDM system on FPGA: study of LED nonlinearity effects," in *Proc. IEEE Vehicular Technology Conference (VTC)*, pp. 1-5, May 2011.

[56] Z. Yu, K. Ying, R. J. Baxley and G. T. Zhou, "PAPR reduction for bit-loaded OFDM in visible light communications," in *Proc. IEEE Wireless Communications and Networking Conference (WCNC)*, pp. 346 - 351, Mar. 2015.

[57] CVX Research, Inc., "CVX: Matlab software for disciplined convex programming, version 2.0 (beta)," June 2013.

[58] K. Ying, Z. Yu, R. J. Baxley and G. T. Zhou, "Optimization of signal-to-noise-plus-distortion ratio for dynamic-range-limited nonlinearities," *Digital Signal Processing*, vol. 36, pp. 104-114, Jan. 2015.

[59] R. Mesleh, R. Mehmood, H. Elgala and H. Haas, "Indoor MIMO optical wireless communication using spatial modulation," in *Proc. IEEE International Conference on Communications (ICC)*, pp. 1-5, May 2010.

[60] F. R. Gfeller and U. H. Bapst, "Wireless in-house data communication via diffuse infrared radiation," *Proc. IEEE*, vol. 67, pp. 1474-1486, Nov. 1979.

[61] J. Zhang, J. Yu, N. Chi and H.-C Chien, "Time-domain digital pre-equalization for band-limited signals based on receiver-side adaptive equalizers," *Optics Express*, vol. 22, no. 17, pp. 20515-20529, Aug. 2014.

[62] Z. Dong, X. Li, J. Yu, Z. Cao and N, Chi, "8×9.95-Gb/s Ultra-Dense WDM-PON on a 12.5-GHz Grid With Digital Pre-Equalization," *IEEE Photonics Technology Letters*, vol. 25, no. 2, pp. 194-197, Jan. 2013.

VITA

Kai YING was born in Yueyang, Hunan, China. He received the B.S. degree with honor from the Department of Electronic Engineering, Shanghai Jiao Tong University, Shanghai, China in 2010. He received the M.E. degree with honor from the Department of Electronic Engineering, Shanghai Jiao Tong University and the M.S. degree from the school of Electrical and Computer Engineering, Georgia Institute of Technology in 2013. Currently, he is pursuing his Ph.D. degree in Georgia Institute of Technology, Atlanta, GA. His research interests include statistical signal processing and visible light communication.